minerals

MDPI

Article

Comparative Analysis of CO_2 Sequestration Potential in Shale Reservoirs: Insights from the Longmaxi and Qiongzhusi Formations

Bo Li [1,*], Bingsong Yu [1,*], Paul W. J. Glover [2], Piroska Lorinczi [2], Kejian Wu [3], Ciprian-Teodor Panaitescu [3], Wei Wei [4], Jingwei Cui [5] and Miao Shi [6]

[1] School of Earth Sciences and Resources, China University of Geosciences, Beijing 100083, China
[2] School of Earth and Environment, University of Leeds, Leeds LS2 9JT, UK; p.w.j.glover@leeds.ac.uk (P.W.J.G.); p.lorinczi@leeds.ac.uk (P.L.)
[3] School of Engineering, University of Aberdeen, Aberdeen AB24 3FX, UK; kejian.wu@abdn.ac.uk (K.W.); c.panaitescu.21@abdn.ac.uk (C.-T.P.)
[4] School of Geophysics and Geomatics, China University of Geosciences, Wuhan 430074, China; weiwei@cug.edu.cn
[5] PetroChina Research Institute of Petroleum Exploration & Development, Beijing 100083, China; cuijingwei@petrochina.com.cn
[6] School of Gemology and Material Technology, Hebei GEO University, Shijiazhuang 050031, China; miaoer727@126.com
* Correspondence: limibo@foxmail.com (B.L.); yubs@cugb.edu.cn (B.Y.); Tel.: +86-13121984164 (B.L.)

Abstract

Shale reservoirs offer significant potential for CO_2 geological sequestration due to their extensive nanopore networks and heterogeneous pore systems. This study comparatively assessed the CO_2 storage potential of the Lower Silurian Longmaxi and Lower Cambrian Qiongzhusi shales through an integrated approach involving organic geochemical analysis, mineralogical characterization through X-ray diffraction (XRD), mercury intrusion capillary pressure (MICP), low-pressure nitrogen and carbon dioxide physisorption, field-emission scanning electron microscopy (FE-SEM), stochastic 3D microstructure reconstruction, multifractal analysis, and three-dimensional succolarity computation. The results demonstrate that mineral assemblages and diagenetic history govern pore preservation: Longmaxi shales, with moderate maturity and shallower burial, retain abundant organic-hosted mesopores, whereas overmature and deeply buried Qiongzhusi shales are strongly compacted and mineralized, reducing pore availability. Multifractal spectra and 3D reconstructions reveal that Longmaxi develops broader singularity spectra and higher succolarity values, reflecting more isotropic meso-/macropore connectivity at the SEM scale, while Qiongzhusi exhibits narrower spectra and lower succolarity, indicating micropore-dominated and anisotropic networks. Longmaxi has nanometer-scale throats ($D_{50} \approx$ 10–25 nm) with high CO_2 breakthrough pressures ($P_{10} \approx 0.57$ MPa) and ultra-low RGPZ permeability (mean $\approx 1.5 \times 10^{-2}$ nD); Qiongzhusi has micrometer-scale throats ($D_{50} \approx$ 1–3 μm), very low breakthrough pressures ($P_{10} \approx 0.018$ MPa), and much higher permeability (mean $\approx 4.63 \times 10^{3}$ nD). Storage partitioning further differs: Longmaxi's median total capacity is ≈15.6 kg m^{-3} with adsorption ≈ 93%, whereas Qiongzhusi's median is ≈12.8 kg m^{-3} with adsorption ≈ 70%. We infer Longmaxi favors secure adsorption-dominated retention but suffers from injectivity limits; Qiongzhusi favors injectivity but requires reliable seals.

Keywords: CO_2 sequestration; shale reservoirs; diagenetic minerals; pore characteristic and modeling; multifractal analysis; fractal dimension; lacunarity; 3D succolarity

Academic Editors: Fei Wang and Rafael Santos

Received: 1 August 2025
Revised: 11 September 2025
Accepted: 12 September 2025
Published: 19 September 2025

Citation: Li, B.; Yu, B.; Glover, P.W.J.; Lorinczi, P.; Wu, K.; Panaitescu, C.-T.; Wei, W.; Cui, J.; Shi, M. Comparative Analysis of CO_2 Sequestration Potential in Shale Reservoirs: Insights from the Longmaxi and Qiongzhusi Formations. *Minerals* **2025**, *15*, 997. https://doi.org10.3390/min15090997

1. Introduction

Modern economic advancement has historically relied on the intensive use of fossil fuels, such as coal, oil, and natural gas, to meet increasing demands for energy, transportation, and manufacturing [1,2]. Driven by record-high fossil fuel consumption, the continuous increase in anthropogenic carbon dioxide (CO_2) emissions has triggered a series of severe global environmental issues in the past decades, including climate change, rising sea levels, and ecosystem imbalances [3–5]. Many countries now aim to reach carbon neutrality by the middle of this century [6,7].

To mitigate the escalating atmospheric CO_2 levels, carbon capture, utilization, and storage (CCUS) technologies have emerged as critical strategies [4,8]. The process includes separating carbon dioxide (CO_2) from industrial sources, transporting the captured CO_2 to specific locations, and either recycling or storing the transported CO_2 in geological formations [9,10].

Geological sequestration, characterized by its large-scale capacity and long-term stability, represents a particularly promising approach for significant CO_2 emission reductions. Traditional storage options include depleted conventional reservoirs and deep saline aquifers, relying on unique geological trapping structures [11,12]. Other types of subsurface systems will be briefly discussed in the following paragraph.

Sandstone aquifers are relatively abundant and offer high storage potential as well as good injectivity, but their performance depends strongly on caprock integrity [13]. Depleted sandstone reservoirs offer significant advantages due to complete characterization, increased confidence in caprock integrity, in the case of gas reservoirs, and existing infrastructure; however, previous ageing infrastructure can also prove challenging for repurposing [14]. Carbonate reservoirs, particularly depleted oil and gas fields, provide secure storage with an increased importance of the fluid–rock geochemical reaction, though this can also potentially impede injection efficiency [15]. More recently, mixed siliciclastic–carbonate successions have been proven to enhance trapping and chemical reaction due to diagenetic heterogeneity [16]. Other options include coal seams where CO_2 can be efficiently adsorbed and also provide potential for enhanced coalbed methane recovery, though the risk of impaired injectivity due to coal swelling is significant [17,18]. Salt caverns offer exceptional seal integrity compared to other sedimentary systems [19] but relatively limited storage capacity. Non-sedimentary sequestration has recently gained interest, with basalts showing rapid mineralization into stable carbonates [20] and ultramafic formations also showing high reactivity [21].

However, recent research has increasingly focused on shale reservoirs due to their extensive nanoscale pore networks, substantial heterogeneity, and widespread geological distribution [22–24]. Shale formations exhibit better adsorption capacities compared to conventional reservoirs, and their unique pore structures and mineralogical compositions are expected to facilitate effective and long-term CO_2 sequestration [25–27]. Compared with methane, CO_2 demonstrates a substantially higher adsorption affinity in shale [28]. Thus, injecting CO_2 into shale formations can improve oil and gas recovery while also reducing water consumption and sequestering CO_2 [29,30].

As noted, shales can provide excellent sites for CO_2 sequestration, showcasing significant advantages. However, shale carbon capture and storage also provide unique challenges. The primary issue is the low injectivity compared to other reservoir rock types such as sandstones and carbonates, which is a result of the characteristic small pore size [31]. Fracturing can be a solution, improving injectivity [31]; however, injected CO_2 initially occupies the fractures and larger pores, with the fine pore network remaining less accessible and requiring significant capillary pressure to penetrate. Moreover, CO_2–rock interactions may also alter the mechanical properties of the shales over time, resulting in less brittle,

more ductile rocks with higher toughness [32], which has significant implications in any hydraulic fracturing design. Reservoir heterogeneity and permeability control the CO_2 flow, with permeability evolution due to clay swelling being an additional critical factor [33].

The potential for achieving these goals largely depends on the knowledge of the mechanisms governing CO_2 adsorption and their interplay with pore structure in shale. Several key factors influence CO_2 sequestration capacity in shale reservoirs, notably temperature, pressure, total organic carbon (TOC) content, thermal maturity (Ro), moisture, mineralogical composition, and multiscale pore structures.

Generally, the gas adsorption increases with pressure and decreases with temperature [3,9]. Numerous studies indicate that total organic carbon content (TOC) is the primary factor facilitating the sorption capacity of shales [34,35]. Many researchers found that the thermal maturation of the OM releases acid fluids and hydrocarbons, creating pores and micro-cracks for potential gas storage sites in minerals and OM [36–38]. However, the presence of pore water may compete with gas for adsorption sites, and if it is alkaline, it would inhibit mineral dissolution and decrease the pore generation [37].

Clay minerals, a primary component of shale, play a crucial role in various aspects [39]. It is found that clays like smectite possess a significant reactive surface that can sorb substantial dissolved OM, and they also function as a preservative during burial [40,41]. In particular, clay floccules can encapsulate organic matter, enhancing its preservation during and after deposition, a process further amplified by rapid burial promoted through mud-induced turbulence dampening [42].

Moreover, clay minerals such as illite and mixed-layer illite–smectite (I-S) with abundant nanopores exhibit a stronger CO_2 adsorption affinity than quartz [43]. More importantly, the porous clay–OM matrix can cause major geochemical and geomechanical changes in subsurface conditions [44,45].

The pore system of shale with abundant nanopores (<100 nm) has complex sedimentary and diagenetic backgrounds [46,47]. Based on the classification of the International Union of Pure and Applied Chemistry (IUPAC), pores are categorized as micropores (<2 nm), mesopores (2–50 nm), and macropores (>50 nm) [48]. Understanding pore characteristics, such as porosity, pore size distribution (PSD), heterogeneity, and connectivity, is of great importance for improving gas recovery and storage. Normally, pores characterized by a large surface area and volume, along with effective connectivity, offer significant adsorption sites and flow channels for CO_2, thereby enhancing the efficiency of CO_2 injection and storage.

Numerous investigations have been conducted to characterize shale pores through various methods, which can be divided into two groups: fluid-based probing techniques and radiation-based imaging and scattering methods. The first suite of methods uses the interaction between fluids and pore surfaces to detect the porosity, pore size distribution, and surface area. Some common methods in this group are low-pressure gas adsorption (for example, N_2 and CO_2) for characterizing micro- and mesopores [49,50], mercury intrusion porosimetry for larger pore throats [51], and nuclear magnetic resonance (NMR) techniques [52], such as NMR cryoporometry, which give information about pore size distribution and fluid mobility without using specific pore geometry models [53].

Radiation-based methods, on the other hand, either directly visualize pore structures or derive statistical parameters based on their interactions with radiation or particle beams. X-ray computed micro- and nano-tomography (μCT, nano-CT) and other methods can make 3D images of connected pore systems at the micron to sub-micron scale [54]. However, their spatial resolutions are not sufficient for imaging pores on nanoscale. Thus, people often use field emission scanning electron microscopy (FE-SEM) to look at the shape of nano-sized pores and how minerals are linked together [55]. Helium ion microscopy (HIM) also gives

very high-resolution images of surfaces [56,57]. However, it lacks 3D imaging capability. Focused ion beam-SEM (FIB-SEM) can help to reconstruct the high-resolution 2D SEM images into a 3D stack [58,59]. Small-angle and ultra-small-angle neutron scattering (SANS and USANS) are very useful for statistically studying pore structures that are between nanometers and micrometers, especially in organic-rich matrices [60,61].

Although direct imaging techniques and tests are widely adopted, they often remain limited by cost, resolution, and sample size constraints. As an alternative, the stochastic approaches have been proposed to generate 3D pore space models using spatial and petrographical information from 2D thin sections or rock formation process. Wu et al. [62] developed a stochastic reconstruction approach that generates 3D pore architecture models (PAMs) from 2D thin section images. More recently, Luo et al. [63] constructed digital rock models with a process-driven modeling approach using monodisperse and polydisperse spherical grains. These advances demonstrate that statistically reconstructed models can provide reliable 3D representations of pore systems, offering a powerful, non-destructive way for reservoir characterization.

While conventional techniques provide valuable insights into pore structures, they often fall short in capturing the complexity, anisotropy and heterogeneity of pore structures across scales. In this case, fractal theory provides us with a set of tools for quantitatively describing the multiscale structural properties of pore networks in shale.

Previous studies have widely applied monofractal theory to characterize pore structure complexity in shale, primarily through the estimation of a single fractal dimension [64,65]. Common approaches include calculating the box-counting fractal dimension from 2D SEM or thin section images, extracting 3D fractal dimensions from CT-derived pore volumes, and determining surface fractal dimensions based on nitrogen adsorption data using the Frenkel–Halsey–Hill (FHH) model or Neimark's thermodynamic approaches [66,67]. Additionally, fractal dimensions have been inferred from mercury intrusion capillary pressure (MICP) curves and small-angle neutron scattering (SANS) measurements, offering a global descriptor of roughness or spatial heterogeneity [68,69]. While these monofractal methods provide valuable insights, they are fundamentally limited in capturing the scale-dependent heterogeneity and spatial intermittency inherent in shale pore systems. In contrast, multifractal theory extends the capability of fractal analysis by introducing a spectrum of scaling exponents rather than relying on a single fractal dimension [70,71]. This approach allows for a more comprehensive characterization of the irregular and hierarchical nature of pore systems, especially in organic-rich shales where pore attributes—such as size, density, and connectivity—vary across spatial and measurement scales.

Despite the established applications of monofractal and multifractal approaches in characterizing pore structure complexity and heterogeneity, these methods typically do not explicitly account for percolation properties. A lesser-known fractal parameter termed succolarity quantifies connectivity and percolation capacity in porous media [72,73]. We developed a 3D succolarity computation scheme in previous work [74]. When applied to CT images or reconstructed models of rocks, succolarity captures directional connectivity, percolation properties, and the anisotropy of accessible pore clusters. Thereby, it provides an additional dimension to the analysis of nanoporous networks relevant for CO_2 transport and storage.

The Lower Silurian Longmaxi Formation and the Lower Cambrian Qiongzhusi (Qiongzhusi) Formation represent two significant marine shale sequences in South China, exhibiting distinct geological and geochemical characteristics [75,76]. According to previous comparative studies, the Longmaxi shale generally possesses high total organic carbon (TOC), moderately high thermal maturity (Ro typically between 2.0%–3.0%), well-developed organic-matter pores, and favorable reservoir pressures, contributing to its

greater shale gas production potential [77–79]. In contrast, the Qiongzhusi shale typically shows over-mature states (Ro commonly exceeding 3.0%, often reaching up to 4.5%), limited organic-matter porosity, and lower gas contents [80–82].

Many studies have focused on the pore structure, gas generation potential, adsorption capacity, and their geological controls in the Longmaxi and Qiongzhusi shales [22,83–85], using a combination of laboratory techniques, such as HP-MIP, gas adsorption, electron microscopy (FE-SEM and FIB-SEM), and NMR. Furthermore, some comparative investigations involving both shales and other gas-bearing formations have linked fractal and multifractal analyses with experimental methods to explore the multiscale properties of the pore network [8,83,86,87].

However, to our best knowledge, the stochastic 3D reconstruction of the shale pore structure and the 3D succolarity have not previously been applied to compare the two formations on their CO_2 sequestration potential. We combine mineralogical analyses, experimental techniques, 3D modeling, and fractal/multifractal computation for the two shales to (i) quantify and compare the multiscale pore properties, (ii) link shales' mineralogy and nanostructure to assess their CO_2 storage potential, (iii) evaluate the applicability of the newly developed 3D succolarity and the PAMs on shales, and (iv) compare the CO_2 storage and injectivity of the Longmaxi–TY1 and Qiongzhusi–N206 shales.

2. Materials and Methods

The Upper Yangtze Platform in southern China extends across Henan, most of Guizhou, eastern Sichuan, Chongqing, western Hubei and Hunan, and northern Yunnan [88,89]. This region underwent multiple phases of tectonic activity, which generated a complex system of faults and folds [89]. Sedimentary successions show that black shale facies gradually thickened from the northwest toward the southeast, reflecting a depositional transition from a shallow marine platform into a more open shelf environment [90]. During the early Cambrian, a global eustatic sea-level rise triggered a widespread marine transgression, creating conditions favorable for the accumulation of carbonaceous and calcareous shales, together with carbonates and siltstones [91]. As a result, organic-rich black shales became widely developed across the Upper Yangtze Platform, including the Lower Cambrian Qiongzhusi Formation and the Lower Silurian Longmaxi Formation.

The Lower Silurian Longmaxi Formation represents one of the most significant shale gas reservoirs in China [92]. It exhibits high thermal maturity and elevated organic matter content, together with favorable porosity and natural fracturing capacity [93]. Reported total organic carbon (TOC) values vary widely, from about 0.5% to over 25% [94]. Proven reserves of the formation reach approximately 3200×10^8 cubic feet of gas, with burial depths typically between 1500 and 4500 m [95]. Hydrocarbon generation within the Longmaxi shale is attributed to deposition under tectonically stable, organic-rich, low-energy, and oxygen-deficient deep-shelf environments [95]. The Lower Cambrian Qiongzhusi Formation comprises of black shales deposited within a deep-water continental shelf environment [96]. In the Changning area of southern Sichuan, designated as a key national demonstration zone for shale gas exploration and development, substantial progress has been achieved in both exploration and large-scale production [96]. To date, several hundred wells have been drilled in the region, with an average daily output exceeding 7×10^6 m^3 [97]. The total annual shale gas production of the area is projected to approach 100×10^{12} m^3 [97,98].

A total of 20 marine shale core samples were selected from two wells (TY1 and N206) that were drilled through Longmaxi and Qiongzhusi formations in the northern Guizhou (Tongzi area) and southern Sichuan (Changning area) on the Upper Yangtze Platform (Appendix B). They cover high-maturity to over-maturity stages (Ro 1.83%–4.58%)

and various TOC from 0.45% to 7.58%. The well locations are marked in Figure 1 with stratigraphic information in Tables A1 and A2, core descriptions listed in Tables A3 and A4, Appendix A.

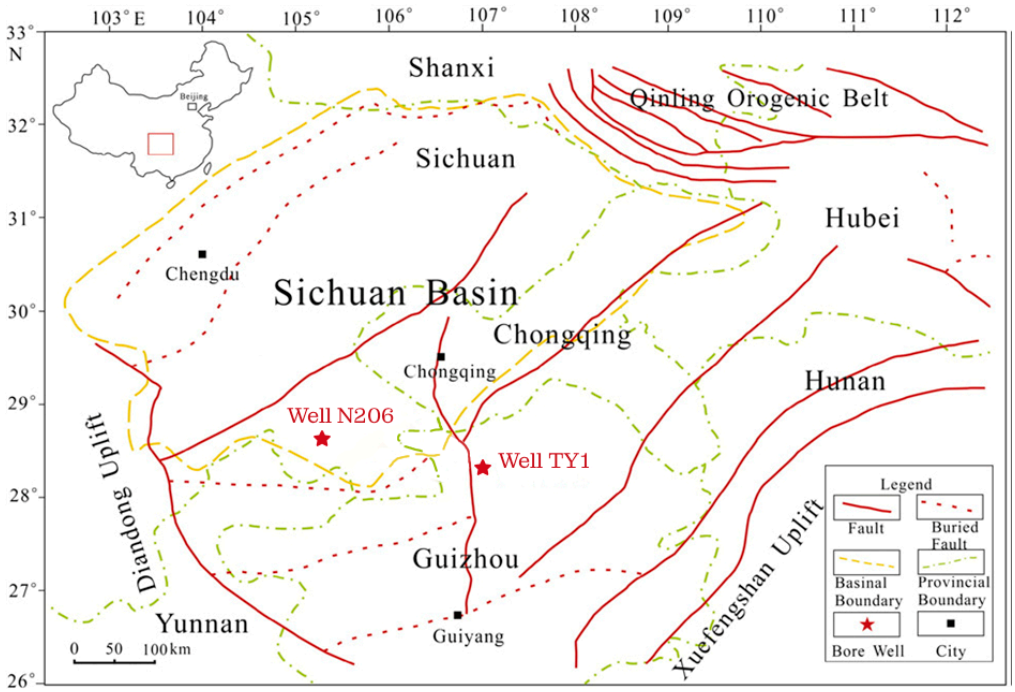

Figure 1. Sichuan basin geologic map showing well locations (modified from Sun et al. [99]).

2.1. TOC, Ro and Mineralogy

2.1.1. Total Organic Carbon (TOC) Analysis

Total organic carbon content was determined to quantify OM abundance in shale samples. Approximately 2–3 g of bulk shale samples was mechanically pulverized to <150 μm (100 mesh) to ensure homogeneity. To eliminate inorganic carbon derived from carbonate minerals, powdered samples were treated with dilute hydrochloric acid (10%–15% HCl) at room temperature until gas evolution ceased. The residues were then repeatedly rinsed with deionized water until neutral pH was achieved, followed by drying at 60 °C under vacuum until constant weight was attained. Approximately 110 mg of pre-treated samples was analyzed using a Leco CS-844 carbon/sulfur analyzer (LECO Corporation, located in St. Joseph, MI, USA). TOC content was calculated based on CO_2 emissions measured during high-temperature combustion (540 °C) under an oxygen-enriched atmosphere. The experiments were performed at the China University of Geosciences (Beijing).

2.1.2. Thermal Maturity Assessment

Vitrinite reflectance (VRr), a globally accepted thermal maturity indicator, was employed to evaluate the thermal maturity of OM. Due to the absence of terrestrial vitrinite in marine shales of the Lower Cambrian and Lower Silurian sequences in South China, equivalent *VRr* values were derived from bitumen reflectance (*BRr*) measurements using an empirically validated conversion model [100,101]:

$$VRr = BRr + 0.2443/1.0495 \quad (1)$$

Polished shale blocks were prepared to optical-grade surfaces to minimize light scattering during reflectance measurements. A Leitz MVP-3 photomultiplier system coupled with a Leitz Laborlux 12Pol optical microscope (Leica Microsystems, Wetzlar and

Mannheim, Germany) was operated under standardized conditions (23 ± 3 °C, 30%–32% relative humidity) for BRr determination. A minimum of 50 valid measurements per sample ensured statistical reliability. The samples were tested at the China University of Petroleum (Beijing).

2.1.3. Mineralogical Characterization

Quantitative X-ray diffraction (XRD) analysis was systematically performed to determine bulk and clay mineral compositions. Core-derived shale samples were pulverized to <50 μm (~300 mesh) and divided into two subsamples: (1) whole-rock powders and (2) clay mineral concentrates isolated via gravity settling. XRD patterns were acquired using a Bruker D8 DISCOVER (Bruker AXS GmbH, Karlsruhe, Germany) diffractometer equipped with a Cu-Kα radiation source (40 kV, 30 mA). Scans covered a 2θ range of 2–70° with a step size of 0.02° and a counting time of 0.5 s/step. Mineral phase identification and quantification were conducted using Jade® 6.0 software, incorporating Rietveld refinement and reference intensity ratio (RIR) corrections to account for crystalline and amorphous components. The analysis was conducted at the China University of Geosciences (Beijing).

2.2. Mercury Intrusion Capillary Pressure (MICP)

Mercury intrusion porosimetry was performed to obtain mercury intrusion capillary pressure (MICP) data using a PorMaster GT 60 analyzer (Quantachrome Instruments, Boynton Beach, FL, USA) at the Beijing Center for Physical and Chemical Analysis. Cubic specimens (~1 cm^3) were polished on all six faces to eliminate cutting artifacts, then oven-dried at 105 °C for 48 h to remove moisture and volatiles before cooling to ambient temperature (25 °C). Measurements employed high-purity mercury with a surface tension of 485 mN/m and a contact angle of 140°. Pressure was incrementally increased from 0.5 to 60,000 psia (3.4 kPa to 413 MPa), corresponding to a theoretical pore–throat diameter range of 3.6 nm to 1000 μm, with a 10–60 s equilibration time per pressure step to ensure complete intrusion. Pore size distribution was derived from intrusion volumes using the Washburn equation [102]:

$$r = \frac{-2\gamma cos\theta}{P} \quad (2)$$

where r = pore–throat radius (nm), γ = mercury surface tension (mN/m), θ = contact angle (°), and P = applied pressure (MPa). Calibration was verified using certified alumina reference materials (Boynton Beach, FL, USA), and reported parameters include median pore diameter (D50), cumulative pore volume, and pore-size distribution density curves.

2.3. N_2 and CO_2 Physisorption Experiments

Low-pressure N_2 and CO_2 physisorption experiments were conducted to characterize the pore structure of shale samples. Prior to analysis, the shale was pulverized to 40–80 mesh (0.18–0.42 mm) and dehydrated at 110 °C (383.15 K) under vacuum for 5 h to remove residual moisture and gases.

N_2 adsorption–desorption isotherms were measured at 77.3 K (−195.8 °C) using a Quantachrome Autosorb-iQ instrument (Anton Paar, Boynton Beach, FL, USA) at the Beijing Physical and Chemical Testing Center. The relative pressure (P/P_0) range was set from 0.0009 to 0.995, with adsorption data collected during pressurization to saturation vapor pressure and desorption data recorded during depressurization. Specific surface area (SSA) was calculated using the Brunauer–Emmett–Teller (BET) method [103]. Pore volume and size distribution were determined via density functional theory (DFT) and Barrett–Joyner–Halenda (BJH) models [104,105].

CO_2 adsorption isotherms were obtained at 273.1 K (0 °C) on a Quantachrome Nova Station A instrument (Anton Paar, Boynton Beach, FL, USA), with pressure incrementally

raised to 104.5 kPa (784 mmHg). Micropore properties (pore size, SSA, pore volume) were analyzed using DFT theory [106,107].

2.4. FE-SEM Investigation and 3D Pore Network Reconstruction

A total of 10 shale samples—five from the Longmaxi Formation and five from the Qiongzhusi Formation—were selected for pore structure and mineralogical characterization. All samples were precision-sectioned into 1 cm × 1 cm × 0.1 cm blocks. To achieve optimal imaging surfaces, the sample faces were polished using an Ar-ion milling system (Gatan Ilion+ II, Model 697, Gatan, Inc., Pleasanton, CA, USA) at 6 kV for 6–8 h. FE-SEM observations were conducted using a ZEISS GEMINI 2 field-emission scanning electron microscope (Carl Zeiss AG, Oberkochen, Germany) (resolution: 0.8 nm) equipped with a Bruker Quantax X-act EDS system at the Institute of Geology and Geophysics, Chinese Academy of Sciences. High-resolution imaging enabled differentiation of mineral phases, OM, and pore systems through grayscale contrast, permitting quantitative assessment of pore size distribution, pore typology (interparticle, intraparticle, and organic-matter-hosted pores), pore connectivity, and mineral morphology across both formations. Complementary EDS elemental mapping provided spatial correlations between pore networks and mineral compositions.

In this study, we adopted a stochastic 3D pore structure reconstruction approach based on the Markov mesh random field (MMRF) framework [108–110], following the methodology developed by Wu et al. [62]. The technique uses binary thin-section images to derive local transition probabilities, which are then applied in a single-pass MCMC scanning algorithm to generate 3D pore architecture models (PAMs). The model builds the structure voxel-by-voxel using a 15-neighborhood system that captures third-order spatial dependencies, enabling rapid and realistic reconstruction of heterogeneous pore networks. For a more detailed procedure, please refer to Wu et al. [62].

2.5. Fractal and Multifractal Analysis

In fractal geometry, fractal dimension measures complexity relating to crucial aspects of patterns: self-similarity and irregularity. Lacunarity, as a measure of spatial distribution, helps to further characterize the heterogeneity of structures, especially when their fractal dimensions are similar. We used the box-counting method incorporated in ComsystanJ (Complex Systems Analysis for ImageJ) to calculate the fractal dimension and lacunarity of the 3D pore network reconstructed from the 2D SEM images [111]. ComsystanJ-1.2.0 is a collection of Fiji/ImageJ2 plugins to compute fractal parameters, entropy, and other nonlinear measures of 2D/3D images and signals.

Three-dimensional succolarity quantifies the connectedness and percolation potential of the nanopore network. We employed the computation scheme from our latest work [74]. The method assumes that a virtual fluid floods through the 3D binary images from six different directions (left to right, right to left, top to bottom, bottom to top, front to back, and back to front). The images are then analyzed by the box-counting method. Boxes with equal size $BS(k)$ (k is the number of possible divisions) are placed on the images, and the porosity of permeable area $\phi(BS(k))$ is measured in each box. Then, 3D succolarity for each direction can be calculated using the following equation:

$$\mathrm{Su}(\sigma)(BS(k), dir) = \frac{\sum_{k=1}^{n} \phi(BS(k)) \times D(BS(k), pc)}{\sum_{k=1}^{n} D(BS(k), pc)} \quad (3)$$

where k denotes box sizes, "*dir*" signifies the flooding direction, D represents the fluid flooding distance from the inlets, and pc is the box centroid position. For detailed information on succolarity calculation, please refer to previous studies [72,74].

We performed multifractal analysis on the gas adsorption isotherms (N_2 and CO_2) to quantitatively characterize the heterogeneity of pore structures across multiple scales [112]. Adsorption data were initially obtained as specific volumes adsorbed (cm^3/g) at standard temperature and pressure conditions over a wide range of relative pressures (P/P_0). To carry out the multifractal analysis, the adsorption isotherm data were divided into equal parts or boxes of length ε using a method called dyadic scaling, where $\varepsilon = 2^{-k}L$ (k = 0, 1, 2, . . ., and L is the total length, which is the difference between the highest and lowest relative pressures) [113]. For each scale ε, the total gas volume adsorbed within each interval (box) was summed and normalized by the total adsorbed volume (N_t) to compute the probability mass function $p_i(\epsilon)$, expressed as

$$p_i(\epsilon) = \frac{N_i(\epsilon)}{N_t} \tag{4}$$

where $N_i(\epsilon)$ represents the gas volume adsorbed in the ith interval.

Subsequently, the partition function, $X(q, \epsilon)$, was calculated for a series of statistical moments q, ranging typically from −10 to +10 in increments of 0.5, according to the following equation:

$$X(q, \epsilon) = \sum_{i=1}^{N(\epsilon)} p_i(\epsilon)^q \tag{5}$$

Using the partition function, we determined the mass exponent function $\tau(q)$, which describes the scaling relationship between probability distributions and box sizes (ε), using linear regression to approximate the limit as ε approaches zero:

$$\tau(q) = \lim_{\varepsilon \to 0} \left[ln \sum_i \frac{P_i(\varepsilon)^q}{ln\left(\frac{1}{\varepsilon}\right)} \right] \tag{6}$$

The generalized dimension D_q, or Rényi dimension [114,115], was derived from $\tau(q)$ as

$$D_q = \frac{\tau(q)}{q-1}, \quad q \neq 1 \tag{7}$$

For q = 1, the information dimension D_1 was obtained by applying L'Hôpital's rule:

$$D_1 = \lim_{\varepsilon \to 0} \frac{\sum_{i=1}^{N(\varepsilon)} P_i(\varepsilon) ln P_i(\varepsilon)}{ln(\varepsilon)} \tag{8}$$

Additionally, the multifractal singularity spectrum was calculated using the Chhabra–Jensen method to characterize singularities and their distribution within the adsorption data. The singularity strength $\alpha(q)$ and the multifractal spectrum $f(\alpha)$ were obtained as follows:

$$\alpha(q) \propto \frac{\sum_{i=1}^{N(\varepsilon)} \mu_i(q, \varepsilon) log[p_i(\varepsilon)]}{log(\varepsilon)} \tag{9}$$

$$f(\alpha) \propto \frac{\sum_{i=1}^{N(\varepsilon)} \mu_i(q, \varepsilon) log[\mu_i(q, \varepsilon)]}{log(\varepsilon)} \tag{10}$$

Here, the weighting factor $\mu_i(q, \epsilon)$ is defined as

$$\mu_i(q, \epsilon) = \frac{p_i(\epsilon)^q}{\sum_{i=1}^{N(\epsilon)} p_i(\epsilon)^q} \tag{11}$$

All calculations were implemented using custom-developed Python (Version: 3.13.7) scripts specifically designed for multifractal analysis, ensuring reproducibility, accuracy, and consistency across the different adsorption datasets.

3. Results

3.1. Organic Geochemistry and Mineralogy

Table 1 summarizes the organic geochemical characteristics and lithofacies types of the Longmaxi (TY1) and Qiongzhusi (N206) shale samples. Total organic carbon (TOC) contents in the Longmaxi Formation range from 0.45 wt% to 7.58 wt%, with an average of 4.40 wt%. In contrast, the Qiongzhusi Formation displays lower TOC, ranging from 1.02 wt% to 4.39 wt%, with an average of 2.37 wt%. Despite these variations, both formations are classified as organic-rich, with TOC contents exceeding the conventional hydrocarbon generation threshold (>2 wt%) [116]. Equivalent vitrinite reflectance (Ro) values, derived from bitumen reflectance, indicate advanced thermal maturity in both formations. Longmaxi shales yield Ro values between 1.83% and 2.61% (average 2.16%), while Qiongzhusi shales exhibit significantly higher Ro values, ranging from 3.62% to 4.58% (average 4.07%), confirming that both units are within the overmature gas window.

Table 1. Lithofacies types, and organic geochemical results of shale samples from TY1 and N206.

Formation	Sample ID	Depth (m)	Shale Lithofacies Types	R_o (%)	TOC (%)
Longmaxi	TY1-1	622.6	Clay-siliciclastic shale	1.95	4.39
	TY1-2	647.3	Clay-siliciclastic shale	2.38	7.2
	TY1-3	654.9	Siliciclastic-rich shale	2.06	0.54
	TY1-4	659.8	Clay-siliciclastic shale	1.94	4.15
	TY1-5	663.2	Calcareous shale	1.83	6.25
	TY1-9	665.0	Calcareous shale	2.18	0.45
	TY1-12	667.3	Calcareous shale	2.53	5.25
	TY1-14	670.0	Mixed shale	2.12	7.58
	TY1-15	670.7	Siliciclastic-rich shale	1.95	5.30
	TY1-20	677.5	Clay-siliciclastic shale	2.61	2.93
Average	/	/	/	2.16	4.40
Qiongzhusi	N206-1	1846.53	Clay-siliciclastic shale	3.62	1.04
	N206-2	1851.35	Siliciclastic-rich shale	3.79	2.19
	N206-3	1859.64	Siliciclastic-rich shale	3.88	3.11
	N206-4	1861.42	Siliciclastic-rich shale	3.95	2.68
	N206-5	1862.08	Siliciclastic-rich shale	3.97	2.27
	N206-6	1863.32	Siliciclastic-rich shale	3.83	2.15
	N206-8	1868.59	Siliciclastic-rich shale	4.39	2.07
	N206-9	1885.46	Siliciclastic-rich shale	4.58	2.63
	N206-10	1886.53	Clay-siliciclastic shale	4.39	3.04
	N206-11	1888.26	Siliciclastic-rich shale	4.25	2.49
Average	/	/	/	4.07	2.37

In terms of mineralogy, bulk rock compositions (Figure 2a,c) reveal clear differences between the two formations. Longmaxi shales have lower average quartz contents (33.75 wt%) compared to Qiongzhusi shales (46.21 wt%) and show significantly higher carbonate abundances, including calcite and dolomite (average 24.29 wt% vs. 7.67 wt%). This implies that the Longmaxi Formation includes more calcareous and mixed lithofacies, while the Qiongzhusi samples are predominantly siliciclastic-rich. K-feldspar is almost absent in Qiongzhusi shales, whereas Longmaxi samples contain measurable amounts (average 2.47 wt%). Pyrite is generally more abundant in Qiongzhusi samples (average 5.38 wt%) than in Longmaxi samples (1.62 wt%), reflecting differences in redox conditions and diagenetic pathways. Additionally, the numerical data summarizing the mineralogy, lithofacies, organic geochemistry, and clay mineral composition for samples TY1 and N206 (represen-

tative for Longmaxi and Qiongzhusi formations, respectively) are tabulated and presented in Tables A3 and A4, Appendix A.

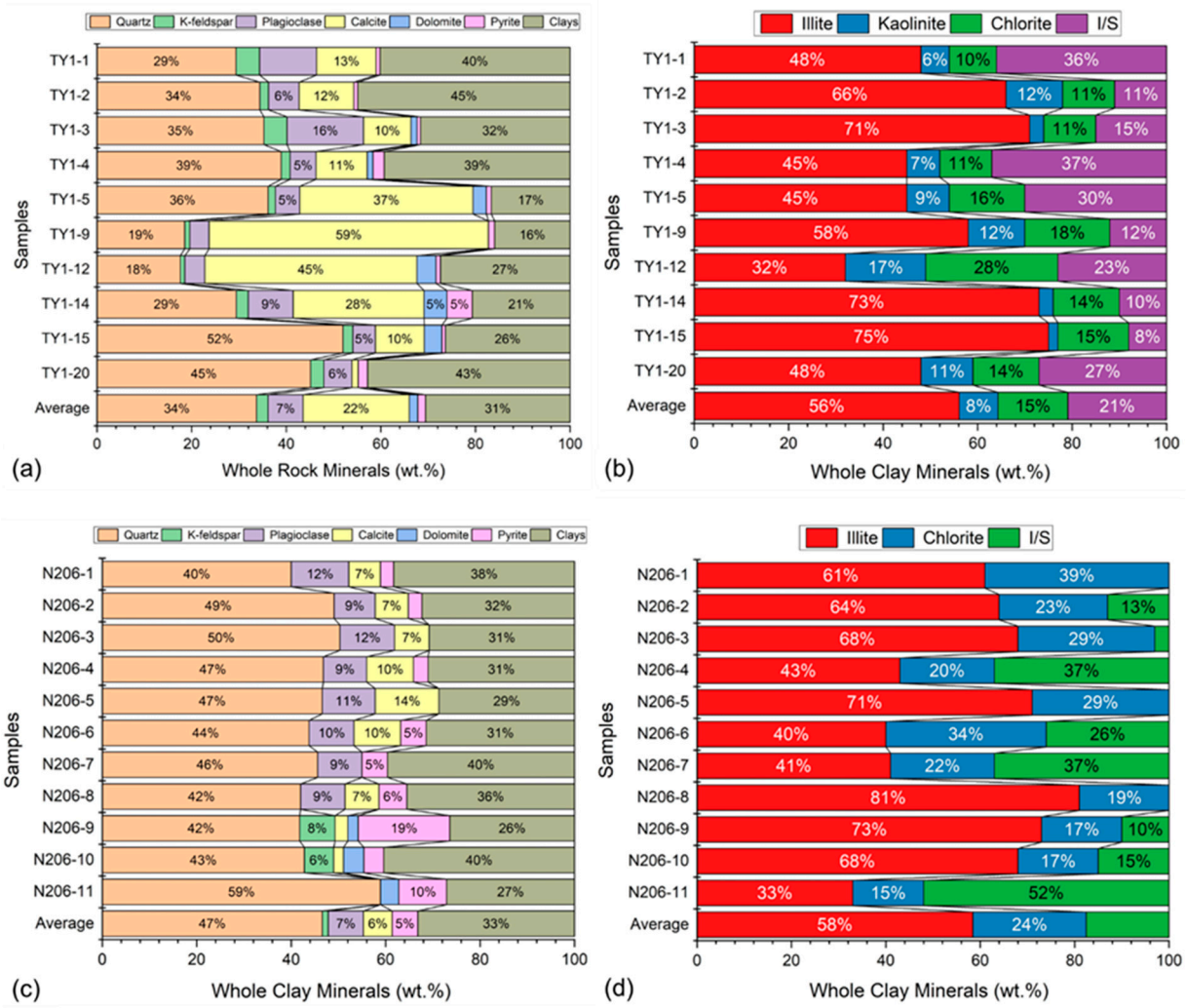

Figure 2. Shale mineral compositions of the two formations: whole rock minerals (**a**) TY1, (**c**) N206; clay minerals (**b**) TY1, (**d**) N206.

Clay content also shows marked variation. Longmaxi samples exhibit an average clay content of 30.62 wt%, with a broader range (16.53 wt%–44.87 wt%) across lithofacies. In contrast, Qiongzhusi shales are richer in clays overall (average 32.19 wt%) but show less compositional diversity. As illustrated in Figure 2b,d, and Table A4, clay mineral assemblages differ significantly. Illite dominates both formations, constituting 56.1% and 60.2% of the clay fraction in Longmaxi and Qiongzhusi samples, respectively. However, kaolinite is more prevalent in Longmaxi shales (average 8.2 wt%), whereas Qiongzhusi samples contain none. Conversely, Qiongzhusi shales exhibit a higher proportion of chlorite (24.2% vs. 14.8%) and mixed-layer illite/smectite (I/S) phases (15.6% vs. 20.9%). These compositional differences reflect distinct diagenetic histories, with kaolinite-rich Longmaxi samples indicating lower-temperature or moderate diagenetic environments [117], and the I/S- and chlorite-enriched Qiongzhusi samples reflecting more advanced diagenetic transformation and deeper burial conditions [118–120].

Collectively, the geochemical and mineralogical data highlight systematic compositional contrasts between the two shale formations. Longmaxi shales are more mineralogically diverse, often calcareous, and exhibit greater heterogeneity in clay mineralogy. In contrast, Qiongzhusi shales are compositionally more homogeneous, richer in quartz, illite,

and pyrite, and represent a deeply buried, over-mature system. These differences have direct implications for pore structure development, reservoir quality, and CO_2 sequestration behavior, which are discussed in subsequent sections.

3.2. SEM Characterization of Minerals, OM, and Associated Porosity

3.2.1. Clay–Quartz–OM Assemblages and OM-Hosted Pores

The SEM observations reveal the distinct morphological characteristics of clay–quartz–OM assemblages in the studied shale samples from the Longmaxi (TY1) and Qiongzhusi (N206) formations (Figure 3). In both the shale samples (a,b), authigenic quartz grains are closely associated with organic matter (OM) and clay minerals (primarily illite). In the Longmaxi samples, OM-hosted nanopores are abundant, well distributed around authigenic quartz (b). Meanwhile, the Qiongzhusi samples (c,d) exhibit a more clay-rich framework consisting mainly of illite and mixed-layer illite/smectite (I/S). OM occurs predominantly as elongated bands or discrete aggregates embedded within the clay matrix (c). The OM-hosted pores in the Qiongzhusi samples generally have smaller sizes and lower connectivity compared to those observed in the Longmaxi samples (d).

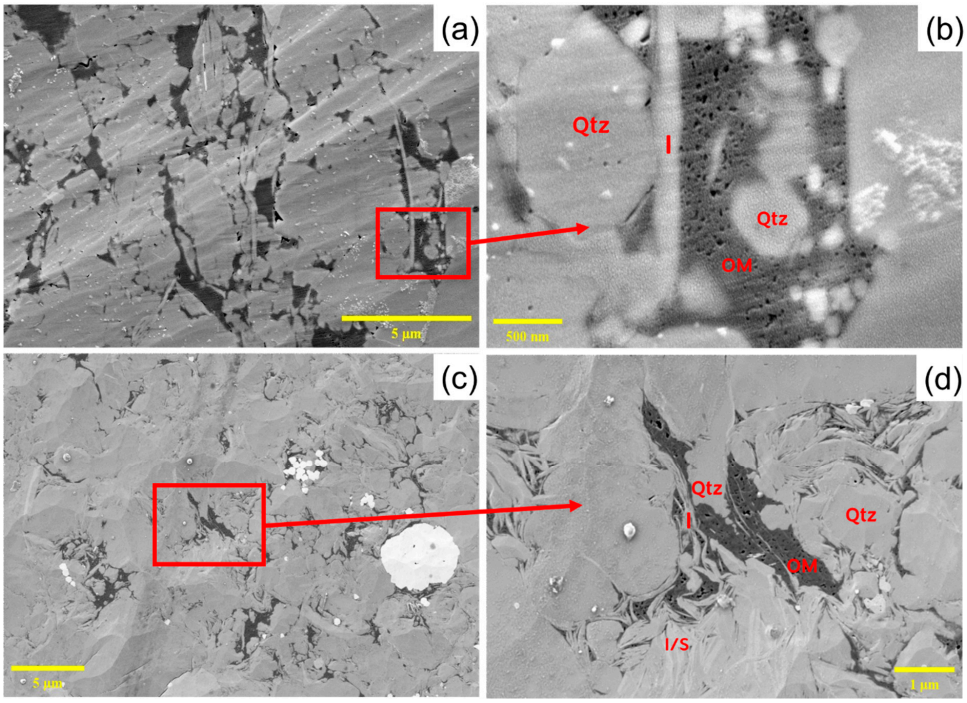

Figure 3. SEM images showing authigenic quartz (Qtz), clay minerals (illite and mixed-layer illite/smectite, I/S), and associated OM-hosted pores in the Longmaxi (TY1, (**a**,**b**)) and Qiongzhusi (N206, (**c**,**d**)) shales. (**a**,**b**) Quartz and clay minerals encapsulating OM with abundant nanopores. High magnification (**b**) highlights well-developed OM-hosted nanopores closely associated with quartz grains. (**c**,**d**) Clay-dominated matrix embedding elongated OM bands, with OM-hosted pores being relatively smaller and less uniform. Enlarged view (**d**) illustrates the interaction of OM with clay-rich phases and minor authigenic quartz.

During thermal maturation, clay minerals in shale reservoirs undergo systematic mineralogical transformations, typically transitioning from smectite through mixed-layer illite/smectite (I/S) phases to illite [121]. Concurrently, kaolinite may decrease significantly or undergo illitization, while chlorite and illite typically remain stable or form at higher maturities [122]. These processes are accompanied by dehydration, structural reorganization, increased crystallinity of illite, and substantial modifications to nano-scale pore systems. The release of water and elemental ions during clay mineral transformation promotes

authigenic quartz precipitation, further impacting the reservoir's pore characteristics and hydrocarbon storage capacity [117,121].

3.2.2. Nanoporous Organic Matter Within Clay Frameworks

Organic matter (OM) is preferentially distributed in zones where platy illite aggregates exhibit localized bending and structural disruption (Figure 4b,d). In these areas, the originally parallel-stacked illite lamellae display angular deflections, curvature, or partial separation, forming microscale voids or fractures. Organic matter appears to occupy these structurally weakened zones, often intercalated between bent or offset illite sheets. These OM-rich domains consistently host abundant nanopores, indicating that clay deformation may play a role in both concentrating organic matter and preserving organic-hosted porosity. In contrast, OM is rarely observed within undeformed, compact illite regions, suggesting a structural control on OM distribution and pore development.

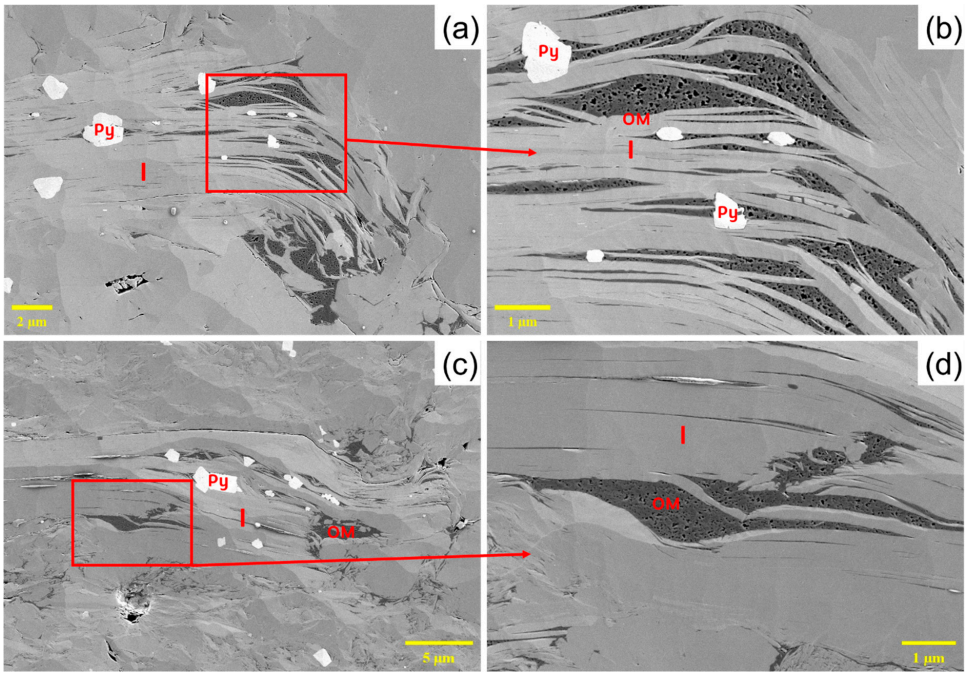

Figure 4. Representative SEM images showing platy illite (I) aggregates deformation and associated organic matter (OM), where abundant organic-hosted nanopores are preserved. (**a**,**b**) Longmaxi-TY1: layered illite platelets intercalated with porous OM and euhedral pyrite (Py); (**c**,**d**) Qiongzhusi-N206: OM domains embedded within platelets, forming well-developed OM-hosted pores.

3.2.3. Illite–Pyrite Aggregates with Porosity

Illite and pyrite often co-occur as mineral aggregates in the studied shale samples (Figure 5a–d). The illite displays a platy morphology with well-aligned lamellae, while pyrite occurs as both framboidal clusters and subhedral to euhedral crystals. In several cases (Figure 5a,c,d), organic matter is observed to be intimately intercalated within the illite–pyrite framework, forming continuous networks of nanopores. These OM-rich zones typically exhibit high pore densities and are spatially associated with disrupted or dislocated clay layers. In contrast, regions where illite and pyrite coexist without associated OM (Figure 5b) show very limited porosity, indicating that the presence of organic matter plays a critical role in generating and preserving nanoporous structures within these mineral assemblages. The comparison between the two formations highlights the critical role of organic matter not only in contributing to porosity but also in interacting with surrounding mineral phases to influence pore morphology and continuity. Illite appears to provide a

protective framework for OM-hosted pores, while pyrite may serve as a local structural anchor or diagenetic byproduct, depending on its morphology and distribution.

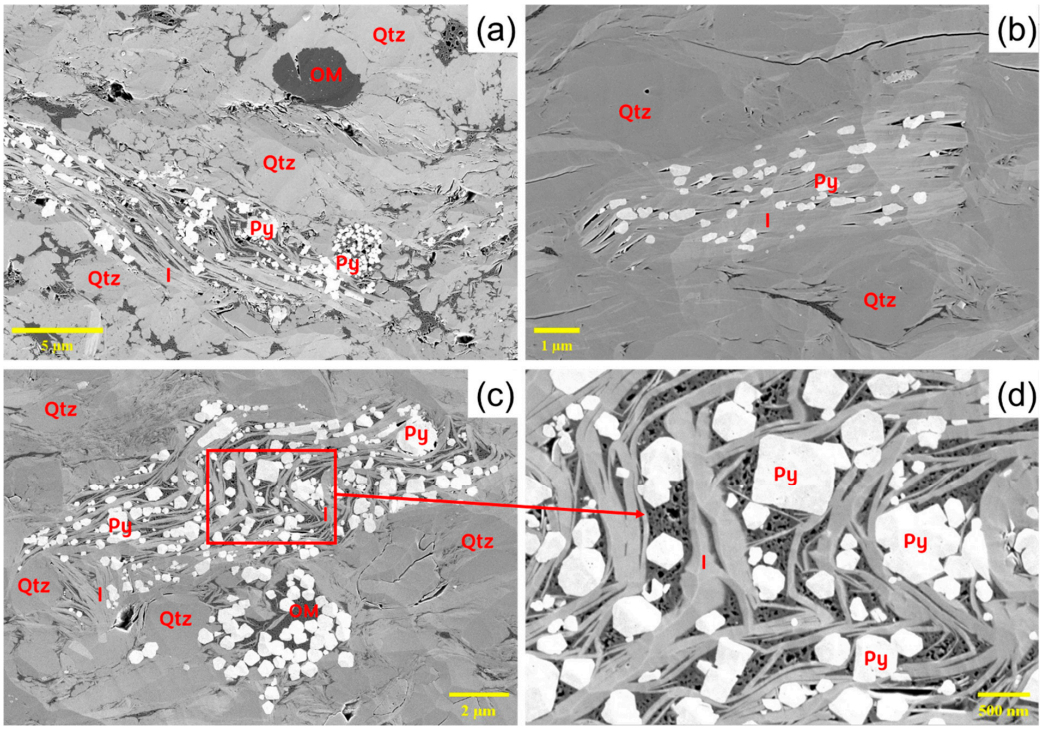

Figure 5. SEM images showing mineralogical assemblages composed of platy illite (I) and framboidal to euhedral pyrite (Py), with or without associated organic matter (OM), from the Longmaxi (TY1) and Qiongzhusi (N206) formations. (**a**,**b**) Samples from the Longmaxi Formation (TY1): (**a**) an illite–pyrite–quartz assemblage with patchy OM distribution and associated nanopores; (**b**) an illite–pyrite-rich zone lacking visible OM, showing limited pore development. (**c**,**d**) Samples from the Qiongzhusi Formation (N206): (**c**) widespread OM and pyrite grains distributed within illite–quartz matrices; (**d**) a close-up of (**c**), highlighting abundant porous OM interspersed between illite sheets and pyrite crystals. The presence or absence of OM appears to strongly influence local nanopore formation in these mineral aggregates.

3.2.4. Nanoporous Organic Matter and Pyrite

The contrasting pyrite–organic matter (Py–OM) relationships observed between the Longmaxi and Qiongzhusi shale samples reveal significant implications for OM pore evolution. In the Longmaxi Formation (Figure 6a), pyrite commonly occurs as fine framboids or dispersed subhedral crystals within or adjacent to OM, suggesting early diagenetic precipitation under euxinic conditions. The abundant nanoscale pores (Figure 6b) surrounding intercrystalline pyrite indicate that these particles may help preserve local pore pressure gradients or prevent OM compaction during burial.

In contrast, the Qiongzhusi Formation features large, closely packed, and often euhedral pyrite crystals that frequently encapsulate OM fragments (Figure 6e,f). Such textures imply late diagenetic or even epigenetic pyrite growth (Figure 6g) during deeper burial stages or sulfur-rich fluid influx. This mode of pyrite formation is detrimental to OM porosity for two reasons: First, the mechanical confinement by pyrite overgrowth reduces space for pore expansion during OM cracking; second, the absence of framboidal textures suggests a loss of the early microbial sulfate reduction signal, potentially reflecting deeper redox conditions that coincide with lower porosity preservation.

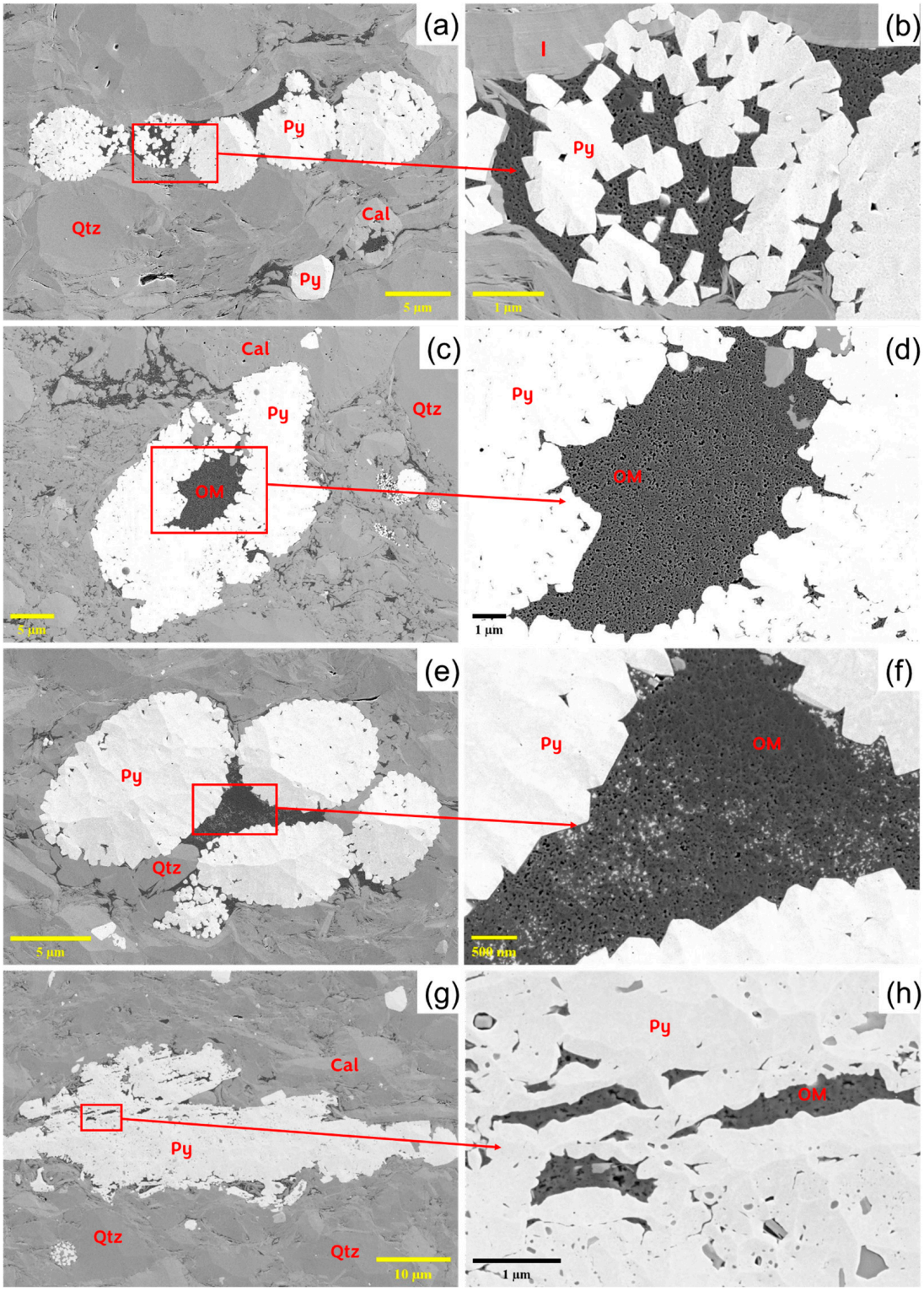

Figure 6. SEM images illustrating the associations between pyrite (Py) and organic matter (OM), and their influence on OM-hosted pore development in the Longmaxi (**a**–**d**) and Qiongzhusi (**e**–**h**) shales. (**a**–**d**) Samples from the Longmaxi Formation. OM is intergrown with framboidal to euhedral pyrite crystals, indicating early diagenetic formation. Enlarged views (**b**,**d**) show abundant and well-developed nanopores within OM, especially surrounding dispersed pyrite. (**e**–**h**) Samples from the Qiongzhusi Formation. OM is encapsulated by large, aggregated pyrite crystals with more euhedral shapes. High-magnification images (**f**,**h**) reveal fewer and less connected nanopores within OM, suggesting pore occlusion or limited pore generation during pyrite overgrowth. Cal: calcite; Qtz: quartz; I: illite.

3.2.5. Pore Characteristics in Discrete Organic Matter

Figure 7 highlights significant variability in pore characteristics within discrete organic matter (OM) observed in Longmaxi (TY1; Figure 7a–d) and Qiongzhusi (N206; Figure 7e–h) shale samples. These pore networks show distinct differences not only in their size, density, and connectivity but also in their structural association with adjacent mineral phases.

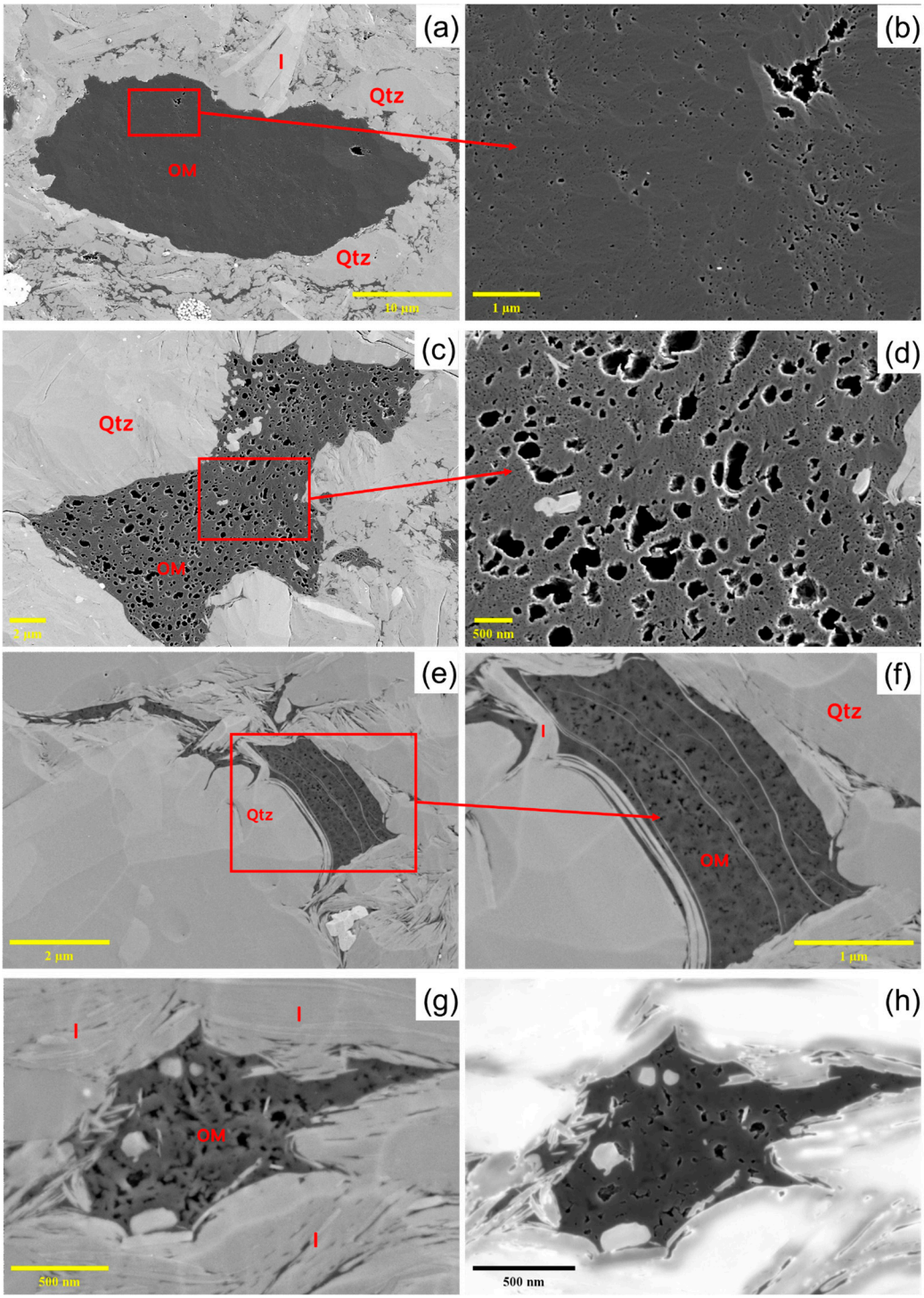

Figure 7. Morphology and pore structure of isolated organic matter in the Longmaxi (**a**–**d**) and Qiongzhusi (**e**–**h**) shale samples. (**a**,**c**,**e**,**g**) show isolated OM particles (labeled OM) embedded within quartz (Qtz) and clay minerals (mainly illite, I); (**b**,**d**,**f**) are magnified views from the red boxes in (**a**,**c**,**e**), respectively, highlighting intraparticle OM-hosted pores; (**h**) is the InLens mode image of (**g**), captured at the same resolution to enhance pore–OM contrast.

In the Longmaxi shale samples (Figure 7a–d), discrete OM exhibits varying degrees of pore development. OM occurs as discrete sub-rounded to irregular particles within a quartz-dominated matrix. Some OM aggregates appear relatively massive with minimal visible porosity (Figure 7a,b). However, other OM domains (Figure 7c,d) exhibit abundant, well-developed nanopores with high connectivity, likely a result of effective organic matter maturation and gas generation. Such heterogeneity suggests differential thermal maturity or OM variations within the Longmaxi Formation.

OM in the Qiongzhusi shale samples (Figure 7e–h) also shows well-developed nanopores, albeit smaller and generally less interconnected compared to highly porous OM in Longmaxi shales. OM-hosted pores in these samples are more irregular and sparsely distributed, although localized dense pore clusters are still observed (f,g). Here, the OM is frequently embedded within layered clay (illite) aggregates, suggesting that clay minerals might impose mechanical constraints, reducing pore expansion and connectivity during OM maturation. The InLens image (h) highlights the sharp boundary between OM and adjacent mineral phases and reveals OM pores with complex internal structures.

3.2.6. Distribution and Pore Features of Accessory Minerals

This section presents the occurrence and pore characteristics of accessory minerals not yet discussed in previous sections, including calcite, dolomite, anatase, albite, and apatite, as observed in SEM images (Figure 8).

In both Longmaxi (TY1) and Qiongzhusi (N206) shale samples, calcite (Cal) is identified as a common cementing mineral. It typically occurs as isolated grains or aggregates, rarely in direct association with organic matter (OM). Intragranular pores within calcite grains are occasionally observed (Figure 8a,b). These pores are interpreted as either dissolution-induced secondary pores or growth-related defects such as cleavage voids or crystallographic interstices formed during precipitation.

Anatase (Ana), a TiO_2 polymorph, is identified as discrete grains within clay matrices or in close association with OM. In the TY1 sample, anatase appears as a porous aggregate (Figure 8c), with its magnified view (Figure 8d) revealing well-developed submicron intercrystalline pores.

Moreover, the particle displays two distinct grayscale phases: brighter microcrystalline anatase near the pore walls and darker, platy internal features. Given its association with surrounding clay minerals and elevated Fe content from EDS, the darker phase may represent Fe–Ti-rich illite or illite-like minerals, possibly formed via alteration or co-precipitation. This textural contrast supports a complex growth or replacement history.

In the Qiongzhusi Formation, anatase crystals are frequently embedded within organic matter (Figure 8e), coexisting with pyrite. The close-up view (Figure 8f) shows anatase crystals intricately intertwined with OM nanopores. Compared to unmineralized OM, the growth of anatase appears to have partially filled preexisting OM-hosted pores and overprinted earlier pyrite textures. These anatase-bearing regions may indicate hydrothermal fluid influence, which not only promoted Ti mobilization and crystallization but also contributed additional heat. Such processes could enhance organic maturity, reduce pore preservation, and suppress new pore formation in overmature OM—consistent with the observed Ro values of 3.62%–4.58% in the Qiongzhusi shale.

Figure 8g shows a later-stage anatase grain that is more compact and pore-free, encapsulating scattered OM fragments. This texture likely represents an evolved stage of anatase crystallization, where progressive growth has displaced OM and obliterated associated pores. The comparison between Figure 8e and g may help explain the reduced porosity commonly observed in the Qiongzhusi shale. Finally, Figure 8h illustrates a mineralogically diverse zone from the N206 sample, where apatite, albite, calcite, dolomite, quartz, pyrite,

anatase, and OM coexist. These assemblages reflect a complex paragenesis involving multiple diagenetic episodes and potential hydrothermal overprinting.

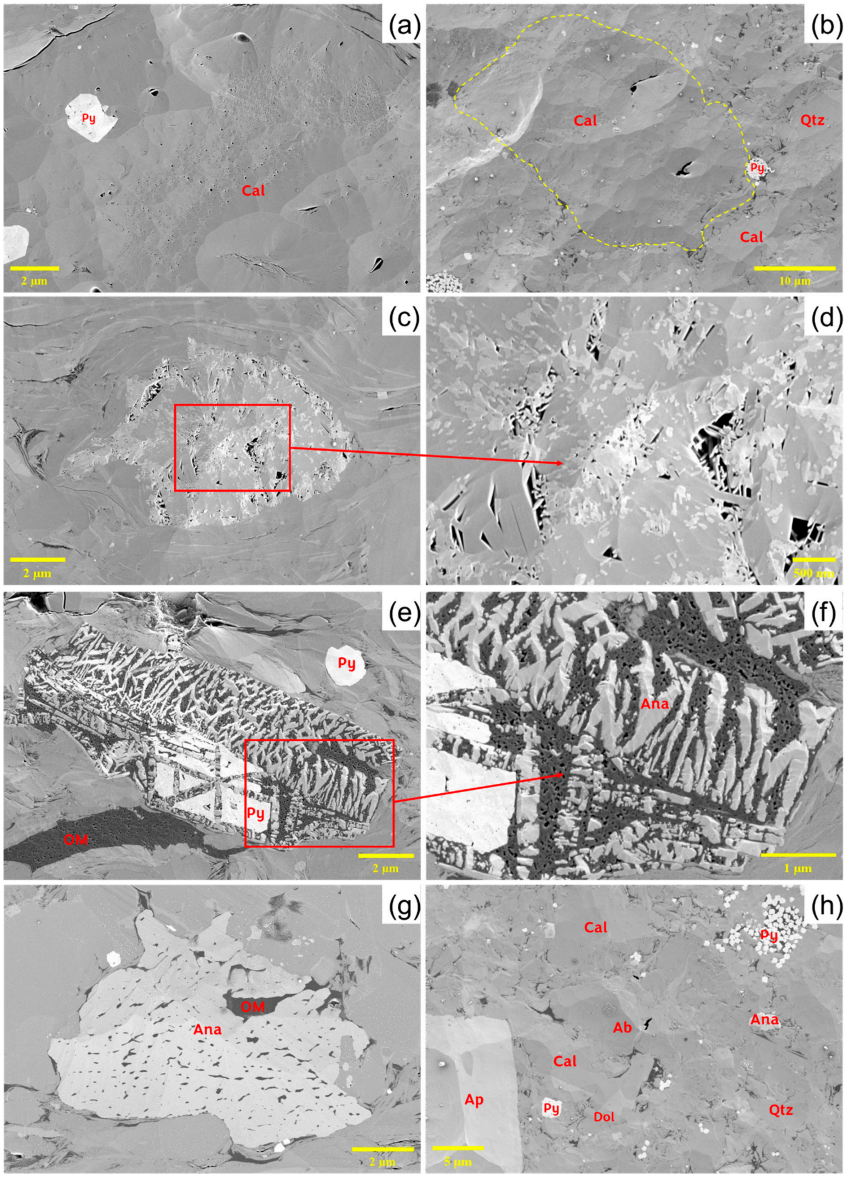

Figure 8. SEM images showing grains with associated porosity. (**a**) Calcite in Longmaxi shale (TY1) exhibiting sparse intragranular pores and embedded pyrites; (**b**) calcite in Qiongzhusi shale (N206), with localized intergranular pores; (**c**) porous anatase aggregate in TY1 sample; (**d**) magnified view of the region in (**c**), revealing submicron-scale intercrystalline pores. (**e**) Coexistence of anatase, pyrite, and organic matter in N206 shale; (**f**) close-up of (**e**) displaying anatase developed in OM nanopores; (**g**) compact anatase grain in N206 shale, embedded in non-porous OM, (**h**) mineralogical diversity in N206 shale. Ab: albite, Ana: Anatase, Ap: Apatite, Cal: Calcite, Dol: Dolomite, OM: Organic matter, Py: pyrite, Qtz: Quartz.

3.3. CO_2/N_2 Adsorption Isotherms and Pore Size Distribution

To systematically characterize the pore structures of the Longmaxi and Qiongzhusi shale samples, MICP, CO_2, and N_2 adsorption experiments were employed. The adsorption behaviors for CO_2 and N_2 reflect differences in pore characteristics such as pore size distribution, pore connectivity, and morphology between the two shale formations.

Low-pressure CO_2 adsorption curves (Figure 9a,b) obtained from the samples demonstrate Type I characteristics according to the IUPAC classifications [48]. From Table 2, the

micropore volumes for Longmaxi samples range from 0.001 to 0.008 cc/g with an average of 0.0038 cc/g, whereas those for the Qiongzhusi samples display a slightly narrower variation between 0.002 and 0.006 cc/g, averaging slightly higher at 0.0044 cc/g. Micropore surface areas from CO_2 adsorption are comparable between the two groups; however, the Qiongzhusi shales show slightly higher average micropore surface area (11.139 m^2/g) than the Longmaxi samples (10.99 m^2/g). Additionally, adsorption energies are generally similar, with Longmaxi shales averaging slightly higher adsorption energy (30.145 kJ/mol) compared to Qiongzhusi samples (29.421 kJ/mol), suggesting marginally stronger adsorption interactions in Longmaxi micropores.

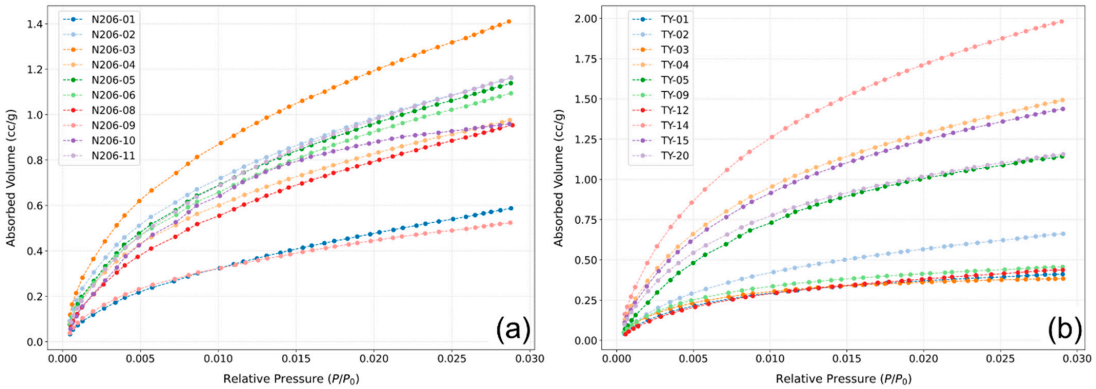

Figure 9. Low-pressure CO_2 adsorption curves of (**a**) Qiongzhusi (N206) and (**b**) Longmaxi (TY1) shales.

Table 2. MICP, low-pressure CO_2, and N_2 sorption analysis results.

Formation	Sample ID	CO_2 Sorption			N_2 Sorption		MICP	
		Micropore Volume (cc/g)	Micropore Surface Area (m^2/g)	Adsorption Energy (kJ/mol)	Pore Volume (cc/g)	MultiPoint BET Surface Area (m^2/g)	Pore Volume (cc/g)	Surface Area (m^2/g)
Longmaxi	TY1-1	0.002	4.768	32.256	0.0108	8.165	0.0025	0.7318
	TY1-2	0.005	15.027	27.437	0.0208	21.64	0.0024	0.53
	TY1-3	0.006	16.746	29.565	0.0213	23.21	0.0042	1.2
	TY1-4	0.001	3.866	34.001	0.0091	7.018	0.0025	0.71
	TY1-5	0.003	7.508	29.354	0.0142	14.73	0.0035	0.88
	TY1-9	0.001	4.492	31.069	0.0126	11.64	0.0035	0.88
	TY1-12	0.002	4.975	29.67	0.0137	11.85	0.0028	0.74
	TY1-14	0.008	22.698	29.246	0.0336	33.03	0.0068	2.03
	TY1-15	0.006	16.67	29.062	0.0261	24.13	0.0038	1.11
	TY1-20	0.004	13.153	29.793	0.0252	20.94	0.0062	2.0898
Average	/	0.0038	10.99	30.145	0.0187	17.635	0.0038	1.09
Qiongzhusi	N206-1	0.003	6.685	28.24	0.0105	2.925	0.0028	0.0121
	N206-2	0.005	12.222	30.385	0.0154	5.899	0.0034	0.0195
	N206-3	0.006	14.851	30.317	0.0142	6.999	0.0101	0.0445
	N206-4	0.004	10.302	30.317	0.0135	5.662	0.0123	0.0553
	N206-5	0.005	12.706	29.259	0.0112	5.614	0.0029	0.0143
	N206-6	0.005	12.043	29.464	0.0132	5.266	0.0082	0.0338
	N206-8	0.004	10.909	28.589	0.0124	2.819	0.0035	0.022
	N206-9	0.002	5.675	29.943	0.0067	1.761	0.0059	0.0151
	N206-10	0.005	12.646	29.062	0.0109	2.229	0.0094	0.0339
	N206-11	0.005	13.355	28.636	0.0107	2.256	0.0056	0.0375
Average	/	0.0044	11.139	29.421	0.0119	4.143	0.0064	0.0288

N_2 sorption isotherms for the Qiongzhusi (N206) and Longmaxi (TY1) shales are presented in Figure 10a,b. The sorption curves for both formations exhibit characteristics

typical of Type IV isotherms according to the IUPAC classification (Figure 11), indicating the dominance of mesoporous structures [48]. At low relative pressures ($P/P_0 < 0.4$), the adsorption volume increases gradually, corresponding primarily to monolayer adsorption, and is indicative of microporous and small mesoporous structures (<4 nm). As relative pressure approaches unity ($P/P_0 > 0.9$), adsorption volume rises sharply, reflecting capillary condensation in larger mesopores and macropores.

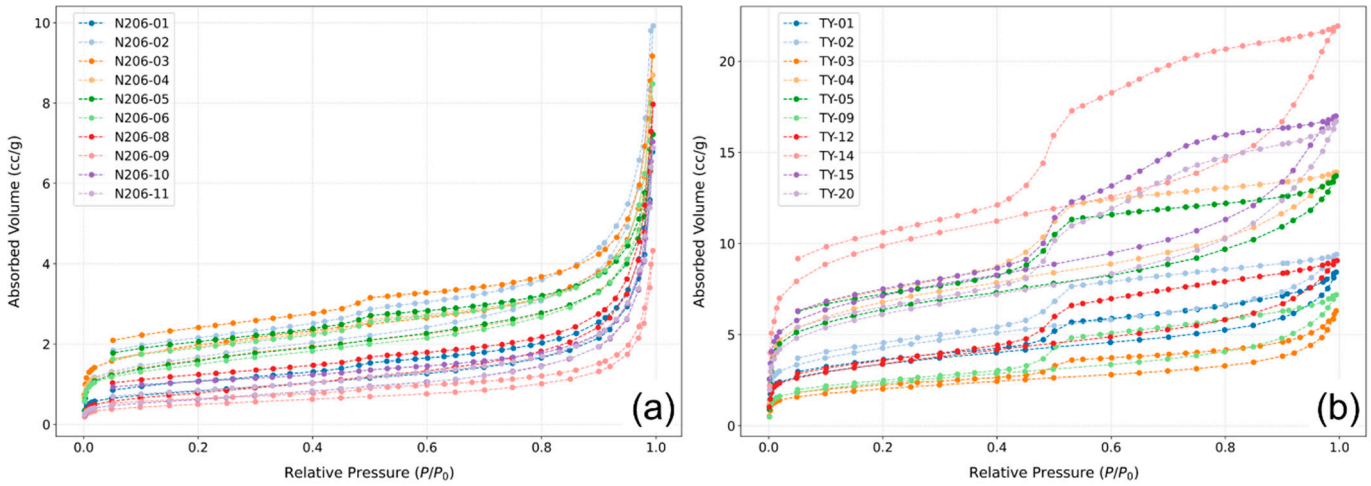

Figure 10. Low-pressure N_2 sorption isotherms from (**a**) Qiongzhusi (N206) and (**b**) Longmaxi (TY1) shales.

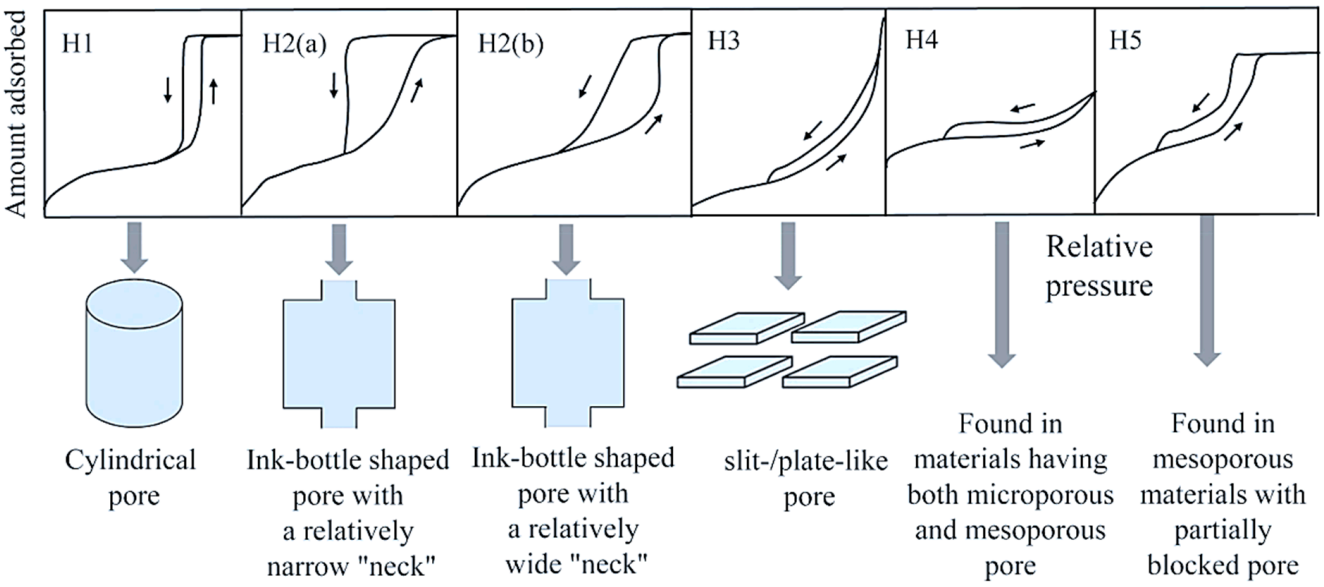

Figure 11. Sorption hysteresis types and representative pore structures [123].

A notable difference between the two shale groups is reflected in the morphology of their hysteresis loops. The Qiongzhusi (N206) shales exhibit hysteresis loops predominantly resembling the H3 type (Figure 10), suggesting slit-like or plate-like pore structures [123], indicative of pores associated with clay mineral aggregates and layered organic matter. In contrast, the Longmaxi (TY1) shales exhibit more varied hysteresis loops, predominantly showing Type H2(a) and H2(b) hysteresis loops [123]. These loop types typically correspond to ink-bottle-shaped pores with narrower necks (H2(a)) and wider necks (H2(b)) [123], indicating the prevalence of ink-bottle pores and complex interconnected networks within organic matter and clay aggregates (Figure 11).

Table 2 collects the pore characteristics of the two formations. The Longmaxi shales exhibit considerably larger pore volumes of N_2 adsorption, ranging from 0.0091 to 0.0336 cc/g (average of 0.0187 cc/g), compared to the Qiongzhusi samples, which display pore volumes between 0.0067 and 0.0154 cc/g (average of 0.0119 cc/g). Multi-point BET surface areas for Longmaxi shales are significantly greater, varying from 7.018 to 33.03 m^2/g, with an average of 17.635 m^2/g. In contrast, the BET surface areas of the Qiongzhusi shales are considerably lower, ranging only from 1.761 to 6.999 m^2/g (average of 4.143 m^2/g). These results indicate a higher overall porosity and a more developed mesoporous structure within the Longmaxi shale samples.

MICP-derived pore volumes are lower in the Longmaxi shales, ranging from 0.0024 to 0.0068 cc/g (average of 0.0038 cc/g), compared to Qiongzhusi samples, which range from 0.0028 to 0.0123 cc/g, averaging 0.0064 cc/g. Furthermore, surface areas from MICP for the Longmaxi samples range from 0.53 to 2.0898 m^2/g, averaging around 1.09 m^2/g, whereas the Qiongzhusi samples display slightly larger variation and much lower values, ranging from 0.0121 to 0.0553 m^2/g, averaging at 0.0288 m^2/g.

Pore size distribution plots (Figure 12a,b) integrated from MICP, CO_2, and N_2 sorption analyses provide a detailed comparative view of the two formations. The Qiongzhusi shale pores predominantly fall within the micropore range (<2 nm), with prominent peaks below 1 nm, accompanied by sparse development of mesopores (2–50 nm) and rare macropores (>50 nm). In comparison, Longmaxi samples show a significant mesopore population centered predominantly in the 2–10 nm range. This indicates Longmaxi shales have better-developed mesoporosity, possibly due to distinct mineral assemblages and organic structures compared to the Qiongzhusi shales.

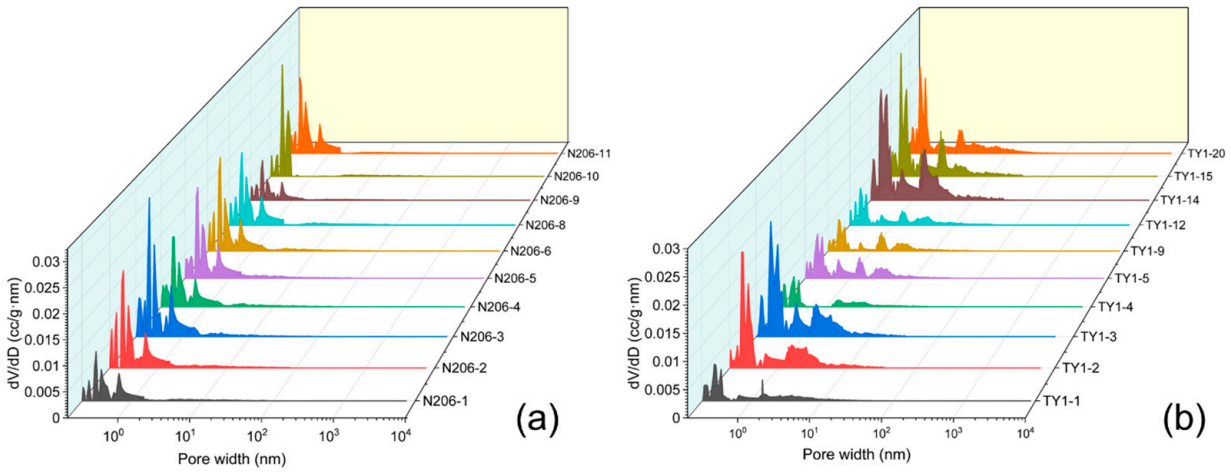

Figure 12. Pore size distributions obtained from MICP and low-pressure gas (CO_2 and N_2) sorption experiments: (**a**) Qiongzhusi (N206) and (**b**) Longmaxi (TY1) shales.

3.4. Multifractality of Pore Structures

Low-pressure CO_2 and N_2 adsorption isotherms obtained from the samples were used to derive log–log plots of the partition function $u(q,\varepsilon)$ vs. the length scale ε for q values ranging from −10 to 10 (at successive q = 1 intervals) (Figures 13 and 14). The plots reveal the existence of a linear relationship between $\log u(q,\varepsilon)$ and $\log\varepsilon$ for all samples, thus exhibiting the multifractal behaviors of the micropore and mesopore PSD curves. Furthermore, the linear trend lines are also observed to be respectively characterized by negative and positive slopes for $q < 0$ and $q > 0$.

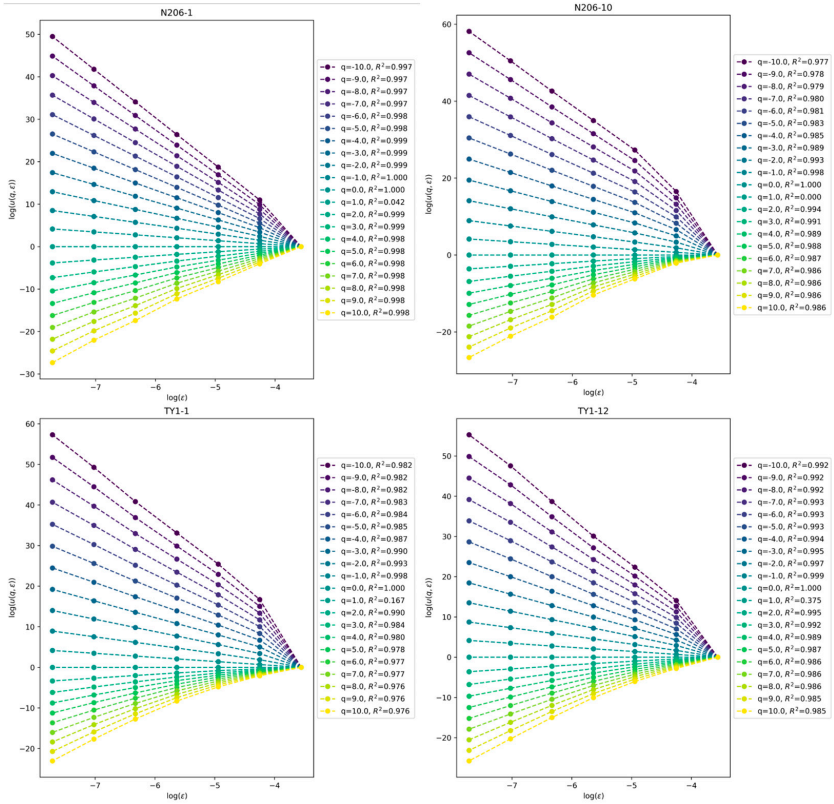

Figure 13. Log–log plots of partition function against length for Qiongzhusi (N206) and Longmaxi (TY1) samples obtained from low-pressure CO_2 adsorption isotherms.

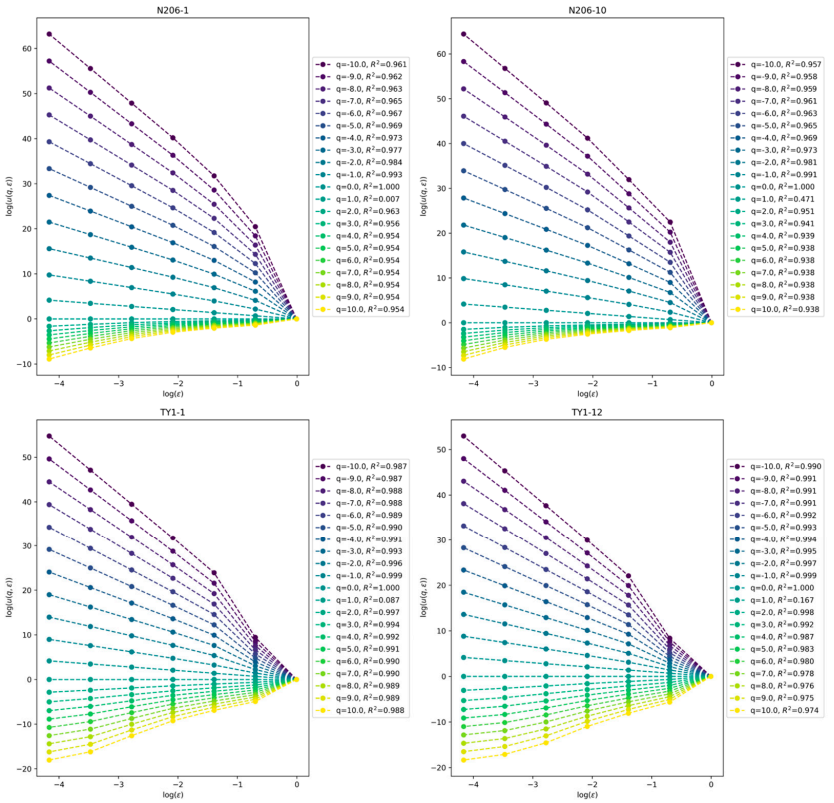

Figure 14. Log–log plots of partition function against length for Qiongzhusi (N206) and Longmaxi (TY1) samples obtained from low-pressure N_2 adsorption isotherms.

Multifractal analysis of pore structures using low-pressure CO_2 adsorption data reveals distinct microporous characteristics for Qiongzhusi (N206) and Longmaxi (TY1) shales. The generalized dimensions D_q from low-pressure CO_2 adsorption data obtained from the samples are presented in Figure 15.

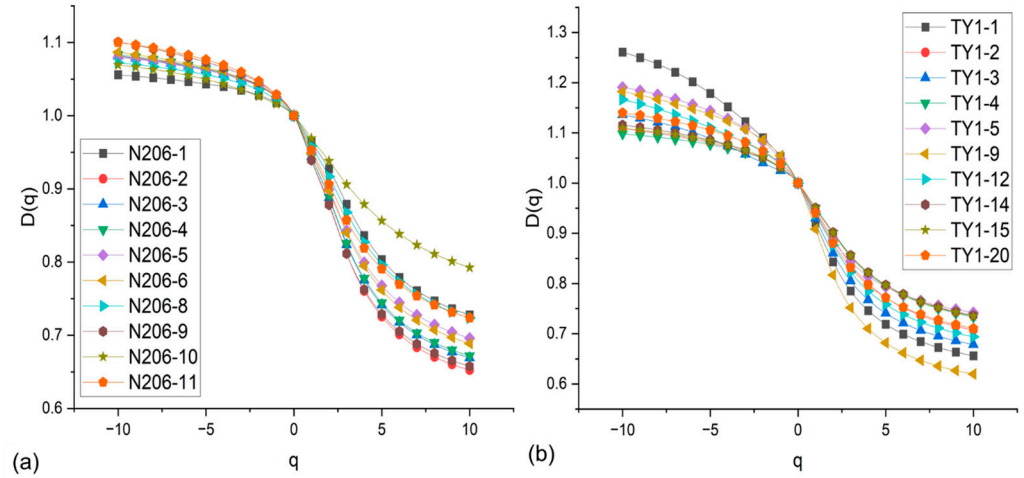

Figure 15. Relationship between D_q and q from low-pressure CO_2 adsorption data for (**a**) N206 and (**b**) TY1.

D_0 represents the fractal behavior of non-empty boxes characterized by a porosity under successive finer partitions that is not dependent on the probability of porosity within the box [124,125]. Table 3 reveals that all samples are characterized by the same D_0. D_1 represents entropy information for PSD along pore size intervals; the degree of distribution uniformity for PSD across specific pore size ranges can be represented by the D_0-D_1 indicator [125,126]. Table 4 shows that the Longmaxi samples have higher D_0-D_1 values (0.0622) on average compared to the Qiongzhusi samples (0.0490). This suggests that the micropore PSD style of the Longmaxi formation is more clustered, with PSD for the Qiongzhusi Formation being more homogenous.

Table 3. Micropore generalized dimensions from low-pressure CO_2 adsorption data.

Formation	Sample	D_{10+}	D_{10-}	D_0	D_1	D_2	$D_0 - D_1$	$D_{10-} - D_{10+}$	H
Longmaxi	TY1-1	0.6561	1.2610	1.0000	0.9215	0.8429	0.0785	0.6049	0.9215
	TY1-2	0.7070	1.1091	1.0000	0.9451	0.8902	0.0549	0.4021	0.9451
	TY1-3	0.6784	1.1362	1.0000	0.9301	0.8602	0.0699	0.4578	0.9301
	TY1-4	0.7335	1.0982	1.0000	0.9501	0.9001	0.0499	0.3647	0.9501
	TY1-5	0.7419	1.1910	1.0000	0.9430	0.8860	0.0570	0.4491	0.9430
	TY1-9	0.6197	1.1824	1.0000	0.9084	0.8167	0.0916	0.5628	0.9084
	TY1-12	0.6940	1.1664	1.0000	0.9382	0.8764	0.0618	0.4723	0.9382
	TY1-14	0.7364	1.1159	1.0000	0.9510	0.9019	0.0490	0.3795	0.9510
	TY1-15	0.7350	1.1092	1.0000	0.9504	0.9008	0.0496	0.3742	0.9504
	TY1-20	0.7103	1.1400	1.0000	0.9404	0.8808	0.0596	0.4296	0.9404
Average	/	0.7012	1.1509	1.0000	0.9378	0.8756	0.0622	0.4497	0.9378
Qiongzhusi	N206-1	0.7277	1.0560	1.0000	0.9637	0.9274	0.0363	0.3283	0.9637
	N206-2	0.6523	1.0817	1.0000	0.9399	0.8798	0.0601	0.4294	0.9399
	N206-3	0.6690	1.0813	1.0000	0.9438	0.8877	0.0562	0.4123	0.9438
	N206-4	0.6718	1.0834	1.0000	0.9443	0.8885	0.0557	0.4116	0.9443
	N206-5	0.6960	1.0797	1.0000	0.9496	0.8991	0.0504	0.3837	0.9496
	N206-6	0.6887	1.0869	1.0000	0.9489	0.8978	0.0511	0.3982	0.9489
	N206-8	0.7234	1.0724	1.0000	0.9585	0.9170	0.0415	0.3489	0.9585
	N206-9	0.6576	1.1009	1.0000	0.9391	0.8782	0.0609	0.4432	0.9391
	N206-10	0.7926	1.0694	1.0000	0.9690	0.9381	0.0310	0.2768	0.9690
	N206-11	0.7236	1.1002	1.0000	0.9530	0.9061	0.0470	0.3765	0.9530
Average	/	0.7003	1.0812	1.0000	0.9510	0.9020	0.0490	0.3809	0.9510

Table 4. Micropore multifractal singularity characteristics from low-pressure CO_2 adsorption data.

Formation	Sample	α_{10+}	α_{10-}	α_0	$\alpha_{10-} - \alpha_{10+}$	$\alpha_0 - \alpha_{10+}$	$\alpha_{10-} - \alpha_0$	R_d
Longmaxi	TY1-1	0.5968	1.3709	1.0531	0.7741	0.4563	0.3178	0.1385
	TY1-2	0.6448	1.1566	1.0312	0.5117	0.3864	0.1253	0.2611
	TY1-3	0.6184	1.2044	1.0248	0.5860	0.4064	0.1796	0.2268
	TY1-4	0.6729	1.1295	1.0302	0.4566	0.3573	0.0993	0.2580
	TY1-5	0.6907	1.2597	1.0483	0.5690	0.3576	0.2114	0.1462
	TY1-9	0.5623	1.2555	1.0548	0.6932	0.4925	0.2007	0.2918
	TY1-12	0.6322	1.2543	1.0379	0.6221	0.4057	0.2164	0.1893
	TY1-14	0.6765	1.1626	1.0311	0.4861	0.3545	0.1315	0.2230
	TY1-15	0.6736	1.1467	1.0315	0.4730	0.3578	0.1152	0.2426
	TY1-20	0.6499	1.1920	1.0392	0.5420	0.3892	0.1528	0.2364
Average	/	0.6418	1.2132	1.0382	0.5714	0.3964	0.1750	0.2214
Qiongzhusi	N206-1	0.6589	1.0754	1.0177	0.4166	0.3588	0.0577	0.3011
	N206-2	0.5886	1.1077	1.0274	0.5192	0.4389	0.0803	0.3585
	N206-3	0.6046	1.1111	1.0263	0.5064	0.4217	0.0847	0.3370
	N206-4	0.6073	1.1132	1.0266	0.5060	0.4193	0.0867	0.3326
	N206-5	0.6303	1.1059	1.0256	0.4756	0.3953	0.0803	0.3150
	N206-6	0.6227	1.1205	1.0259	0.4978	0.4032	0.0946	0.3085
	N206-8	0.6555	1.0967	1.0220	0.4413	0.3665	0.0747	0.2918
	N206-9	0.5948	1.1464	1.0291	0.5517	0.4343	0.1174	0.3169
	N206-10	0.7256	1.0978	1.0161	0.3722	0.2905	0.0817	0.2088
	N206-11	0.6596	1.1356	1.0286	0.4760	0.3690	0.1070	0.2620
Average	/	0.6348	1.1110	1.0245	0.4763	0.3898	0.0865	0.3032

D_2 is known as the correlation dimension, which factors the behavior of the second sampling moments [70,125,126]. Furthermore, the Hurst exponent H, which is defined by $(D_2 + 1)/2$, is an indication of the positive autocorrelation intensity and can be used to explain the pore connectivity across various pore size networks [70]. Longmaxi shales display a lower average H (0.9378) than the Qiongzhusi shales (H = 0.9510).

A subtraction of D_{10+} from D_{10-} can be used to examine the heterogeneity of microporosity distribution over the pore size range measured by low-pressure CO_2 adsorption [47]. The generalized dimension spectra (Figure 15) and Table 3 demonstrate that Longmaxi shales exhibit a wider range of dimensions (D_{10-} to D_{10+}) compared to the Qiongzhusi shales, indicating higher micropore structural complexity and heterogeneity within Longmaxi samples. This finding also agrees with the previous observation of the Qiongzhusi samples having a lower degree of PSD heterogeneity [5,8,127].

Multifractal singularity analysis offers additional insights. All samples (Figure 16 and Table 4) exhibit a strong asymmetric (as α approaches 1) convex parabolic shape, with Longmaxi samples exhibiting broader $\alpha_0 - \alpha_{10+}$ and $\alpha_{10-} - \alpha_0$ ranges.

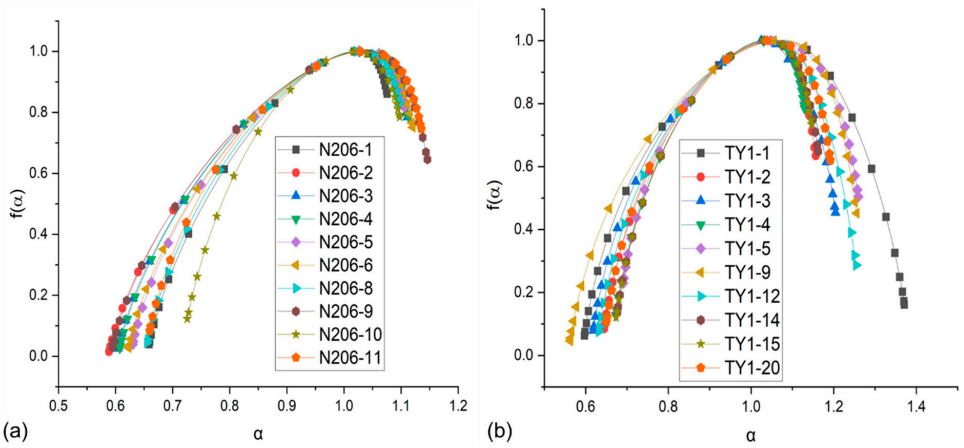

Figure 16. Multifractal singularity from low-pressure CO_2 adsorption data for (**a**) N206 and (**b**) TY1.

The calculated fractal parameters from the plots reveal that, on average, the Longmaxi samples are characterized by higher values of α_0, α_{10-}, α_{10+}, $\alpha_{10-} - \alpha_{10+}$, $\alpha_0 - \alpha_{10+}$, and $\alpha_{10-} - \alpha_0$ (Table 4). Specifically, the Rd parameter (obtained from $(\alpha_0 - \alpha_{10+}) - (\alpha_{10} - \alpha_0)$), quantifying the symmetry and heterogeneity of micropore distributions, averages 0.2214 in Longmaxi versus 0.3032 in Qiongzhusi samples. Furthermore, the observation of an averagely higher α_0 in the Longmaxi samples suggests that, compared to the Qiongzhusi samples, the concentration of PSD over a specific pore size range is at a higher level.

These findings collectively underline that Longmaxi shale microporosity is significantly more heterogeneous and spatially variable, reflecting diverse micropore structures. In contrast, the Qiongzhusi shales demonstrate a comparatively homogeneous microporosity distribution, likely related to their high thermal maturity and more uniform pore structural evolution under deeper environmental pressure.

In addition to the CO_2-based multifractal characterization of microporous structures, low-pressure N_2 adsorption data were employed to further investigate mesopore-to-macropore heterogeneity in the Qiongzhusi (N206) and Longmaxi (TY1) shales. The generalized dimension spectra D_q versus q, derived from the partition function u(q,ε) across a range of moment orders (q = −10 to 10), are presented in Figure 16, with detailed fractal parameters summarized in Table 5.

Table 5. Mesopore–macropore generalized dimensions obtained from low-pressure N_2 adsorption data.

Formation	Sample	D_{10+}	D_{10-}	D_0	D_1	D_2	$D_0 - D_1$	$D_{10-} - D_{10+}$	H
Longmaxi	TY1-1	0.4529	1.1986	1.0000	0.8277	0.6553	0.1723	0.7457	0.8277
	TY1-2	0.4115	1.1643	1.0000	0.8402	0.6804	0.1598	0.7528	0.8402
	TY1-3	0.4084	1.2231	1.0000	0.7950	0.5900	0.2050	0.8148	0.7950
	TY1-4	0.3205	1.1928	1.0000	0.7912	0.5824	0.2088	0.8724	0.7912
	TY1-5	0.3100	1.2345	1.0000	0.7804	0.5608	0.2196	0.9245	0.7804
	TY1-9	0.4714	1.1952	1.0000	0.8336	0.6671	0.1664	0.7238	0.8336
	TY1-12	0.4835	1.1630	1.0000	0.8608	0.7217	0.1392	0.6795	0.8608
	TY1-14	0.3501	1.2418	1.0000	0.8048	0.6097	0.1952	0.8916	0.8048
	TY1-15	0.4589	1.1954	1.0000	0.8596	0.7191	0.1404	0.7366	0.8596
	TY1-20	0.5186	1.1997	1.0000	0.8693	0.7387	0.1307	0.6811	0.8693
Average	/	0.4186	1.2008	1.0000	0.8263	0.6525	0.1737	0.7823	0.8263
Qiongzhusi	N206-1	0.2803	1.2313	1.0000	0.7186	0.4371	0.2814	0.9511	0.7186
	N206-2	0.3376	1.2276	1.0000	0.7532	0.5063	0.2468	0.8900	0.7532
	N206-3	0.2404	1.3039	1.0000	0.7004	0.4007	0.2996	1.0636	0.7004
	N206-4	0.2290	1.2872	1.0000	0.6920	0.3840	0.3080	1.0581	0.6920
	N206-5	0.2964	1.2706	1.0000	0.7379	0.4759	0.2621	0.9741	0.7379
	N206-6	0.2363	1.2676	1.0000	0.6984	0.3969	0.3016	1.0313	0.6984
	N206-8	0.2198	1.2816	1.0000	0.6836	0.3672	0.3164	1.0618	0.6836
	N206-9	0.2073	1.2946	1.0000	0.6740	0.3481	0.3260	1.0873	0.6740
	N206-10	0.2008	1.3070	1.0000	0.6677	0.3354	0.3323	1.1062	0.6677
	N206-11	0.2108	1.2891	1.0000	0.6754	0.3507	0.3246	1.0782	0.6754
Average	/	0.2459	1.2761	1.0000	0.7001	0.4002	0.2999	1.0302	0.7001

In Figure 17, the D_q curves of all samples exhibit distinct multifractal trends, characterized by monotonic decreases in D(q) with increasing q and a clear separation between positive and negative q regions. This behavior confirms the multifractal nature of the mesopore-to-macropore pore size distribution.

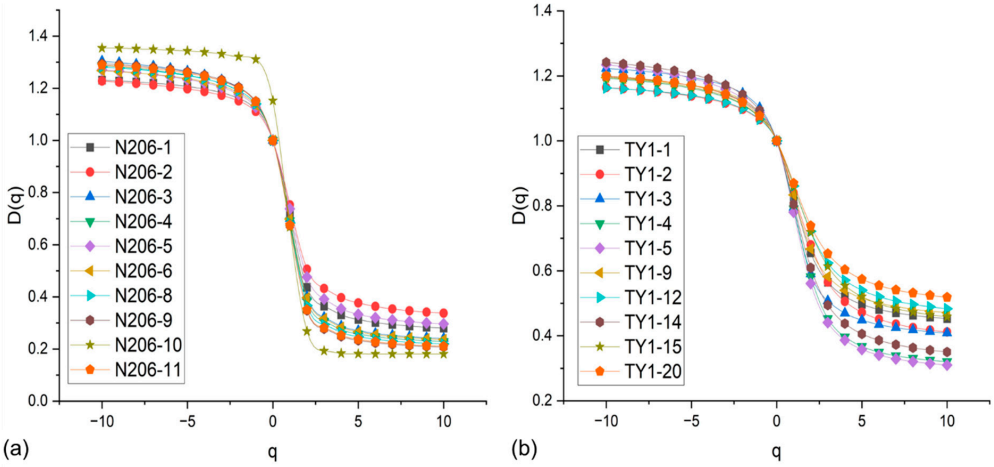

Figure 17. Relationship between D_q and q from low-pressure N_2 adsorption data for (**a**) N206 and (**b**) TY1.

Longmaxi samples show higher average D_1 and D_2 values than Qiongzhusi samples, suggesting a more evenly distributed and better-connected mesopore network in the former. These differences are further quantified by the $D_0 - D_1$ indicator, which is higher for Qiongzhusi shales (average 0.2999) than for Longmaxi (average 0.1737), indicating greater heterogeneity and clustering of mesopore PSDs in the Qiongzhusi Formation.

The range of generalized dimensions, measured by $D_{10-} - D_{10+}$, is also broader in Qiongzhusi shales (average 1.0302) compared to the Longmaxi shales (0.7823), reinforcing the interpretation of more structurally heterogeneous mesopores in the former. The derived Hurst exponent ($H = (D_2 + 1)/2$) is consistently higher in Longmaxi samples (0.8263) than in the Qiongzhusi samples (0.7001), indicating a higher degree of positive autocorrelation and potentially improved pore connectivity in Longmaxi shales.

Complementary insights are provided by multifractal singularity spectra $f(\alpha)$, plotted against singularity strength α in Figure 18, with the associated parameters listed in Table 6. The characteristic convex parabolic curves in both formations confirm the multifractal behavior. However, the Qiongzhusi samples exhibit broader singularity spectra, with higher values of α_0, α_{10-}, and α_{10+}, indicating a wider distribution of scaling exponents and greater PSD complexity.

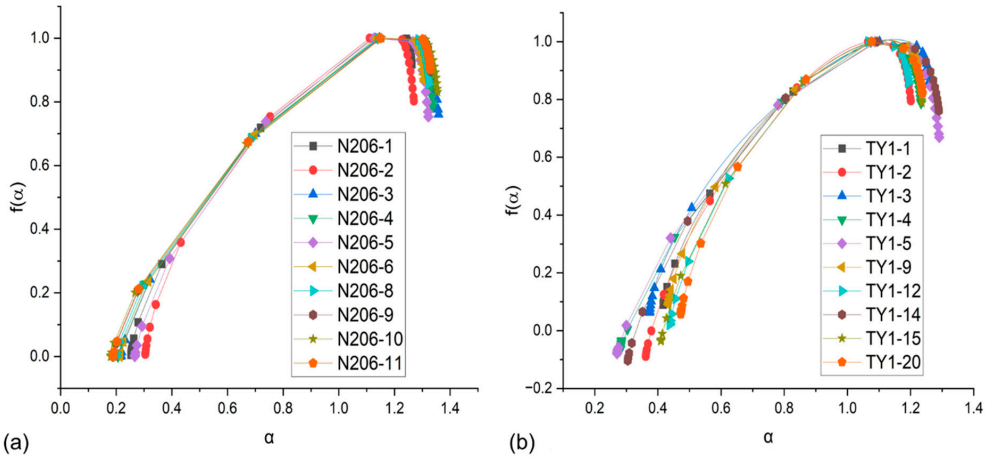

Figure 18. Multifractal singularity from low-pressure N_2 adsorption data for (**a**) N206 and (**b**) TY1.

Table 6. Mesopore–macropore multifractal singularity characteristics from low-pressure N_2 adsorption data.

Formation	Sample	α_{10+}	α_{10-}	α_0	$\alpha_{10-} - \alpha_{10+}$	$\alpha_0 - \alpha_{10+}$	$\alpha_{10-} - \alpha_0$	R_d
Longmaxi	TY1-1	0.4166	1.2356	1.0828	0.8190	0.6662	0.1528	0.5134
	TY1-2	0.3615	1.2012	1.0652	0.8397	0.7037	0.1360	0.5677
	TY1-3	0.3738	1.2601	1.1019	0.8863	0.7281	0.1582	0.5699
	TY1-4	0.2850	1.2335	1.0737	0.9485	0.7887	0.1597	0.6290
	TY1-5	0.2725	1.2911	1.0876	1.0186	0.8151	0.2035	0.6116
	TY1-9	0.4332	1.2251	1.0860	0.7918	0.6528	0.1390	0.5137
	TY1-12	0.4372	1.1938	1.0661	0.7566	0.6289	0.1276	0.5013
	TY1-14	0.3047	1.2899	1.0946	0.9851	0.7899	0.1953	0.5946
	TY1-15	0.4097	1.2362	1.0733	0.8264	0.6636	0.1629	0.5007
	TY1-20	0.4725	1.2376	1.0770	0.7651	0.6046	0.1606	0.4440
Average	/	0.3767	1.2404	1.0808	0.8637	0.7042	0.1596	0.5446
Qiongzhusi	N206-1	0.2527	1.2627	1.1203	1.0100	0.8676	0.1424	0.7252
	N206-2	0.3045	1.2701	1.1113	0.9656	0.8068	0.1587	0.6481
	N206-3	0.2163	1.3583	1.1462	1.1419	0.9298	0.2121	0.7177
	N206-4	0.2061	1.3374	1.1399	1.1313	0.9338	0.1975	0.7363
	N206-5	0.2668	1.3223	1.1276	1.0555	0.8608	0.1947	0.6661
	N206-6	0.2127	1.3079	1.1347	1.0952	0.9220	0.1732	0.7487
	N206-8	0.1979	1.3240	1.1408	1.1262	0.9429	0.1832	0.7597
	N206-9	0.1865	1.3346	1.1504	1.1481	0.9639	0.1842	0.7797
	N206-10	0.1807	1.3545	1.1529	1.1738	0.9722	0.2016	0.7706
	N206-11	0.1897	1.3278	1.1485	1.1381	0.9587	0.1794	0.7793
Average	/	0.2214	1.3200	1.1373	1.0986	0.9159	0.1827	0.7331

The mean Rd value of the Qiongzhusi samples (0.7331) surpasses that of the Longmaxi samples (0.5446), signifying more asymmetry and heterogeneity in the particle size distributions of Qiongzhusi shales. Conversely, Longmaxi shales demonstrate a more constrained α spectrum and reduced Rd, indicating a more homogeneous and symmetrical distribution of mesopore and macropore structures.

The multifractal analysis of N_2 adsorption data indicates that Qiongzhusi shales exhibit significant heterogeneity and asymmetrical distribution of meso-to-macropores, likely affected by advanced diagenetic compaction and mineralogical maturity. In contrast, Longmaxi shales have relatively homogeneous pore structures and improved connectivity over wider pore size ranges.

3.5. Fractal Properties of Reconstructed Shale Pore Structures

We produced a series of reconstructed 3D pore models from 2D SEM images (Figure 19) to assess the applicability of the newly established 3D succolarity approach and pore architecture models (PAMs) in shale systems. The chosen photos depict characteristic pore textures in Qiongzhusi (N206-2, N206-5, and N206-7) and Longmaxi (TY1-2, TY1-4, and TY1-6) shales, encompassing a broad spectrum of porosities and microstructural varieties. Binary segmentation was applied to extract pore regions, followed by a voxel-based MCMC scanning algorithm to generate 3D PAMs.

Fractal characteristics were quantified for the reconstructed volumes. Table 7 summarizes the fractal dimension (FD) and lacunarity (LA), while the complete succolarity dataset is presented separately in Table A5, Appendix A. On average, Longmaxi samples exhibit higher FD (2.6518) and lower LA (0.1639) than Qiongzhusi samples (FD = 2.4471; LA = 0.2751). Under the SEM scale, this reflects that Longmaxi shales possess more hierarchical and spatially more homogeneous pore networks. Yet, pore systems are more fragmented and heterogeneous in Qiongzhusi shales.

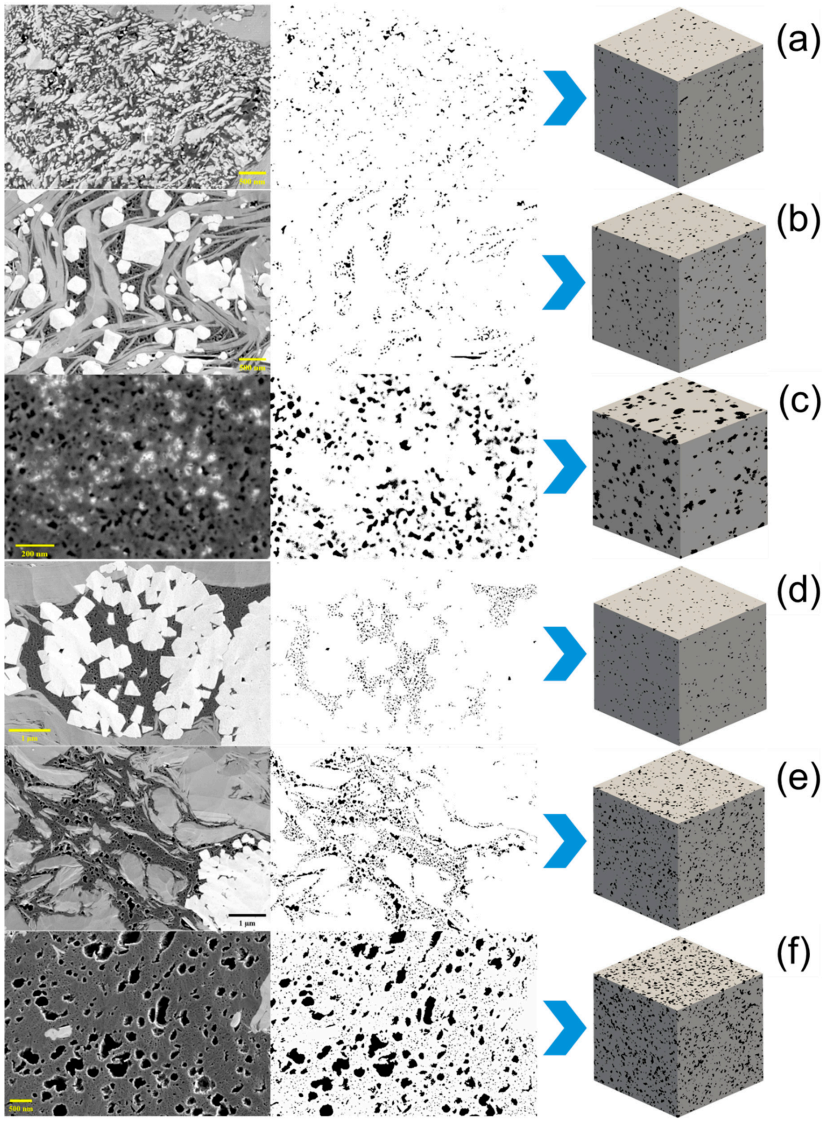

Figure 19. Shale pore reconstruction with the corresponding SEM images, for samples (**a**) N206-5 (φ = 2.24%), (**b**) N206-2 (φ = 2.48%), (**c**) N206-2 (φ = 11.78%), (**d**) TY1-4 (φ = 2.24%), (**e**) TY1-6 (φ = 7.39%), (**f**) TY1-2 (φ = 16.59%).

Table 7. Fractal dimension, lacunarity, and porosity comparison of reconstructed shale pore models.

Formation	Sample	Image Porosity (φ%)	Volume Porosity (φ%)	Fractal Dimension	Lacunarity
Longmaxi	TY1-2	7.19	7.19	2.7049	0.1190
		6.37	6.37	2.6333	0.1832
		16.59	16.59	2.8418	0.0970
	TY1-4	2.24	2.24	2.4191	0.2562
		2.64	2.64	2.4294	0.2864
		3.26	3.26	2.5042	0.2187
		13.51	13.51	2.7854	0.1302
		11.61	11.61	2.7927	0.0949

Table 7. *Cont.*

Formation	Sample	Image Porosity (φ%)	Volume Porosity (φ%)	Fractal Dimension	Lacunarity
Longmaxi	TY1-6	4.71	4.71	2.5935	0.1725
		6.66	6.66	2.6597	0.1549
		7.39	7.39	2.6768	0.1556
		10.88	10.88	2.7804	0.0976
	Average	7.75	7.75	2.6518	0.1639
Qiongzhusi	N206-2	11.78	11.78	2.7115	0.2536
		2.57	2.57	2.4354	0.2697
		2.65	2.65	2.4463	0.2545
		3.31	3.31	2.4935	0.2379
		2.48	2.48	2.4215	0.2828
	N206-5	1.98	1.98	2.3792	0.2988
		1.3	1.3	2.3013	0.3012
		2.24	2.24	2.4069	0.2779
	N206-7	4.59	4.59	2.5610	0.2232
		1.58	1.58	2.3141	0.3513
	Average	3.45	3.45	2.4471	0.2751

Directional succolarity results are displayed in Figure 20 as radar plots on a logarithmic scale, which allows directional contrasts to be compared across several orders of magnitude. At the scale of SEM reconstructions, the Longmaxi group overall shows larger succolarity values and, thus, better pore connectivity than the Qiongzhusi group. Moreover, the polygons of Longmaxi tend to be more isotropic, indicating more balanced connectivity across directions, while Qiongzhusi samples exhibit comparatively lower succolarity and often more uneven directional patterns. Within each formation, however, both isotropic and anisotropic cases occur: For example, TY1-2 shows relatively isotropic connectivity across all axes, whereas TY1-4 reveals stronger contrasts between horizontal and vertical directions (Figure 20b). Similar intra-group variation is also observed in the Qiongzhusi set (Figure 20c).

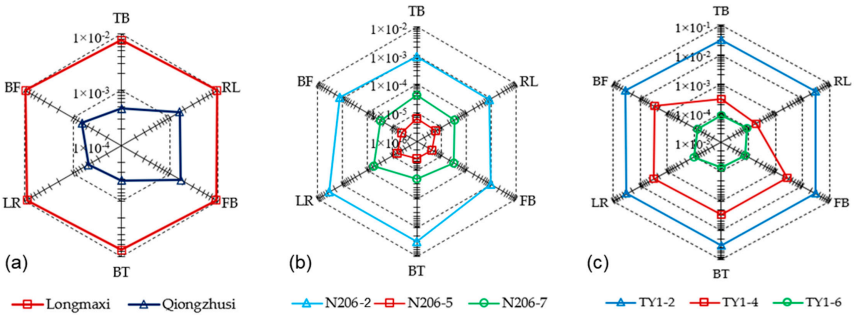

Figure 20. Average succolarity values organized directionally top-to-bottom (TB), bottom-to-top (BT), right-to-left (RL), left-to-right (LR), front-to-back (FB), and back-to-front (BF), comparing (**a**) the Longmaxi and Qiongzhusi formations, (**b**) the three representative samples collected from the Longmanxi formation, and (**c**) the three representative samples collected from the Qiongzhusi formation. The plots highlight the significant contrast in succolarity between the Longmaxi and Qiongzhusi shales and show the anisotropy in the sample microstructure. The numerical data are also presented in Table A3.

Compared with FD and LA, which mainly quantify geometrical irregularity and spatial dispersion, succolarity uniquely captures the capacity of percolation and continuity of fluid-conducting pathways through the pore network. This metric, thus, provides complementary and previously inaccessible information on shale pore topology, especially regarding anisotropic connectivity and fluid migration potential.

In this section, the applicability of pore architecture models (PAMs) to shale systems is also demonstrated. First, as shown in Figure 19, the reconstructed 3D pore architectures closely resemble their corresponding 2D SEM images in terms of pore morphology and spatial arrangement, indicating that PAMs can realistically capture characteristic shale textures. Second, in Table 7, we report both the image porosity and volume porosity of the reconstructed PAMs. By adjusting model parameters, the generated 3D structures reproduce the porosity of the input images with close agreement, confirming that PAMs can preserve quantitative porosity characteristics in addition to visual similarity. Finally, all fractal parameters, including FD, LA, and succolarity, are derived from the PAMs, thereby reflecting different aspects of the shale pore network based on these reconstructed volumes. This consistency further supports the suitability of PAMs as a robust framework for quantifying pore complexity, uniformity, and connectivity in shale matrices.

3.6. Estimation of CO_2 Storage Capacity

Shale formations can store CO_2 via adsorption in nano-pores and free gas in connected pores; quantifying both under in situ P–T is essential to assess storage potential and to compare intervals with different textures and organic content. Prior studies show shales possess significant CO_2 sorption capacities and that pore size (micro/meso) governs the partitioning between adsorbed and free phases [128,129].

Under in situ P–T, the volumetric CO_2 storage capacity (G_{total}) of shale is taken as the sum of (i) **adsorbed gas** (G_{ads}) described by a Langmuir isotherm, (ii) **mesopore film adsorption** ($G_{ads,film}$) accounting for multilayer coverage in the 2–50 nm range, and (iii) **free gas** G_{free} occupying the effective pore volume (water-filled part excluded). This partition follows IUPAC pore-size conventions (micro <2 nm; meso 2–50 nm).

$$G_{total} = G_{ads} + G_{ads,film} + G_{free} \tag{12}$$

with G in kgm^{-3}.

A single-site Langmuir isotherm is used for CO_2 uptake at reservoir pressure P, with the affinity term temperature-corrected by a van't Hoff relation [130]:

$$n_{abs}(P,T) = \frac{L_{max} b(T) P}{1 + b(T) P} \tag{13}$$

where

$$b(T) = b_{273} exp\left[-\frac{\Delta H}{R}\left(\frac{1}{T + 273.15} - \frac{1}{273.15}\right)\right] \tag{14}$$

with L_{max} the Langmuir capacity, b_{273} the affinity at 273 K, and ΔH the isosteric heat (negative for exothermic physisorption) [130,131]. The adsorbed-phase mass per rock volume is

$$G_{ads} = \rho_b \times (1000) \times n_{abs}(P,T) \times (0.044) \tag{15}$$

with bulk density ρ_b in gcm^{-3}, $n_{abs}(P,T)$ in $mmolg^{-1}$, and molar factor 0.044 for CO_2 [130,131].

To avoid over-assigning mesopore volume to the free-gas phase, we deduct the geometric film volume associated with multilayer adsorption in mesopores:

$$G_{ads,film} = \phi_{meso,layer} \times \rho_{ads} \quad (16)$$

where

$$\phi_{meso,layer} = \rho_b A_{2-50} t \quad (17)$$

Here, A_{2-50} is the N_2-DFT surface area restricted to 2–50 nm pores, t is the adopted film thickness (we use t = 0.35 nm), and ρ_{ads} is an effective adsorbed-phase density (we use 0.9 g cm^{-3}) [129].

Free-phase storage uses the effective pore fraction after removing (i) micropores counted as adsorption space and (ii) the mesopore film volume:

$$G_{free} = \phi_{eff} (1 - S_w) \rho_g \quad (18)$$

with water saturation $S_w = 0.45$ [132,133] and CO_2 density $\rho_g(P, T)$ obtained from the Span–Wagner reference EOS at the sample's in situ $P - T$ [134].

Using the workflow defined above, we obtained sample-scale CO_2 capacities for the two wells. Figure 21 shows a clear contrast between them: TY1 samples are adsorption-dominated, with only a small free-gas contribution atop a substantial adsorption fraction, whereas N206 exhibits a more balanced split with a visibly larger free-gas contribution.

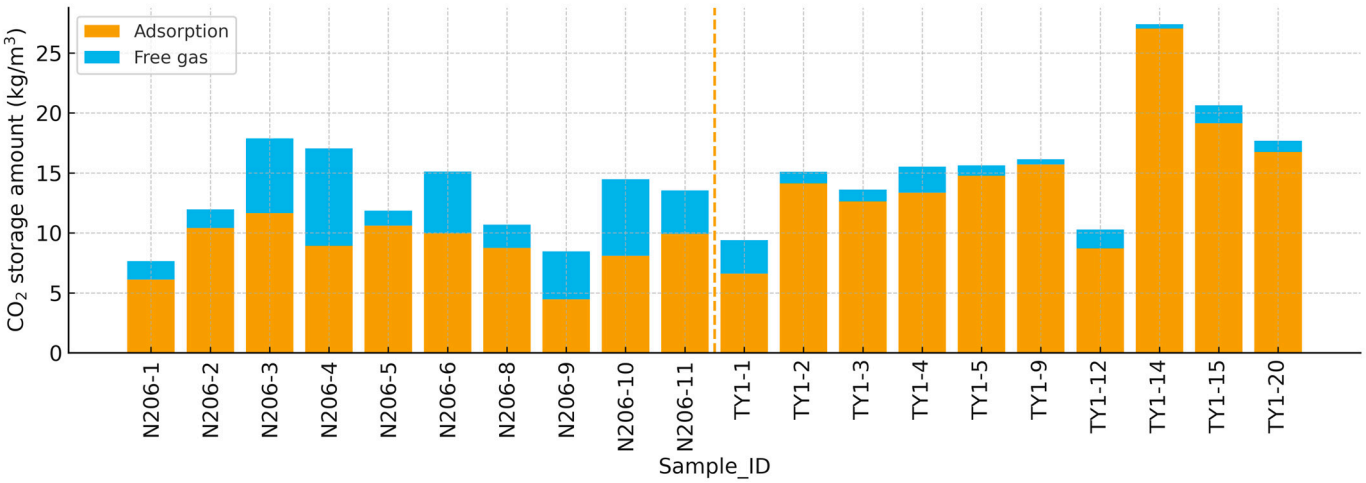

Figure 21. Comparison of CO_2 storage amount per sample for N206 and TY1: adsorption and free gas.

This visual impression is borne out by the distribution statistics in Figure 22. For N206, the median adsorption capacity is 9.42 kg m^{-3} (range 4.47–11.65 kg m^{-3}) and the median free-gas capacity is 3.82 kg m^{-3} (1.26–8.13 kg m^{-3}), yielding a median total of 12.77 kg m^{-3} (7.65–17.89 kg m^{-3}) with adsorption accounting for roughly 70% of the total on a general level. Meanwhile, TY1 presents a different situation: Adsorption rises to a median of 14.46 kg m^{-3} (6.60–27.04 kg m^{-3}), free gas is much smaller with a median of 0.97 kg m^{-3} (0.36–2.80 kg m^{-3}), and the median total reaches 15.58 kg m^{-3} (9.40–27.40 kg m^{-3}), with adsorption contributing about 93% of the total.

In summary, both wells store CO_2 primarily by adsorption, but TY1 achieves higher totals through stronger adsorption capacity, whereas N206 retains a larger free-gas share.

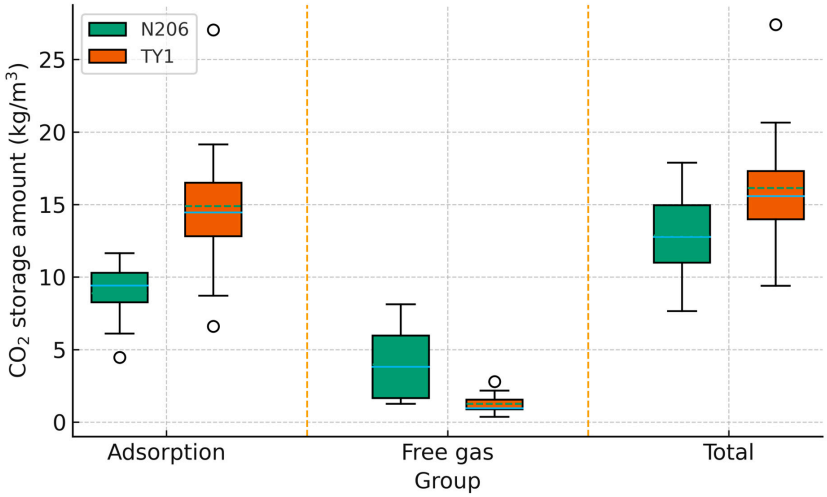

Figure 22. Comparison of adsorption, free-gas, and total CO_2 storage distributions for N206 and TY1.

3.7. CO_2 Breakthrough Pressure and MICP-RGPZ Permeability

For low-permeability shales, the capillary entry (breakthrough) pressure is the first barrier that injected CO_2 must overcome to invade connected pore throats; it, therefore, sets a primary control on injectivity and, conversely, on sealing capacity [135,136]. Several studies have derived CO_2–brine capillary pressures directly or by converting mercury-intrusion curves to appraise the ease of CO_2 invasion and migration in caprocks and fine-grained reservoirs [137–139]. Following the established practice [140], we convert the capillary pressure $P_c^{Hg\text{-}air}$ for the Hg-air system to $P_c^{CO_2\text{-}brine}$ as follows:

$$P_c^{CO_2\text{-}brine} = \alpha P_c^{Hg\text{-}air}, \alpha = 0.08 \quad (19)$$

where α is a constant conversion factor to reflect typical CO_2–brine vs. Hg–air interfacial properties at reservoir conditions [140].

The measured and calculated pressure results are listed in Table 8. For N206, entry pressures on the Hg–air curves are low and tightly grouped: mean P_{10} = 0.226 MPa (range 0.187–0.284 MPa) and mean P_{20} = 0.360 MPa (0.239–0.547 MPa). The corresponding median metrics indicate a coarse pore–throat system ($P_{50} \approx 0.940$ MPa; D_{50} on the order of 1–3 µm). After conversion to CO_2–brine, the thresholds remain small: mean P_{10} CO_2 = 0.018 MPa and mean P_{20} CO_2 = 0.029 MPa.

Table 8. Pore structure parameters along with measured and calculated pressure (P_{10}, P_{10} CO_2, P_{20}, P_{20} CO_2, and P_{50}) from the MICP test of the shale samples in this paper.

Formation	Sample	Porosity (%)	P_{10} (MPa)	P_{20} (MPa)	P_{50} (MPa)	D_{50} (nm)	P_{10} CO_2 (MPa)	P_{20} CO_2 (MPa)
Longmaxi	TY1-1	0.6530	2.4975	13.398	118.106	12.4710	0.1998	1.0719
	TY1-2	0.6403	2.6432	49.916	57.999	25.4478	0.2115	3.9933
	TY1-3	1.1000	2.1610	19.647	115.376	12.7554	0.1729	1.5718
	TY1-4	0.6750	6.9298	30.771	101.343	14.5348	0.5544	2.4617
	TY1-5	0.9248	3.2693	15.877	93.146	15.8134	0.2615	1.2702
	TY1-9	0.9190	2.2158	43.01	89.636	16.4259	0.1773	3.4408
	TY1-12	0.7645	36.3973	40.041	67.95	23.3977	2.9118	3.2032
	TY1-14	1.8240	3.4600	26.579	121.593	12.0952	0.2768	2.1263
	TY1-15	0.9911	1.9760	49.824	96.435	15.2562	0.1581	3.9859
	TY1-20	1.6119	10.005	42.205	149.775	9.8281	0.8004	3.3764

Table 8. *Cont.*

Formation	Sample	Porosity (%)	P_{10} (MPa)	P_{20} (MPa)	P_{50} (MPa)	D_{50} (nm)	P_{10} CO_2 (MPa)	P_{20} CO_2 (MPa)
Average	/	1.0104	7.1555	33.127	101.136	15.8026	0.5725	2.6502
Qiongzhusi	N206-1	0.7207	0.2837	0.5469	1.3597	1084.47	0.0227	0.0437
	N206-2	0.8750	0.2292	0.3821	1.1926	1239.86	0.0183	0.0306
	N206-3	2.5168	0.2014	0.2747	0.6588	2235.43	0.0161	0.0220
	N206-4	3.1863	0.1983	0.2694	0.6578	2238.88	0.0159	0.0215
	N206-5	0.7522	0.2715	0.5250	1.4041	1048.94	0.0217	0.0420
	N206-6	2.1046	0.2080	0.2872	0.6894	2136.17	0.0166	0.0230
	N206-8	0.8983	0.2419	0.4346	1.3414	1097.25	0.0194	0.0348
	N206-9	1.5371	0.1817	0.2389	0.5170	2849.71	0.0145	0.0191
	N206-10	2.4311	0.1948	0.2564	0.5881	2503.58	0.0156	0.0205
	N206-11	1.4642	0.2501	0.3809	0.9947	1481.04	0.0200	0.0305
Average	/	1.6486	0.2261	0.3596	0.9404	1791.53	0.0181	0.0288

Note: P_{10} and P20 are pressures from the Hg–air MICP curves at 10% and 20% cumulative intrusion; P_{50} is the median capillary pressure; D50 is the median throat diameter; P_{10} CO_2 and P_{20} CO_2 are for CO_2–brine system.

In contrast, TY1 exhibits much higher and more dispersed entry pressures on the Hg–air curves: mean P_{10} = 7.156 MPa (1.976–36.397 MPa) and mean P_{20} = 33.127 MPa (13.398–49.916 MPa). Its typical capillary level and throat size are consistent with a much finer network ($P_{50} \approx$ 101.136 MPa; D_{50} in the tens-of-nanometers range, ~10–25 nm). Converted to CO_2–brine, the corresponding thresholds are mean P_{10} CO_2 = 0.573 MPa and mean P_{20} CO_2 = 2.650 MPa.

Accurately predicting permeability (k) is paramount for assessing the injectivity potential of shale reservoirs targeted for CO_2 storage [141–143]. Unlike conventional formations, shales possess complex, nanoporous networks where permeability cannot be reliably estimated from porosity alone and is notoriously challenging to measure experimentally under representative in situ conditions [144–146].

We estimate permeability from the MICP data using the Revil–Glover–Pezard–Zamora (RGPZ) formulation, which expresses K_{RGPZ} as a function of porosity ϕ, a grain-scale length d_{grain} derived from the pore–throat size $d_{pore\ throat}$, and the electrical cementation exponent m (we adopt m = 3 and $a \approx 8/3$ following the previous practice [147–149]):

$$K_{RGPZ} = \frac{d_{grain}^2\, \phi^{3m}}{4am^2} \tag{20}$$

where d_{grain} is the grain diameter controlling the flow characteristics within the porous media and is estimated via

$$d_{grain} = 1.6585 \sqrt[2]{\frac{am^2}{8\phi^{2m}}} d_{pore\ \mathrm{throat}} \tag{21}$$

where $d_{pore\ throat}$ is the mode pore diameter measured from MICP.

This approach has been validated against core data and other predictive models and does not require empirical calibration for each rock set. The estimated permeabilities for the shale samples are presented in Table 9.

Table 9. Summary of the permeabilities of shale samples in this paper calculated from MICP and RGPZ model.

Formation	Sample	$d_{pore\ throat}$ (um)	k_{RGPZ} (nD)
Longmaxi	TY1-1	0.0126	3.86×10^{-3}
	TY1-2	0.0262	1.57×10^{-2}
	TY1-3	0.0076	6.75×10^{-3}
	TY1-4	0.0077	1.61×10^{-3}
	TY1-5	0.0076	3.98×10^{-3}
	TY1-9	0.0159	1.70×10^{-2}
	TY1-12	0.0351	4.80×10^{-2}
	TY1-14	0.0071	2.67×10^{-2}
	TY1-15	0.0072	4.35×10^{-3}
	TY1-20	0.0078	2.22×10^{-2}
Average	/	0.0135	1.50×10^{-2}
Qiongzhusi	N206-1	0.6547	1.40×10^{1}
	N206-2	0.6547	2.50×10^{1}
	N206-3	0.6319	5.54×10^{2}
	N206-4	0.6319	1.13×10^{3}
	N206-5	0.5921	1.30×10^{1}
	N206-6	2.8010	6.37×10^{3}
	N206-8	0.5864	2.17×10^{1}
	N206-9	3.9190	4.86×10^{3}
	N206-10	5.1500	3.32×10^{4}
	N206-11	0.5981	9.78×10^{1}
Average	/	1.6220	4.63×10^{3}

The permeabilities of the two wells are separated by several orders of magnitude. TY1 exhibits very small characteristic pore–throat diameters (0.0071–0.0351 μm; mean 0.0135 μm) and correspondingly tiny RGPZ permeabilities, from 1.61×10^{-3} to 4.80×10^{-2} nD with a mean of 1.50×10^{-2} nD. By contrast, N206 shows micrometer-scale throats (0.5864–5.1500 μm; mean 1.622 μm) and k_{RGPZ} from 1.30×10^{1} to 3.32×10^{4} nD with a mean of 4.63×10^{3} nD. On average, the cross-well contrast approaches six orders of magnitude, and the most permeable N206 sample exceeds the least permeable TY1 sample by more than seven orders. These permeability results are internally consistent with the breakthrough analysis: The well that requires lower CO_2 entry pressures (N206) also offers much greater flow capacity once invaded, whereas the well with nanometer-scale throats (TY1) remains effectively nonconductive.

4. Discussion

4.1. Geological and Pore Structural Implications on CO_2 Storage Potential

The evolution and characteristics of the shale pore system are fundamentally governed by organic geochemistry, mineralogical composition, and diagenetic processes [150]. They exert strong influences on pore development, morphology, and, eventually, gas transport and storage capacity [151]. The Qiongzhusi (N206) and Longmaxi (TY1) shales examined in this study present contrasting yet complementary insights into the geological controls shaping shale pore structures and their implications for CO_2 storage potential.

The Qiongzhusi shales, characterized by a greater burial depth (1846.53–1888.26 m) and higher thermal maturity (Ro = 4.07%), exhibit extensive diagenetic mineral transformations, particularly the conversion of unstable minerals such as K-feldspar, kaolinite, and smectite to authigenic illite, chlorite, and quartz [121,122]. This mineralogical evolution is evident in the SEM observation and the higher quartz content (46.21 wt%) and clay mineral abundance (32.19 wt%), with illite (60.2%) and chlorite (24.2%) in their clay composition. Such mineral transformations, driven by higher maturity and prolonged diagenesis, result

in a rigid framework predominantly hosting micropores, which are constrained by extensive mineral infill and compaction. Moreover, the higher pyrite content (5.38 wt%) and occasional occurrence of authigenic anatase in Qiongzhusi samples further indicate some hydrothermal alteration, reducing overall pore volume and connectivity by occupying previously available organic-hosted pores.

In contrast, the Longmaxi shales, with shallower burial and moderate maturity (Ro = 2.16%), exhibit less intense diagenetic alteration. They retain higher TOC (4.40 wt%) and more primary minerals, including K-feldspar and kaolinite, due to their intermediate diagenesis. The preservation of these primary minerals indicates less mineral conversion, allowing more extensive organic-hosted mesopores to form during hydrocarbon generation. SEM observations and adsorption data confirm that the Longmaxi shales have a higher meso–macro pore volume (0.0187 cc/g) and greater BET surface areas (17.635 m^2/g) than the Qiongzhusi shales (4.143 m^2/g), indicating more favorable conditions for meso–macro pore development. These well-developed organic-hosted pores result primarily from moderate thermal maturity, abundant TOC, limited mineral infilling, and reduced compaction effects.

Studies show that carbonate-rich shales exhibit susceptibility to meso- and microporosity alterations due to interactions with CO_2 and water [152], which enhances the available pore space for CO_2 storage [153]. This indicates a greater appropriateness of the carbonate-rich Longmaxi samples compared to the Qiongzhusi samples for CO_2 storage.

Quartz grains, due to their mechanical rigidity and chemical stability, likely protect associated OM from compaction, thus preserving abundant interconnected nanopores generated during thermal maturation. In both samples, authigenic quartz precipitation appears beneficial for OM porosity preservation. However, in contrast, the clay-dominated matrices (primarily illite and mixed-layer illite/smectite), being more ductile and prone to compaction, offer less effective mechanical support to the pore space within OM. This leads to smaller and less interconnected nanopores.

Therefore, the distinct mineralogical and diagenetic differences between these formations lead directly to divergent pore structures. The Qiongzhusi Formation, dominated by micropores due to extensive mineral transformation and hydrothermal alteration, might constrain its overall storage performance. The Longmaxi TY1 shale, characterized by higher TOC, moderate maturity, and preserved mesoporosity, presents greater storage capacity. Yet, it suffers from severe injectivity limitations due to nanometer-scale throats and ultra-low permeabilities. This trade-off is elaborated in Section 4.3.

4.2. Multifractal Analysis and 3D Reconstruction of Pore Structures: Implications for CO_2 Storage

Multifractal analysis of adsorption isotherms offers insights into pore heterogeneity and connectivity across micro and macro pore scales. Generalized dimension spectra and multifractal singularity characteristics distinguish the pore structural complexity of Qiongzhusi and Longmaxi shales.

Low-pressure CO_2 adsorption data indicate that the Qiongzhusi shales have marginally greater micropore volumes and demonstrate elevated Hurst exponent (H) values, suggesting improved micropore connectivity and storage capacity. Longmaxi shales exhibit higher $D_0 - D_1$ values (0.0622) compared to Qiongzhusi shales (0.0490), indicating increased heterogeneity and clustering in micropore distributions. The Qiongzhusi Formation exhibits effective nanopore connectivity; however, the limited pore sizes may constrain the overall capacity for CO_2 storage.

Nitrogen adsorption-derived multifractal parameters highlight variations from mesoporous to macroporous structures. Longmaxi shales exhibit broader singularity spectra, characterized by elevated $\alpha_{10-} - \alpha_{10+}$ and Rd values, which suggest a greater diversity

and abundance of larger pores that enhance CO_2 transport and storage. Surface area measurements from CO_2 adsorption, N_2 adsorption, and MICP consistently indicate higher BET surface areas in Longmaxi samples, implying greater accessible pore space. The narrower fractal spectra of Qiongzhusi shales highlight their predominance of micropores, which restricts CO_2 diffusion and retention at larger (meso-/macro-) scales. The utilization of 3D techniques to reconstruct pore networks from 2D SEM images enhances multifractal analyses through direct visualization and quantification of pore geometry.

The computation of reconstructed 3D models demonstrates significant variations in fractal dimensions, lacunarity, and the newly defined parameter of succolarity. Succolarity quantifies directional pore connectivity and percolation capacity, providing a notable advantage over traditional fractal parameters by directly evaluating gas migration pathways within the pore network. Higher succolarity values across various orientations in Longmaxi samples are strongly associated with increased mesoporosity and larger pore sizes, thereby confirming succolarity as a reliable indicator of favorable pore connectivity and potential storage efficiency at the SEM-image scale. The lower succolarity and higher lacunarity in Qiongzhusi samples indicate compartmentalized microporous domains, which may reduce volumetric storage efficiency at this scale.

Nonetheless, the reconstruction of 3D pore networks from 2D SEM images presents specific limitations. This reconstruction may underestimate or overestimate pore connectivity when derived from restricted 2D observations. The following calculation and modeling of these 3D pore networks still need to be upscaled and tested for larger scales. And importantly, succolarity and multifractal indices are scale-dependent and complementary to bulk pore structure metrics. Therefore, upscaling and cross-validation with bulk methods (MICP, permeability) remain necessary to ensure representativeness.

Still, combining multifractal analysis with 3D reconstruction yields robust and complementary data sets, enhancing the accuracy of pore network characterization relative to traditional single-method approaches. The integration of multifractal analysis with advanced 3D reconstruction techniques, such as directional succolarity measurement, provides detailed insights into shale pore structures, thereby enhancing the understanding of their CO_2 storage potentials.

4.3. Evaluating CO_2 Storage Potential and Injectivity Constraints in Longmaxi–TY1 and Qiongzhusi–N206 Shales

The comparison between the Longmaxi–TY1 and Qiongzhusi–N206 shales highlights a fundamental trade-off between storage capacity and injectivity, which ultimately constrains their CO_2 sequestration potential.

In terms of storage, TY1 achieves higher total CO_2 capacities (median $\approx$ 15.6 kg m^{-3}) largely through adsorption, where adsorption alone contributes ~93% of the total. By contrast, N206 shows a lower but more balanced storage partitioning (median $\approx$ 12.8 kg m^{-3}, with adsorption ~70% and free gas ~30%). This suggests that TY1 offers greater security in retaining CO_2 due to its adsorption-dominated uptake and sealing microstructure, whereas N206 provides higher operational injectivity and faster pore filling but is more vulnerable to leakage risks.

TY1 samples are dominated by nanometer-scale throats ($D_{50} \approx$ 10–25 nm) and exhibit extremely high breakthrough pressures (P_{10} $CO_2 \approx$ 0.57 MPa; P_{20} $CO_2 \approx$ 2.65 MPa), coupled with ultra-low permeabilities (K_{RGPZ} on the order of 10^{-2} nD). This pore structure configuration ensures exceptional sealing integrity once CO_2 is emplaced, but simultaneously imposes severe injectivity limitations, as fluids face high capillary entry barriers and negligible flow pathways. On the other hand, N206 samples possess micrometer-scale throats ($D_{50} \approx$ 1–3 μm) and very low breakthrough pressures (P_{10} $CO_2 \approx$ 0.018 MPa; P_{20} $CO_2 \approx$ 0.029 MPa), with permeabilities that are 5–6 orders of magnitude higher than those

of TY1. Such characteristics favor rapid CO_2 injectivity and migration, but at the expense of long-term sealing capacity.

Correlation analysis further clarifies the pore structural controls on CO_2 storage capacity (Figure 23). In both Longmaxi (TY1) and Qiongzhusi (N206) shales, the adsorbed CO_2 storage amount (G_{ads}) shows strong positive correlations with micropore volume/surface area as well as N_2 adsorption-derived mesopore volume/surface area, highlighting the predominant contribution of micro–mesoporous domains to adsorption capacity. This finding is consistent across both formations, reinforcing the critical role of fine-scale pores in governing CO_2 adsorption. In the Qiongzhusi shales, TOC and MICP-derived pore volume are strongly correlated, and both parameters further exhibit strong correlations with free CO_2 and total CO_2 storage capacity, suggesting that organic matter-associated macroporosity provides additional storage space beyond adsorption. Moreover, D_{50} shows an extremely strong negative correlation with CO_2 breakthrough pressures (P_{10} and P_{20}). Given that the Qiongzhusi–N206 samples exhibit much larger average pore–throat diameters ($D_{50} \approx 1791.5$ nm) compared with the Longmaxi–TY1 samples ($D_{50} \approx 15.8$ nm), this relationship indicates that larger pore throats substantially facilitate injectivity, while smaller pore–throat sizes, as in the Longmaxi shales, correspond to higher breakthrough pressures and reduced injectivity.

Taken together, TY1 shales are characterized by larger adsorption-dominated storage capacities but limited injectivity due to nanometer-scale throats and ultra-low permeabilities. In contrast, N206 shales present lower overall storage capacities but better injectivity, supported by micrometer-scale throats and much higher permeabilities. This trade-off suggests a complementary role for the two formations in CO_2 geological storage: Longmaxi may act as a more secure long-term storage interval due to its sealing microstructure, whereas Qiongzhusi offers favorable injection conditions provided effective regional seals are present.

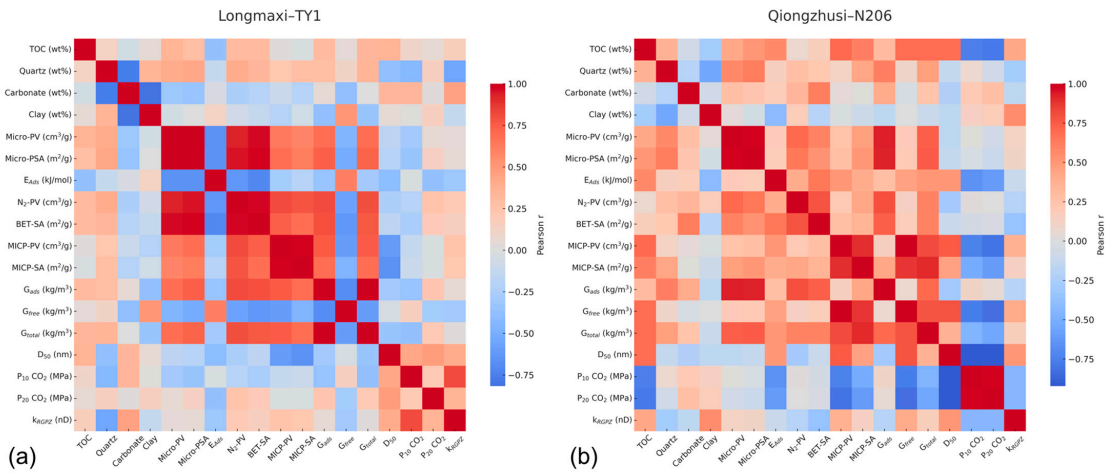

Figure 23. Pearson correlation matrices of geochemical, mineralogical, pore-structure, and CO_2 storage/injectivity parameters for (**a**) Longmaxi–TY1 and (**b**) Qiongzhusi–N206 shales. PV: pore volume, PSA: pore surface area, SA: surface area, E_{ads}: adsorption energy.

5. Conclusions

This study conducted a comprehensive comparative analysis of the CO_2 sequestration potential of two representative shale formations (Longmaxi and Qiongzhusi) using an integrated approach involving organic geochemical characterization, mineralogical analysis, gas adsorption experiments, multifractal analysis, and fractal computations based on 3D pore structure reconstruction. The key conclusions are as follows:

(1) Geological factors, including organic geochemistry, mineral composition, and diagenetic evolution, exert profound controls on micropore heterogeneity and connectivity are observed in both formations. Due to lower maturity, shallower burial, and intermedia diagenesis, mineral assemblages, like clay–quartz–OM, assist Longmaxi shales in preserving abundant organic-hosted mesopores. In contrast, Qiongzhusi's overmaturity and deep-burial environment promote more authigenic mineral generation and high pressure, significantly reducing total accessible pore space.

(2) Multifractal spectra and reconstructed 3D models highlight contrasting pore complexities. Longmaxi exhibits broader singularity spectra and higher succolarity values across orientations, consistent with meso-/macropore development and isotropic connectivity at the SEM scale. Qiongzhusi shows narrower multifractal spectra and lower succolarity, reflecting micropore-dominated, more heterogeneous and anisotropic networks. These metrics complement adsorption and MICP data by quantifying pore connectivity and heterogeneity across scales.

(3) Adsorption and free-gas partitioning indicate that Longmaxi samples achieve higher total CO_2 storage capacities (median $\approx$ 15.6 kg/m^3, with adsorption contributing ~93%) than Qiongzhusi samples (median $\approx$ 12.8 kg/m^3, with adsorption ~70% and free gas ~30%). This confirms that Longmaxi provides larger adsorption-dominated capacities due to better-developed micro–mesoporous networks.

(4) Longmaxi samples exhibit nanometer-scale throats ($D_{50} \approx$ 10–25 nm), very high breakthrough pressures (P_{10} $CO_2 \approx$ 0.57 MPa; P_{20} $CO_2 \approx$ 2.65 MPa), and ultra-low RGPZ permeabilities ($\approx 10^{-2}$ nD). In contrast, Qiongzhusi samples possess micrometer-scale throats ($D_{50} \approx$ 1–3 μm), extremely low breakthrough pressures (P_{10} $CO_2 \approx$ 0.018 MPa; P_{20} $CO_2 \approx$ 0.029 MPa), and permeabilities 5–6 orders of magnitude higher, suggesting much better injectivity.

(5) Longmaxi shales are favorable for long-term CO_2 retention owing to their adsorption-dominated capacities and sealing pore systems, but their injectivity is severely limited. Qiongzhusi shales, while offering smaller total capacities, exhibit superior injectivity and lower entry pressures, making them suitable as injection intervals provided regional seals are present.

Author Contributions: B.L.: conceptualization, methodology, formal analysis, writing—original draft, writing—review and editing, visualization. B.Y.: conceptualization, writing—review and editing, supervision, project administration, funding acquisition. P.W.J.G. and P.L.: methodology, supervision, project administration, funding acquisition. K.W. and C.-T.P.: conceptualization, methodology, software, visualization. W.W. and J.C.: methodology, supervision, writing—review and editing. M.S.: funding acquisition, writing—review and editing. All authors have read and agreed to the published version of the manuscript.

Funding: This study was supported by the National Natural Science Foundation of China (Grants 42272136), China Scholarship Council (Grants 202006400034), and the Doctoral research start-up fund project of Hebei GEO University (Grants BQ2024008).

Data Availability Statement: Digital data processing and visualization were performed using ParaView version 5.13.2 [154,155], available under the Paraview license at https://www.paraview.org/ (accessed on 11 September 2025). Computation results figures were made with Matplotlib version 3.10.0 [156], available under the Matplotlib license at https://matplotlib.org/ (accessed on 11 September 2025) and also with [157], available under the OriginLab license at https://www.originlab.com/. The succolarity code created by the authors was stored on GitHub https://github.com/LBCUGB/3D-Succolarity-Computation, (14 February 2025). The rest of the data presented in this study are available upon request from the corresponding author.

Acknowledgments: We express our gratitude to R. H. C. de Melo (Federal Fluminense University, Brazil), Abderrahim Ayad (Abdelmalek Essaâdi University, Morocco), and Helmut Ahammer (Medical University of Graz, Austria) for their assistance in addressing inquiries related to code development and image processing.

Conflicts of Interest: The authors declare no conflicts of interest.

Appendix A

Table A1. Comprehensive stratigraphic framework in the Changning area, southern Sichuan Basin.

Erathem	System	Series	Formation (Member)	Lithological Unit	Thickness (m)
Paleozoic	Silurian	Wenlockian	Huixingmiao Fm.	Siltstone/Shale	0–150
			Hanjiadian Fm.	Siltstone/Shale	0–50
		Llandovery	Shiniulan Fm.	Limestone/Siltstone/Shale	240–500
			Longmaxi Fm.	Shale	100–680
	Ordovician	Upper	Wufeng Fm.	Shale	3–30
			Linxiang Fm.	Limestone	18–80
		Middle	Baota Fm.	Limestone	10–40
			Datangpo Fm.	Silty shale	100–260
		Lower	Luohanpo Fm.	Sandstone/Limestone	50–160
	Cambrian	Miaolingian	Xiangxi Fm.	Dolostone	220–420
		Series 2	Longwangmiao Fm.	Dolostone	70–200
		Terreneuvian	Canglangpu Fm.	Sandstone/Shale	65–3000
			Qiongzhusi Fm.	Shale	90–400

Table A2. Comprehensive stratigraphic framework in the southern Sichuan Basin.

Erathem	System	Series	Formation (Member)	Lithological Unit	Thickness (m)
Paleozoic	Permian	Lower	Qixia Fm.	Limestone/Dolomite	267.70
	Silurian	Lower	Hanjiadian Fm.	Limestone/Shale	129.95
			Shiniulan Fm.	Limestone/Sandstone/Mudstone	80.85
			Longmaxi Fm.	Mudstone/Shale	182.95
	Ordovician	Upper	Wufeng Fm.	Shale	20.20
			Jiancaogou Fm	Limestone	6.00
		Middle	Baota Fm.	Limestone	28.32

Table A3. Mineralogy, lithofacies types, and organic geochemical results of shale samples from TY1 and N206.

Formation	Sample ID	Depth (m)	Quartz (%)	K-Feldspar (%)	Plagioclase (%)	Carbonate (%)	Pyrite (%)	Clay (%)
Longmaxi	TY1-1	622.6	29.35	4.99	12.05	12.59	0.84	40.17
	TY1-2	647.3	34.43	1.82	6.47	11.57	0.85	44.87
	TY1-3	654.9	35.27	4.89	16.16	11.35	0.71	31.62
	TY1-4	659.8	38.92	1.9	5.47	12.05	2.37	39.29
	TY1-5	663.2	35.94	1.52	5.13	39.19	1.05	16.53
	TY1-9	665.0	18.52	1.1	4.07	59.06	1.3	15.94
	TY1-12	667.3	17.6	0.97	4.22	48.86	0.95	27.4
	TY1-14	670.0	29.54	2.56	9.54	32.66	5.37	20.77
	TY1-15	670.7	52.81	2.11	4.83	14.29	0.75	26.77
	TY1-20	677.5	45.14	2.82	5.92	1.33	1.99	42.81

Table A3. *Cont.*

Formation	Sample ID	Depth (m)	Quartz (%)	K-Feldspar (%)	Plagioclase (%)	Carbonate (%)	Pyrite (%)	Clay (%)
Average	/	/	33.75	2.47	7.39	24.29	1.62	30.62
Qiongzhusi	N206-1	1846.53	40	0	12.2	6.7	2.8	38.3
	N206-2	1851.35	49.1	0	8.7	7	2.9	32.3
	N206-3	1859.64	50.3	0	11.6	7.3	0	30.8
	N206-4	1861.42	46.8	0	9.2	9.9	3.1	31
	N206-5	1862.08	46.6	0	11.2	13.5	0	28.7
	N206-6	1863.32	43.8	0	9.5	9.9	5.4	31.4
	N206-8	1868.59	42	0	9.4	7.2	5.9	35.5
	N206-9	1885.46	41.8	0	0	4.9	19.4	26.4
	N206-10	1886.53	42.8	7.5	0	6.4	4.2	40.4
	N206-11	1888.26	58.9	6.2	0	3.9	10.1	27.1
Average	/	/	46.21	/	7.18	7.67	5.38	32.19

Table A4. Clay mineral composition of shale samples from TY1 and N206.

Formation	Sample ID	Depth (m)	Clay (%)	Illite (%)	Kaolinite (%)	Chlorite (%)	I/S (%)	%S	%I
Longmaxi	TY1-1	622.6	40.17	48	6	10	36	15	85
	TY1-2	647.3	44.87	66	12	11	11	10	90
	TY1-3	654.9	31.62	71	3	11	15	10	90
	TY1-4	659.8	39.29	45	7	11	37	15	85
	TY1-5	663.2	16.53	45	9	16	30	15	85
	TY1-9	665.0	15.94	58	12	18	12	15	85
	TY1-12	667.3	27.4	32	17	28	23	20	80
	TY1-14	670.0	20.77	73	3	14	10	10	90
	TY1-15	670.7	26.77	75	2	15	8	10	90
	TY1-20	677.5	42.81	48	11	14	27	15	85
Average	/	/	30.62	56.1	8.2	14.8	20.9	/	/
Qiongzhusi	N206-1	1846.53	38.3	61	0	39	0	10	90
	N206-2	1851.35	32.3	64	0	23	13	10	90
	N206-3	1859.64	30.8	68	0	29	3	10	90
	N206-4	1861.42	31	43	0	20	37	10	90
	N206-5	1862.08	28.7	71	0	29	0	10	90
	N206-6	1863.32	31.4	40	0	34	26	10	90
	N206-8	1868.59	35.5	81	0	19	0	10	90
	N206-9	1885.46	26.4	73	0	17	10	10	90
	N206-10	1886.53	40.4	68	0	17	15	10	90
	N206-11	1888.26	27.1	33	0	15	52	10	90
Average	/	/	32.19	60.2	0	24.2	15.6	/	/

Table A5. Succolarities of reconstructed shale pore models. Succolarity values presented directionally top-to-bottom (TB), bottom-to-top (BT), right-to-left (RL), left-to-right (LR), front-to-bottom (FB), and bottom-to-front (BF).

Formation	Sample	Image Porosity (φ%)	Su_{TB} ($\times 10^{-5}$)	Su_{BT} ($\times 10^{-5}$)	Su_{LR} ($\times 10^{-5}$)	Su_{RL} ($\times 10^{-5}$)	Su_{FB} ($\times 10^{-5}$)	Su_{BF} ($\times 10^{-5}$)	$Su_{average}$ ($\times 10^{-5}$)
Longmaxi	TY1-2	7.19	5.811	6.253	138.8	134.1	118.8	142.8	91.10
		6.37	11.57	6.832	151.2	189.6	179.9	173.0	118.7
		16.59	9151	8776	9135	9691	9166	9799	9286
	TY1-4	2.24	0.8065	0.5388	31.39	24.17	26.19	27.40	18.42
		2.64	1.210	0.7596	32.97	39.73	40.92	36.03	25.27
		3.26	0.9492	0.8798	47.68	43.97	58.69	54.16	34.39
		13.51	120.1	71.35	811.7	948.2	1040	916.0	651.2
		11.61	27.12	20.78	406.4	412.9	405.5	437.9	285.1

Table A5. *Cont.*

Formation	Sample	Image Porosity (φ%)	Su_{TB} ($\times10^{-5}$)	Su_{BT} ($\times10^{-5}$)	Su_{LR} ($\times10^{-5}$)	Su_{RL} ($\times10^{-5}$)	Su_{FB} ($\times10^{-5}$)	Su_{BF} ($\times10^{-5}$)	$Su_{average}$ ($\times10^{-5}$)
Longmaxi	TY1-6	4.71	1.890	1.493	1.649	1.424	2.274	1.226	1.660
		6.66	4.844	4.230	4.731	4.729	5.651	4.132	4.720
		7.39	8.198	7.094	7.880	5.565	7.707	7.393	7.306
		10.88	19.06	23.05	15.68	16.83	23.83	18.15	19.43
	Average	7.75	779.4	743.3	898.8	959.4	923.0	968.1	878.6
Qiongzhusi	N206-2	11.78	448.3	410.6	476.3	1589	1688	642.9	876.0
		2.57	1.030	0.7149	1.010	0.7582	1.303	0.8475	0.9438
		2.65	0.8996	0.6258	0.8406	0.6773	1.056	0.5.242	0.7706
		3.31	1.450	0.6720	1.375	1.218	1.831	0.7210	1.211
		2.48	0.9371	1.241	0.7.637	0.7144	1.117	1.043	0.9693
	N206-5	1.98	0.4926	0.5923	0.4233	0.3569	0.8030	0.2178	0.4810
		1.3	0.2.21	0.1361	0.2126	0.07206	0.2705	0.09196	0.1659
		2.24	1.156	0.9730	0.5490	0.7483	0.8256	0.9441	0.8660
	N206-7	4.59	7.970	6.400	5.920	3.266	10.40	5.040	6.499
		1.58	0.6604	0.2545	0.5035	0.6630	0.5.033	0.5628	0.5246
	Average	3.45	46.31	42.22	48.79	159.8	170.6	65.29	88.84

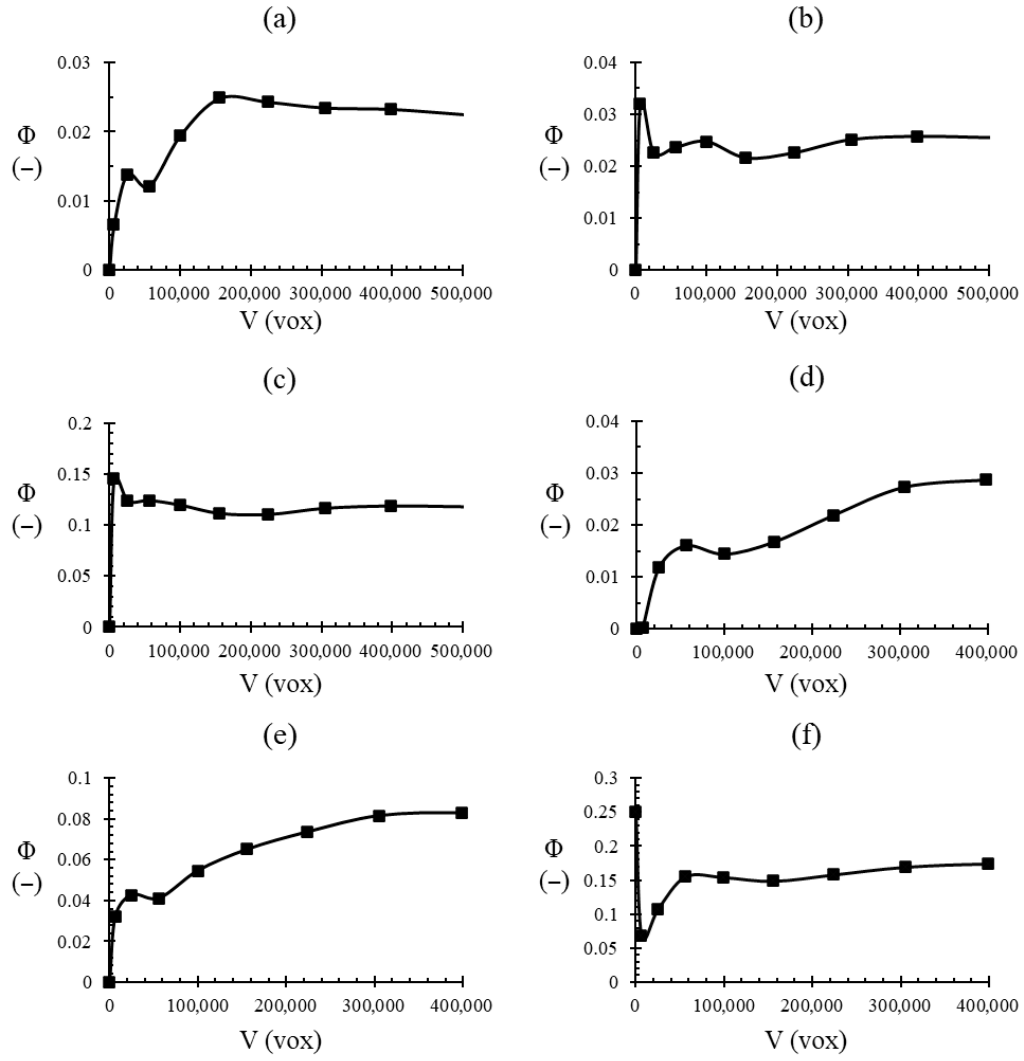

Figure A1. Plots to determine that the representative elementary volume (REV) has been reached for segmented SEM images (**a**–**f**) corresponding to Figure 19.

Appendix B

The explanation of the sample selection criteria:

The Longmaxi–TY1 and Qiongzhusi–N206 wells were selected because they penetrate thick, organic-rich shale intervals that are stratigraphically representative of the Lower Silurian and Lower Cambrian formations in the Sichuan Basin. In the Qiongzhusi–N206 well, the target organic-rich shale interval is ~40 m thick (1850–1890 m), and our 10 samples were systematically collected across this depth range (1846.53–1888.26 m). Similarly, in the Longmaxi–TY1 well, the organic-rich shale interval is ~60 m thick (620–680 m), and the 10 samples collected from 622.6–677.5 m adequately represent the vertical variability of the reservoir interval. This sampling strategy ensures that the major lithological and geochemical features of the target sections are captured.

References

1. Zhironkin, S.; Abu-Abed, F. Fossil fuel prospects in the energy of the future (energy 5.0): A review. *Energies* **2024**, *17*, 5606. [CrossRef]
2. Zou, C.; Zhao, Q.; Zhang, G.; Xiong, B. Energy revolution: From a fossil energy era to a new energy era. *Nat. Gas Ind. B* **2016**, *3*, 1–11. [CrossRef]
3. Xu, Y.; Lun, Z.; Wang, H.; Zhao, C.; Zhou, X.; Hu, W.; Zou, J.; Zhang, D. Understanding roles of moisture in CO_2 adsorption and desorption hysteresis on deep gas-bearing shales under high temperature and pressure. *Sep. Purif. Technol.* **2024**, *334*, 125970. [CrossRef]
4. Rui, Z.; Qian, C.; Liu, Y.; Zhao, Y.; Li, H.A.; Afanasyev, A.; Torabi, F. Adsorption characteristics of $CO_2/CH_4/H_2S$ mixtures in calcite nanopores with the implications for CO_2 sequestration. *SPE J.* **2024**, *29*, 2748–2762. [CrossRef]
5. Li, Z.; Zhang, J.; Mo, X.; Tong, Z.; Wang, X.; Wang, D.; Su, Z.; Tang, X.; Gong, D. Characterization of an Angstrom-Scale Pore Structure in Organic- Rich Shales by Using Low-Pressure CO_2 Adsorption and Multifractal Theory and Its Role in CH_4/CO_2 Gas Storage. *Energy Fuels* **2022**, *36*, 12085–12103. [CrossRef]
6. Pang, J.; Liang, Y.; Mi, F.; Jiang, G.; Tsuji, T.; Ning, F. Nanoscale Understanding on CO_2 Diffusion and Adsorption in Clay Matrix Nanopores: Implications for Carbon Geosequestration. *Environ. Sci. Technol.* **2024**, *58*, 20401–20411. [CrossRef] [PubMed]
7. Ma, L.; Fauchille, A.-L.; Ansari, H.; Chandler, M.; Ashby, P.; Taylor, K.; Pini, R.; Lee, P.D. Linking multi-scale 3D microstructure to potential enhanced natural gas recovery and subsurface CO_2 storage for Bowland shale, UK. *Energy Environ. Sci.* **2021**, *14*, 4481–4498. [CrossRef]
8. Ukaomah, C.F.; Sun, M.; Pan, Z.; Ostadhassan, M.; Liu, B.; Xu, Y.; Madaki, A.I.; Umeobi, H.I.; Aminu, M.D.; Yang, B. An insight into CO_2 sequestration and EGR in Longmaxi and Niutitang shale formations via experimental analysis. *Fuel* **2022**, *324*, 124776. [CrossRef]
9. Wang, Y.; Ding, Z.; Cao, Z.; Han, F.; Wang, Y.; Cheng, H. Molecular simulation of CO_2 adsorption on kaolinite: Insights into geological storage of CO_2. *Appl. Clay Sci.* **2024**, *258*, 107495. [CrossRef]
10. Wang, D.; Hu, H.; Wang, T.; Tang, T.; Li, W.; Zhu, G.; Chen, X. Difference between of coal and shale pore structural characters based on gas adsorption experiment and multifractal analysis. *Fuel* **2024**, *371*, 132044. [CrossRef]
11. Zeng, C.; Kalam, S.; Zhang, H.; Wang, L.; Luo, Y.; Wang, H.; Mu, Z.; Arif, M. Predicting absolute adsorption of CO_2 on Jurassic shale using machine learning. *Fuel* **2025**, *381*, 133050. [CrossRef]
12. Ou, C.; You, Z. Review of CO_2 utilization and storage in adsorption-type unconventional natural gas reservoirs. *Fuel* **2024**, *374*, 132352. [CrossRef]
13. Benson, S.M.; Cole, D.R. CO_2 sequestration in deep sedimentary formations. *Elements* **2008**, *4*, 325–331. [CrossRef]
14. Worden, R.H. Carbon dioxide capture and storage (CCS) in saline aquifers versus depleted gas fields. *Geosciences* **2024**, *14*, 146. [CrossRef]
15. Raza, A.; Gholami, R.; Rabiei, M.; Rasouli, V.; Rezaee, R.; Fakhari, N. Impact of geochemical and geomechanical changes on CO_2 sequestration potential in sandstone and limestone aquifers. *Greenh. Gases: Sci. Technol.* **2019**, *9*, 905–923. [CrossRef]
16. Arif, H.; Abdulwahab, B.; Muhammad Naveed, B.; Muhammad Hammad, M.; Ardiansyah, K.; Abduljamiu, A.; Cornel, O.; Khalid, A.-R. Diagenetic variability in Tertiary, syn-rift mixed siliciclastic-carbonate depositional system (Lower Musayr Formation), Red Sea, Saudi Arabia. *Sediment. Geol.* **2024**, *470*, 106699. [CrossRef]
17. Jiang, L.L.; Chen, Z.X.; Ali, S.M.F.; Zhang, J.S.; Chen, Y.P.; Chen, S.S. Storing carbon dioxide in deep unmineable coal seams for centuries following underground coal gasification. *J. Clean. Prod.* **2022**, *378*, 134565. [CrossRef]
18. Liu, X.; Zhang, B.; Xuehai, F.; Jielin, L.; Manli, H.; Fanhua, Z. Potential, Efficiency, and Leakage Risk of CO_2 Sequestration in Coal: A Review. *Processes* **2025**, *13*, 1680. [CrossRef]

19. Grant Charles, M.; Melckzedeck Michael, M.; Mbega Ramadhani, N.; Long, Y. Recent advances on carbon dioxide sequestration potentiality in salt caverns: A review. *Int. J. Greenh. Gas Control* **2024**, *133*, 104109. [CrossRef]
20. Matter, J.M.; Stute, M.; Snæbjörnsdottir, S.Ó.; Oelkers, E.H.; Gislason, S.R.; Aradottir, E.S.; Sigfusson, B.; Gunnarsson, I.; Sigurdardottir, H.; Gunnlaugsson, E.; et al. Rapid carbon mineralization for permanent disposal of anthropogenic carbon dioxide emissions. *Science* **2016**, *352*, 1312–1314. [CrossRef]
21. Kelemen, P.; Benson, S.M.; Pilorgé, H.; Psarras, P.; Wilcox, J. An overview of the status and challenges of CO_2 storage in minerals and geological formations. *Front. Clim.* **2019**, *1*, 9. [CrossRef]
22. Hu, K.; Liu, Y.; Zhang, Q.; Song, Z.; Thaika, M.A.; Li, R.; Kuru, E.; Shi, J.; Liu, H. From Micropores to Macropores: Investigating Pore Characteristics of Longmaxi Shale in the Sichuan Basin. *Energy Fuels* **2024**, *38*, 3961–3981. [CrossRef]
23. Adeyilola, A.; Zakharova, N.; Liu, K.; Gentzis, T.; Carvajal-Ortiz, H.; Fowler, H.; Harrison Iii, W.B. Porosity distribution in the Devonian Antrim Shale: Controlling factors and implications for gas sorption. *Int. J. Coal Geol.* **2023**, *272*, 104251. [CrossRef]
24. Garum, M.; Glover, P.W.J.; Lorinczi, P.; Micklethwaite, S.; Hassanpour, A. Integration of Multiscale Imaging of Nanoscale Pore Microstructures in Gas Shales. *Energy Fuels* **2021**, *35*, 10721–10732. [CrossRef]
25. Chen, Z.; Zhao, X.; Zhu, H.; Tang, Z.; Zhao, X.; Zhang, F.; Sepehrnoori, K. Engineering factor analysis and intelligent prediction of CO_2 2 storage parameters in shale gas reservoirs based on deep learning. *Appl. Energy* **2025**, *377*, 124642. [CrossRef]
26. Wang, J.; Wang, K.; Shan, X.; Ma, L.; Taylor, K.G. Potential for CO_2 storage in shale basins in China. *Int. J. Greenh. Gas Control* **2024**, *132*, 104060. [CrossRef]
27. Murugesu, M.P.; Joewondo, N.; Prasad, M. Carbon storage capacity of shale formations: Mineral control on CO_2 adsorption. *Int. J. Greenh. Gas Control* **2023**, *124*, 103833. [CrossRef]
28. Zhang, D.; Tang, H.; Song, Y.; Perera, M.S.A.; Ranjith, P.G. Molecular simulation of the competitive adsorption of methane and carbon dioxide in the matrix and slit model of shale kerogen and the influence of water. *Geoenergy Sci. Eng.* **2024**, *242*, 213212. [CrossRef]
29. Wang, H.; Zhang, M.; Xia, X.; Tian, Z.; Qin, X.; Cai, J. Lattice Boltzmann prediction of CO_2 and CH_4 competitive adsorption in shale porous media accelerated by machine learning for CO_2 sequestration and enhanced CH_4 recovery. *Appl. Energy* **2024**, *370*, 123638. [CrossRef]
30. Chang, X.; Lin, S.; Yang, C.; Guo, Y.; Dai, X. Enhancing shale gas recovery and CO_2 sequestration: Microscopic mechanisms of adsorption and diffusion in shale pores. *Phys. Fluids* **2024**, *36*, 116614. [CrossRef]
31. Hou, L.; Elsworth, D.; Zhang, L.; Gong, P.; Liu, H. Recalibration of CO_2 storage in shale: Prospective and contingent storage resources, and capacity. *Energy* **2024**, *290*, 130067. [CrossRef]
32. Fatah, A.; Bennour, Z.; Ben Mahmud, H.; Gholami, R.; Hossain, M.M. A review on the influence of CO_2/shale interaction on shale properties: Implications of CCS in shales. *Energies* **2020**, *13*, 3200. [CrossRef]
33. Heidarabad, R.G.; Shin, K. Carbon Capture and Storage in Depleted Oil and Gas Reservoirs: The Viewpoint of Wellbore Injectivity. *Energies* **2024**, *17*, 1201. [CrossRef]
34. Shi, J.; Shen, G.; Zhao, H.; Sun, N.; Song, X.; Guo, Y.; Wei, W.; Sun, Y. Porosity at the interface of organic matter and mineral components contribute significantly to gas adsorption on shales. *J. CO_2 Util.* **2018**, *28*, 73–82. [CrossRef]
35. Lin, S.; Chang, X.; Wang, K.; Yang, C.; Guo, Y. Swelling damage characteristics induced by CO_2 adsorption in shale: Experimental and modeling approaches. *J. Rock Mech. Geotech. Eng.* **2024**, *17*, 5526–5541. [CrossRef]
36. Onwumelu, C.; Kolawole, O.; Bouchakour, I.; Ozotta, O.; Nordeng, S.; Alamooti, M. CO_2-Induced alterations due to thermal maturation in shale: Implications for CO_2 utilization and storage. *Greenh. Gases-Sci. Technol.* **2023**, *13*, 797–813. [CrossRef]
37. Wang, L.; Liu, B.; Bai, L.; Ma, L.; Yu, Z.; Huo, Q.; Taylor, K.G. Differential mineral diagenetic evolution of lacustrine shale: Implications for CO_2 storage. *Int. J. Coal Geol.* **2024**, *295*, 104629. [CrossRef]
38. Liu, B.; Wang, Y.; Tian, S.; Guo, Y.; Wang, L.; Yasin, Q.; Yang, J. Impact of thermal maturity on the diagenesis and porosity of lacustrine oil-prone shales: Insights from natural shale samples with thermal maturation in the oil generation window. *Int. J. Coal Geol.* **2022**, *261*, 104079. [CrossRef]
39. Wang, Y.; Liu, L.; Cheng, H. Gas Adsorption Characterization of Pore Structure of Organic-rich Shale: Insights into Contribution of Organic Matter to Shale Pore Network. *Nat. Resour. Res.* **2021**, *30*, 2377–2395. [CrossRef]
40. Kennedy, M.J.; Pevear, D.R.; Hill, R.J. Mineral surface control of organic carbon in black shale. *Science* **2002**, *295*, 657–660. [CrossRef]
41. Kennedy, M.J.; Wagner, T. Clay mineral continental amplifier for marine carbon sequestration in a greenhouse ocean. *Proc. Natl. Acad. Sci. USA* **2011**, *108*, 9776–9781. [CrossRef] [PubMed]
42. Hussain, A.; Haughton, P.D.; Shannon, P.M.; Morris, E.A.; Pierce, C.S.; Omma, J.E. Mud-forced turbulence dampening facilitates rapid burial and enhanced preservation of terrestrial organic matter in deep-sea environments. *Mar. Pet. Geol.* **2021**, *130*, 105101. [CrossRef]
43. Zhang, Y.; Li, D.; Xin, G.; Ren, S. A Review of Molecular Models for Gas Adsorption in Shale Nanopores and Experimental Characterization of Shale Properties. *Acs Omega* **2023**, *8*, 13519–13538. [CrossRef]

44. Fatah, A.; Ben Mahmud, H.; Bennour, Z.; Gholami, R.; Hossain, M.M. Geochemical and physical alteration of clay-rich shales under supercritical CO_2 conditions. *Appl. Geochem.* **2022**, *140*, 105291. [CrossRef]
45. Xie, W.; Chen, S.; Vandeginste, V.; Yu, Z.; Wang, H.; Wang, M. Review of the Effect of Diagenetic Evolution of Shale Reservoir on the Pore Structure and Adsorption Capacity of Clay Minerals. *Energy Fuels* **2022**, *36*, 4728–4745. [CrossRef]
46. Gou, Q.; Xu, S.; Hao, F.; Shu, Z.; He, S.; Wu, Z. Differences in the Nanopore Structure of Organic-Rich Shales with Distinct Sedimentary Environments and Mineral Compositions. *Energy Fuels* **2021**, *35*, 16562–16577. [CrossRef]
47. Wang, Y.; Xu, S.; Hao, F.; Zhang, B.; Shu, Z.; Gou, Q.; Lu, Y.; Cong, F. Multiscale petrographic heterogeneity and their implications for the nanoporous system of the Wufeng-Longmaxi shales in Jiaoshiba area, Southeast China: Response to depositional-diagenetic process. *Geol. Soc. Am. Bull.* **2020**, *132*, 1704–1721. [CrossRef]
48. Sing, K.S. Reporting physisorption data for gas/solid systems with special reference to the determination of surface area and porosity. *Pure Appl. Chem.* **1985**, *57*, 603–619. [CrossRef]
49. Tian, Z.; Wei, W.; Zhou, S.; Wood, D.A.; Cai, J. Experimental and Fractal Characterization of the Microstructure of Shales from Sichuan Basin, China. *Energy Fuels* **2021**, *35*, 3899–3914. [CrossRef]
50. Hawthorne, S.B.; Miller, D.J.; Pekot, L.J.; Azzolina, N.A.; Kurz, B.A.; Sorensen, J.A. Measured CO_2 sorption isotherms with 25 Bakken Petroleum System rock samples from the Lower and Upper Shales, Middle Bakken, and Three Forks formations. *Int. J. Greenh. Gas Control* **2023**, *127*, 103930. [CrossRef]
51. Wang, X.; Jiang, Z.; Jiang, S.; Chang, J.; Zhu, L.; Li, X.; Li, J. Full-Scale Pore Structure and Fractal Dimension of the Longmaxi Shale from the Southern Sichuan Basin: Investigations Using FE-SEM, Gas Adsorption and Mercury Intrusion Porosimetry. *Minerals* **2019**, *9*, 543. [CrossRef]
52. Zhang, N.; Wang, S.; Xun, X.; Wang, H.; Sun, X.; He, M. Pore Structure and Fractal Characteristics of Coal-Measure Sedimentary Rocks Using Nuclear Magnetic Resonance (NMR) and Mercury Intrusion Porosimetry (MIP). *Energies* **2023**, *16*, 3812. [CrossRef]
53. Zhou, B.; Han, Q.; Yang, P. Characterization of Nanoporous Systems in Gas Shales by Low Field NMR Cryoporometry. *Energy Fuels* **2016**, *30*, 9122–9131. [CrossRef]
54. Jiang, F.; Chen, J.; Xu, Z.; Wang, Z.; Hu, T.; Chen, D.; Li, Q.; Li, Y. Organic Matter Pore Characterization in Lacustrine Shales with Variable Maturity Using Nanometer-Scale Resolution X-ray Computed Tomography. *Energy Fuels* **2017**, *31*, 2669–2680. [CrossRef]
55. Gou, Q.; Xu, S.; Hao, F.; Yang, F.; Zhang, B.; Shu, Z.; Zhang, A.; Wang, Y.; Lu, Y.; Cheng, X.; et al. Full-scale pores and micro-fractures characterization using FE-SEM, gas adsorption, nano-CT and micro-CT: A case study of the Silurian Longmaxi Formation shale in the Fuling area, Sichuan Basin, China. *Fuel* **2019**, *253*, 167–179. [CrossRef]
56. Wang, P.; Zhang, C.; Li, X.; Zhang, K.; Yuan, Y.; Zang, X.; Cui, W.; Liu, S.; Jiang, Z. Organic matter pores structure and evolution in shales based on the he ion microscopy (HIM): A case study from the Triassic Yanchang, Lower Silurian Longmaxi and Lower Cambrian Niutitang shales in China. *J. Nat. Gas Sci. Eng.* **2020**, *84*, 103682. [CrossRef]
57. Huang, C.; Ju, Y.; Zhu, H.; Qi, Y.; Yu, K.; Sun, Y.; Ju, L. Nano-Scale Pore Structure and Fractal Dimension of Longmaxi Shale in the Upper Yangtze Region, South China: A Case Study of the Laifeng-Xianfeng Block Using HIM and N_2 Adsorption. *Minerals* **2019**, *9*, 356. [CrossRef]
58. Kelly, S.; El-Sobky, H.; Torres-Verdin, C.; Balhoff, M.T. Assessing the utility of FIB-SEM images for shale digital rock physics. *Adv. Water Resour.* **2016**, *95*, 302–316. [CrossRef]
59. Liang, Y.; Wang, S.; Feng, Q.; Zhang, M.; Cao, X.; Wang, X. Ultrahigh- Resolution Reconstruction of Shale Digital Rocks from FIB-SEM Images Using Deep Learning. *SPE J.* **2024**, *29*, 1434–1450. [CrossRef]
60. Blach, T.; Radlinski, A.P.; Vu, P.; Ji, Y.; de Campo, L.; Gilbert, E.P.; Regenauer-Lieb, K.; Mastalerz, M. Accessibility of Pores to Methane in New Albany Shale Samples of Varying Maturity Determined Using SANS and USANS. *Energies* **2021**, *14*, 8438. [CrossRef]
61. Clarkson, C.R.; Solano, N.; Bustin, R.M.; Bustin, A.M.M.; Chalmers, G.R.L.; He, L.; Melnichenko, Y.B.; Radlinski, A.P.; Blach, T.P. Pore structure characterization of North American shale gas reservoirs using USANS/SANS, gas adsorption, and mercury intrusion. *Fuel* **2013**, *103*, 606–616. [CrossRef]
62. Wu, K.; Van Dijke, M.I.; Couples, G.D.; Jiang, Z.; Ma, J.; Sorbie, K.S.; Crawford, J.; Young, I.; Zhang, X. 3D stochastic modelling of heterogeneous porous media–applications to reservoir rocks. *Transp. Porous Media* **2006**, *65*, 443–467. [CrossRef]
63. Luo, M.; Glover, P.W.; Zhao, P.; Li, D. 3D digital rock modeling of the fractal properties of pore structures. *Mar. Pet. Geol.* **2020**, *122*, 104706. [CrossRef]
64. Zhang, C.; Guan, P.; Zhang, J.; Ding, X. Methodological Study on the Full-Range Pore Structure and Fractal Characteristics of the Tight Reservoirs. *Minerals* **2023**, *13*, 587. [CrossRef]
65. Li, Z.; Shen, X.; Qi, Z.; Hu, R. Study on the pore structure and fractal characteristics of marine and continental shale based on mercury porosimetry, N_2 adsorption and NMR methods. *J. Nat. Gas Sci. Eng.* **2018**, *53*, 12–21. [CrossRef]
66. Liu, X.; Nie, B. Fractal characteristics of coal samples utilizing image analysis and gas adsorption. *Fuel* **2016**, *182*, 314–322. [CrossRef]

67. He, H.; Liu, P.; Xu, L.; Hao, S.; Qiu, X.; Shan, C.; Zhou, Y. Pore structure representations based on nitrogen adsorption experiments and an FHH fractal model: Case study of the block Z shales in the Ordos Basin, China. *J. Pet. Sci. Eng.* **2021**, *203*, 108661. [CrossRef]
68. Zhang, J.; Tang, Y.; He, D.; Sun, P.; Zou, X. Full-scale nanopore system and fractal characteristics of clay-rich lacustrine shale combining FE-SEM, nano-CT, gas adsorption and mercury intrusion porosimetry. *Appl. Clay Sci.* **2020**, *196*, 105758. [CrossRef]
69. Yang, R.; He, S.; Hu, Q.; Sun, M.; Hu, D.; Yi, J. Applying SANS technique to characterize nano-scale pore structure of Longmaxi shale, Sichuan Basin (China). *Fuel* **2017**, *197*, 91–99. [CrossRef]
70. Liu, K.; Ostadhassan, M.; Zou, J.; Gentzis, T.; Rezaee, R.; Bubach, B.; Carvajal-Ortiz, H. Multifractal analysis of gas adsorption isotherms for pore structure characterization of the Bakken Shale. *Fuel* **2018**, *219*, 296–311. [CrossRef]
71. Wang, Y.; Cheng, H.; Hu, Q.; Liu, L.; Jia, L.; Gao, S.; Wang, Y. Pore structure heterogeneity of Wufeng-Longmaxi shale, Sichuan Basin, China: Evidence from gas physisorption and multifractal geometries. *J. Pet. Sci. Eng.* **2022**, *208*, 109313. [CrossRef]
72. de Melo, R.H.C. Using Fractal Characteristics such as Fractal Dimension, Lacunarity and Succolarity to Characterize Texture Patterns on Images. 2007; pp. 1–85. Available online: https://app.uff.br/riuff/bitstream/handle/1/17146/Dissert-Rafael%20Melo.pdf?sequence=1&isAllowed=y (accessed on 10 September 2025).
73. Mandelbrot, B.B. *The Fractal Geometry of Nature*; W.H.Freeman & Co Ltd.: New York, NY, USA, 1983; pp. 1–468.
74. Li, B.; Panaitescu, C.-T.; Glover, P.W.J.; Lorinczi, P.; Wu, K.; Yu, B.; Wei, W.; Cui, J.; Shi, M. Unravelling 3D Succolarity to Quantify Multiscale Petrophysical and Structural Properties of Porous Media. *Water Resour. Res.* **2025**, *submitted*. [CrossRef]
75. Horsfield, B.; Zou, C.; Li, J.; Yang, S.; Mahlstedt, N.; Misch, D.; Gross, D.; Wei, M.; Wang, Y.; Tan, J. Prediction of the gas-generating characteristics of the Qiongzhusi and Longmaxi Formations, Yangtze Platform, southern China, using analogues. *AAPG Bull.* **2021**, *105*, 945–985. [CrossRef]
76. Xu, C.; Yao, S.; Song, D.; Liu, Y. Types, chemical and porosity characteristics of hydrocarbon-generating organisms of the lower Paleozoic, south China-Taking Longmaxi Formation and Qiongzhusi Formation in Sichuan Basin as examples. *Mar. Pet. Geol.* **2020**, *119*, 104508. [CrossRef]
77. Liu, S.; Ma, W.; Luba, J.; Huang, W.; Zeng, X.; Zhang, C. Characteristics of the shale gas reservoir rocks in the Lower Silurian Longmaxi Formation, East Sichuan basin, China. *Acta Petrol. Sin.* **2011**, *27*, 2239–2252. [CrossRef]
78. Shi, M.; Yu, B.; Xue, Z.; Wu, J.; Yuan, Y. Pore characteristics of organic-rich shales with high thermal maturity: A case study of the Longmaxi gas shale reservoirs from well Yuye-1 in southeastern Chongqing, China. *J. Nat. Gas Sci. Eng.* **2015**, *26*, 948–959. [CrossRef]
79. Gai, S.; Liu, H.; He, S.; Mo, S.; Chen, S.; Liu, R.; Huang, X.; Tian, J.; Lv, X.; Wu, D.; et al. Shale reservoir characteristics and exploration potential in the target: A case study in the Longmaxi Formation from the southern Sichuan Basin of China. *J. Nat. Gas Sci. Eng.* **2016**, *31*, 86–97. [CrossRef]
80. Huang, J.; Zou, C.; Li, J.; Dong, D.; Wang, S.; Wang, S.; Cheng, K. Shale gas generation and potential of the Lower Cambrian Qiongzhusi Formation in the Southern Sichuan Basin, China. *Pet. Explor. Dev.* **2012**, *39*, 75–81. [CrossRef]
81. Jiao, K.; Ye, Y.; Liu, S.; Ran, B.; Deng, B.; Li, Z.; Li, J.; Yong, Z.; Sun, W. Characterization and Evolution of Nanoporosity in Superdeeply Buried Shales: A Case Study of the Longmaxi and Qiongzhusi Shales from MS Well #1, North Sichuan Basin, China. *Energy Fuels* **2018**, *32*, 191–203. [CrossRef]
82. Liu, R.; Zhou, W.; Xu, H.; Zhou, Q.; Jiang, K.; Shang, F.; Gao, W.; Song, W.; Liu, D.; Zhao, H.; et al. Impact of Minerals and Sealing Systems on the Pore Characteristics of the Qiongzhusi Formation Shale in the Southern Sichuan Basin. *ACS Omega* **2022**, *7*, 15821–15840. [CrossRef]
83. Wang, P.; Jiang, Z.; Chen, L.; Yin, L.; Li, Z.; Zhang, C.; Tang, X.; Wang, G. Pore structure characterization for the Longmaxi and Niutitang shales in the Upper Yangtze Platform, South China: Evidence from focused ion beam He ion microscopy, nano-computerized tomography and gas adsorption analysis. *Mar. Pet. Geol.* **2016**, *77*, 1323–1337. [CrossRef]
84. Zhang, L.; Xiao, D.; Lu, S.; Jiang, S.; Chen, L.; Guo, T.; Wu, L. Pore development of the Lower Longmaxi shale in the southeastern Sichuan Basin and its adjacent areas: Insights from lithofacies identification and organic matter. *Mar. Pet. Geol.* **2020**, *122*, 104662. [CrossRef]
85. Chen, S.; Gong, Z.; Li, X.; Wang, H.; Wang, Y.; Zhang, Y. Pore structure and heterogeneity of shale gas reservoirs and its effect on gas storage capacity in the Qiongzhusi Formation. *Geosci. Front.* **2021**, *12*, 101244. [CrossRef]
86. Wang, R.; Hu, Z.; Sun, C.; Liu, Z.; Zhang, C.; Gao, B.; Du, W.; Zhao, J.; Tang, W. Comparative analysis of shale reservoir characteristics in the Wufeng-Longmaxi (O_3w-S_1l) and Niutitang ($\in_1 n$) Formations: A case study of wells JY1 and TX1 in the southeastern Sichuan Basin and its neighboring areas, southwestern China. *Interpret. -A J. Subsurf. Charact.* **2018**, *6*, SN31–SN45. [CrossRef]
87. Gou, Q.; Xu, S.; Hao, F.; Lu, Y.; Shu, Z.; Lu, Y.; Wang, Z.; Wang, Y. Evaluation of the exploration prospect and risk of marine gas shale, southern China: A case study of Wufeng-Longmaxi shales in the Jiaoshiba area and Niutitang shales in the Cen'gong area. *Geol. Soc. Am. Bull.* **2022**, *134*, 1585–1602. [CrossRef]

88. Li, J. Reservoir Characteristics of Longmaxi Shale in the Southeast of Chongqing: A Case Study from Lujiao Outcrop Section and Well Yuye-1. Master's Thesis, China University of Geosciences, Beijing China, 2013.
89. Tan, J.; Horsfield, B.; Mahlstedt, N.; Zhang, J.; di Primio, R.; Vu, T.A.T.; Boreham, C.J.; van Graas, G.; Tocher, B.A. Physical properties of petroleum formed during maturation of Lower Cambrian shale in the upper Yangtze Platform, South China, as inferred from PhaseKinetics modelling. *Mar. Pet. Geol.* **2013**, *48*, 47–56. [CrossRef]
90. Li, A.; Ding, W.; Jiu, K.; Wang, Z.; Wang, R.; He, J. Investigation of the pore structures and fractal characteristics of marine shale reservoirs using NMR experiments and image analyses: A case study of the Lower Cambrian Niutitang Formation in northern Guizhou Province, South China. *Mar. Pet. Geol.* **2018**, *89*, 530–540. [CrossRef]
91. Wang, R.; Liu, Y.; Li, Z.; Wang, D.; Wang, G.; Lai, F.; Li, Z.; He, J. Microscopic pore structure characteristics and controlling factors of marine shale: A case study of Lower Cambrian shales in the Southeastern Guizhou, Upper Yangtze Platform, South China. *Front. Earth Sci.* **2024**, *12*, 1368326. [CrossRef]
92. Ran, L. Characteristics of oil-gas resources in Sichuan Basin. *China Oil Gas* **2006**, *4*, 24–27.
93. Yong, M.; Zhejun, P.; Ningning, Z.; Luke, D.C.; David, I.D.; Wenlie, L.; Yi, Z. Experimental study of anisotropic gas permeability and its relationship with fracture structure of Longmaxi Shales, Sichuan Basin, China. *Fuel* **2016**, *180*, 106–115. [CrossRef]
94. Shangbin, C.; Yanming, Z.; Hongyan, W.; Honglin, L.; Wei, W.; Junhua, F. Shale gas reservoir characterisation: A typical case in the southern Sichuan Basin of China. *Energy* **2011**, *36*, 6609–6616. [CrossRef]
95. Dong, D.; Shi, Z.; Guan, Q.; Jiang, S.; Zhang, M.; Zhang, C.; Wang, S.; Sun, S.; Yu, R.; Liu, D. Progress, challenges and prospects of shale gas exploration in the Wufeng–Longmaxi reservoirs in the Sichuan Basin. *Nat. Gas Ind. B* **2018**, *5*, 415–424. [CrossRef]
96. Gou, Q.; Wang, Y.; Xu, S.; Hao, F.; Wang, Z. The exploration prospects of Ediacaran shales in the Yangtze Platform, South China: Insights from the coupling of generation, storage, and preservation. *J. Asian Earth Sci.* **2023**, *256*, 105829. [CrossRef]
97. Zhang, J.; Shi, M.; Wang, D.; Tong, Z.; Hou, X.; Niu, J.; Li, X.; Li, Z.; Zhang, P.; Huang, Y. Fields and directions for shale gas exploration in China. *Nat. Gas Ind. B* **2022**, *9*, 20–32. [CrossRef]
98. Wang, Y.; Qin, Y.; Zhang, R.; He, L.; Anovitz, L.M.; Bleue, M.; Mildner, D.F.R.; Liu, S.; Zhu, Y. Evaluation of Nanoscale Accessible Pore Structures for Improved Prediction of Gas Production Potential in Chinese Marine Shales. *Energy Fuels* **2018**, *32*, 12447–12461. [CrossRef]
99. Sun, M.; Zhang, L.; Hu, Q.; Pan, Z.; Yu, B.; Sun, L.; Bai, L.; Fu, H.; Zhang, Y.; Zhang, C.; et al. Multiscale connectivity characterization of marine shales in southern China by fluid intrusion, small-angle neutron scattering (SANS), and FIB-SEM. *Mar. Pet. Geol.* **2020**, *112*, 104101. [CrossRef]
100. Jacob, H. Classification, structure, genesis and practical importance of natural solid oil bitumen ("migrabitumen"). *Int. J. Coal Geol.* **1989**, *11*, 65–79. [CrossRef]
101. Schoenherr, J.; Littke, R.; Urai, J.L.; Kukla, P.A.; Rawahi, Z. Polyphase thermal evolution in the Infra-Cambrian Ara Group (South Oman Salt Basin) as deduced by maturity of solid reservoir bitumen. *Org. Geochem.* **2007**, *38*, 1293–1318. [CrossRef]
102. Washburn, E.W. The dynamics of capillary flow. *Phys. Rev.* **1921**, *17*, 273. [CrossRef]
103. Brunauer, S.; Emmett, P.H.; Teller, E. Adsorption of gases in multimolecular layers. *J. Am. Chem. Soc.* **1938**, *60*, 309–319. [CrossRef]
104. Barrett, E.P.; Joyner, L.G.; Halenda, P.P. The determination of pore volume and area distributions in porous substances. I. Computations from nitrogen isotherms. *J. Am. Chem. Soc.* **1951**, *73*, 373–380. [CrossRef]
105. Lastoskie, C.; Gubbins, K.E.; Quirke, N. Pore size distribution analysis of microporous carbons: A density functional theory approach. *J. Phys. Chem.* **1993**, *97*, 4786–4796. [CrossRef]
106. Seaton, N.; Walton, J. A new analysis method for the determination of the pore size distribution of porous carbons from nitrogen adsorption measurements. *Carbon* **1989**, *27*, 853–861. [CrossRef]
107. Do, D.; Do, H. Pore characterization of carbonaceous materials by DFT and GCMC simulations: A review. *Adsorpt. Sci. Technol.* **2003**, *21*, 389–423. [CrossRef]
108. Geman, S.; Geman, D. Stochastic relaxation, Gibbs distributions, and the Bayesian restoration of images. *IEEE Trans. Pattern Anal. Mach. Intell.* **1984**, *6*, 721–741. [CrossRef]
109. Qian, W.; Titterington, D. Multidimensional Markov chain models for image textures. *J. R. Stat. Soc. Ser. B (Methodol.)* **1991**, *53*, 661–674. [CrossRef]
110. Qian, W.; Titterington, D. Pixel labelling for three-dimensional scenes based on Markov mesh models. *Signal Process.* **1991**, *22*, 313–328. [CrossRef]
111. Ahammer, H.; Reiss, M.A.; Hackhofer, M.; Andronache, I.; Radulovic, M.; Labra-Spröhnle, F.; Jelinek, H.F. ComsystanJ: A collection of Fiji/ImageJ2 plugins for nonlinear and complexity analysis in 1D, 2D and 3D. *PLoS ONE* **2023**, *18*, e0292217. [CrossRef]
112. Ferreiro, J.P.; Wilson, M.; Vázquez, E.V. Multifractal description of nitrogen adsorption isotherms. *Vadose Zone J.* **2009**, *8*, 209–219. [CrossRef]
113. Kravchenko, A.N.; Boast, C.W.; Bullock, D.G. Multifractal analysis of soil spatial variability. *Agron. J.* **1999**, *91*, 1033–1041. [CrossRef]

114. Caniego, F.J.; Martin, M.A.; San Jose, F. Renyi dimensions of soil pore size distribution. *Geoderma* **2003**, *112*, 205–216. [CrossRef]
115. Rényi, A. On a new axiomatic theory of probability. *Acta Math. Hung.* **1955**, *6*, 285–335. [CrossRef]
116. Tissot, B.P.; Welte, D.H. *Petroleum Formation and Occurrence*; Springer Science & Business Media: Berlin/Heidelberg, Germany, 2013.
117. Du, J.; Cai, J.; Long, S.; Gao, B.; Feng, D.; Peng, Z.; Zeng, X. The control of diagenesis and mineral assemblages on brittleness of mudstones. *Front. Earth Sci.* **2021**, *9*, 758046. [CrossRef]
118. Qin, X.; Han, D.-H.; Zhao, L. Elastic characteristics of overpressure due to smectite-to-illite transition based on micromechanism analysis. *Geophysics* **2019**, *84*, WA23–WA42. [CrossRef]
119. Pytte, A.; Reynolds, R. The thermal transformation of smectite to illite. In *Thermal History of Sedimentary Basins: Methods and Case Histories*; Springer: Berlin/Heidelberg, Germany, 1989; pp. 133–140.
120. Worden, R.H.; Griffiths, J.; Wooldridge, L.J.; Utley, J.E.P.; Lawan, A.Y.; Muhammed, D.D.; Simon, N.; Armitage, P.J. Chlorite in sandstones. *Earth-Sci. Rev.* **2020**, *204*, 103105. [CrossRef]
121. Worden, R.H.; Morad, S. Clay minerals in sandstones: Controls on formation, distribution and evolution. In *Clay Mineral Cements in Sandstones*; John Wiley & Sons: Hoboken, NJ, USA, 1999; pp. 1–41.
122. Grigsby, J.D. Origin and growth mechanism of authigenic chlorite in sandstones of the lower Vicksburg Formation, south Texas. *J. Sediment. Res.* **2001**, *71*, 27–36. [CrossRef]
123. Wang, Z.; Cheng, Y.; Wang, G.; Ni, G.; Wang, L. Comparative analysis of pore structure parameters of coal by using low pressure argon and nitrogen adsorption. *Fuel* **2022**, *309*, 122120. [CrossRef]
124. Perfect, E.; Kay, B.D. Applications of fractals in soil and tillage research: A review. *Soil Tillage Res.* **1995**, *36*, 1–20. [CrossRef]
125. Liu, K.; Ostadhassan, M. Quantification of the microstructures of Bakken shale reservoirs using multi-fractal and lacunarity analysis. *J. Nat. Gas Sci. Eng.* **2017**, *39*, 62–71. [CrossRef]
126. Liu, K.; Ostadhassan, M.; Kong, L. Multifractal characteristics of Longmaxi Shale pore structures by N2 adsorption: A model comparison. *J. Pet. Sci. Eng.* **2018**, *168*, 330–341. [CrossRef]
127. Sun, W.; Zuo, Y.; Wu, Z.; Liu, H.; Xi, S.; Shui, Y.; Wang, J.; Liu, R.; Lin, J. Fractal analysis of pores and the pore structure of the Lower Cambrian Niutitang shale in northern Guizhou province: Investigations using NMR, SEM and image analyses. *Mar. Pet. Geol.* **2019**, *99*, 416–428. [CrossRef]
128. Thommes, M.; Kaneko, K.; Neimark, A.V.; Olivier, J.P.; Rodriguez-Reinoso, F.; Rouquerol, J.; Sing, K.S.W. Physisorption of gases, with special reference to the evaluation of surface area and pore size distribution (IUPAC Technical Report). *Pure Appl. Chem.* **2015**, *87*, 1051–1069. [CrossRef]
129. Katie, A.C.; Matthias, T. Progress in the Physisorption Characterization of Nanoporous Gas Storage Materials. *Engineering* **2018**, *4*, 559–566. [CrossRef]
130. Langmuir, I. The adsorption of gases on plane surfaces of glass, mica and platinum. *J. Am. Chem. Soc.* **1918**, *40*, 1361–1403. [CrossRef]
131. Tiina, L.; Ilkka, M.; Jani, K.; Juha, T. Utilization of Pisat temperature-dependency in modelling adsorption on zeolites. *Chem. Eng. Sci.* **2012**, *69*, 503–513. [CrossRef]
132. Taotao, C.; Mo, D.; Juanyi, X.; Hu, L.; Anyang, P.; Qinggu, C. Reservoir characteristics of marine–continental transitional shale and gas-bearing mechanism:Understanding based on comparison with marine shale reservoir. *J. Nat. Gas Geosci.* **2023**, *8*, 169–185. [CrossRef]
133. Mu, Y.; Hu, Z.; Guo, Q.; Duan, X.; Chang, J.; Niu, W.; Wu, Z. Water Distribution in Marine Shales: Based on Two-Dimensional Nuclear Magnetic Resonance and Low-Temperature Nitrogen Adsorption. *Energy Fuels* **2023**, *37*, 5034–5047. [CrossRef]
134. Span, R.; Wagner, W. A new equation of state for carbon dioxide covering the fluid region from the triple-point temperature to 1100 K at pressures up to 800 MPa. *J. Phys. Chem. Ref. Data* **1996**, *25*, 1509–1596. [CrossRef]
135. Stavropoulou, E.; Laloui, L. Evaluating CO_2 breakthrough in a shaly caprock material: A multi-scale experimental approach. *Sci. Rep.* **2022**, *12*, 10706. [CrossRef] [PubMed]
136. Ukaomah, C.F.; Zhang, L.; Xu, Y.; Sun, M.; Yang, B.; Madaki, A.I.; Umeobi, H.I.; Aminu, M.D. Pore Structure and Seal Capacity of Ilaro Formation Shales in the Eastern Dahomey Basin: Implications from Mercury Injection Capillary Pressure and Spontaneous Imbibition Analyses. *Energy Fuels* **2021**, *35*, 10086–10101. [CrossRef]
137. Celeste, D.L.; Paul, C.H. Using mercury injection pressure analyses to estimate sealing capacity of the Tuscaloosa marine shale in Mississippi, USA: Implications for carbon dioxide sequestration. *Int. J. Greenh. Gas Control* **2018**, *78*, 375–387. [CrossRef]
138. Xiaojin, Z.; Espinoza, D.N. Multiphase CO_2-brine transport properties of synthetic fault gouge. *Mar. Pet. Geol.* **2021**, *129*, 105054. [CrossRef]
139. Guiltinan, E.J.; Espinoza, D.N.; Cockrell, L.P.; Cardenas, M.B. Textural and compositional controls on mudrock breakthrough pressure and permeability. *Adv. Water Resour.* **2018**, *121*, 162–172. [CrossRef]
140. Cristian, R.M.; Maria, M.; Richard, W.L.; John, A.R. A novel multi-technique approach used in the petrophysical characterization of the Maquoketa Group (Ordovician) in the southeastern portion of the Illinois Basin: Implications for seal efficiency for the geologic sequestration of CO_2. *Int. J. Greenh. Gas Control* **2020**, *93*, 102883. [CrossRef]

141. Ding, S.; Wen, F.; Wang, N.; Zhang, Y.; Lu, R.; Gao, Y.; Yu, H. Multi-objective optimization of CO_2 enhanced oil recovery and storage processes in low permeability reservoirs. *Int. J. Greenh. Gas Control* **2022**, *121*, 103802. [CrossRef]
142. Yue, P.; Zhang, R.; Sheng, J.J.; Yu, G.; Liu, F. Study on the Influential Factors of CO_2 Storage in Low Permeability Reservoir. *Energies* **2022**, *15*, 344. [CrossRef]
143. Fan, Z.; Tian, M.; Li, M.; Mi, Y.; Jiang, Y.; Song, T.; Cao, J.; Liu, Z. Assessment of CO_2 Sequestration Capacity in a Low-Permeability Oil Reservoir Using Machine Learning Methods. *Energies* **2024**, *17*, 3979. [CrossRef]
144. Tran, H.; Sakhaee-Pour, A.; Bryant, S.L. A Simple Relation for Estimating Shale Permeability. *Transp. Porous Media* **2018**, *124*, 883–901. [CrossRef]
145. Feng, X.; Ma, F.; Zhao, H.; Liu, G.; Guo, J. Gas Multiple Flow Mechanisms and Apparent Permeability Evaluation in Shale Reservoirs. *Sustainability* **2019**, *11*, 2114. [CrossRef]
146. Wasaki, A.; Akkutlu, I.Y. Permeability of Organic-Rich Shale. *Spe J.* **2015**, *20*, 1384–1396. [CrossRef]
147. Glover, P.W. A generalized Archie's law for n phases. *Geophysics* **2010**, *75*, E247–E265. [CrossRef]
148. Glover, P.; Walker, E. Grain-size to effective pore-size transformation derived from electrokinetic theory. *Geophysics* **2009**, *74*, E17–E29. [CrossRef]
149. Rashid, F.; Glover, P.; Lorinczi, P.; Collier, R.; Lawrence, J. Porosity and permeability of tight carbonate reservoir rocks in the north of Iraq. *J. Pet. Sci. Eng.* **2015**, *133*, 147–161. [CrossRef]
150. Mastalerz, M.; Schimmelmann, A.; Drobniak, A.; Chen, Y. Porosity of Devonian and Mississippian New Albany Shale across a maturation gradient: Insights from organic petrology, gas adsorption, and mercuty intrusion. *AAPG Bull.* **2013**, *97*, 1621–1643. [CrossRef]
151. Slatt, R.M.; O'Brien, N.R. Pore types in the Barnett and Woodford gas shales: Contribution to understanding gas storage and migration pathways in fine-grained rocks. *AAPG Bull.* **2011**, *95*, 2017–2030. [CrossRef]
152. Ji, M.; Choi, S.; Kim, M.; Choi, B.; Min, B. Numerical investigation of CO_2-carbonated water-alternating-gas on enhanced oil recovery and geological carbon storage. *J. CO_2 Util.* **2023**, *74*, 102544. [CrossRef]
153. Chen, Y.; Zhao, J.-H.; Hu, Q.-H.; Liu, K.-Y.; Wu, W.; Luo, C.; Zhao, S.-H.; Zhang, Y.-Y. Origin of carbonate minerals and impacts on reservoir quality of the Wufeng and Longmaxi Shale, Sichuan Basin. *Pet. Sci.* **2023**, *20*, 3311–3336. [CrossRef]
154. Ayachit, U. *The Paraview Guide: A Parallel Visualization Application*; Kitware, Inc.: Clifton Park, NY, USA, 2015.
155. Ahrens, J.; Geveci, B.; Law, C.; Hansen, C.; Johnson, C. 36-paraview: An end-user tool for large-data visualization. In *The Visualization Handbook*; Scientific Research Publishing Inc.: Wuhan, China, 2005; pp. 717–731.
156. Team, T.M.D. Matplotlib: Visualization with Python (v3.10.0). *Zenodo* **2024**. [CrossRef]
157. *Origin (Pro), Version 2024*; OriginLab Corporation: Northampton, MA, USA, 2024.